On the topic of oceanic variability near the Coriolis frequency; generation mechanisms, observations, and implications for interior mixing

Byron Frank Kilbourne

A dissertation
submitted in partial fulfillment of the
requirements for the degree of

Doctor of Philosophy

University of Washington

2015

Reading Committee:

James B. Girton, Chair

Thomas B. Sanford

Eric Kunze

Program Authorized to Offer Degree:
School of Oceanography

University of Washington

Abstract

On the topic of oceanic variability near the Coriolis frequency; generation mechanisms, observations, and implications for interior mixing

Byron Frank Kilbourne

Chair of the Supervisory Committee:
Dr. James B. Girton
Ocean Physics Department

Internal waves with frequency near the Coriolis frequency, the frequency of oscillations due to the Coriolis acceleration (commonly denoted by the symbol f), are ubiquitous throughout the world's oceans. However, observational constraints on their global energetics and impact on subsurface mixing remain sparse. This study investigates near-inertial (inertial and Coriolis frequency are used interchangeably) waves in the Southern Ocean using measurements of water velocity made by Electromagnetic Autonomous Profiling Explorers (EM-APEX). Initial observations from the eastern Pacific showed that coherent near-inertial waves were episodic and enhanced at mid-depth between 500 and 1000 m. The observed waves showed depth-integrated horizontal kinetic energy between 1 and 7 kJ m^{-2}, with an average of 1.6 kJ m^{-2}, and a typical group velocity of 40 m d^{-1}. These observations imply an average energy flux of 3 mW m^{-2} at the mixed layer base decreasing to approximately 25% of that value at 1500 m. Simulations of near-inertial surface currents forced with reanalysis winds along each float track agree with observed surface currents from EM-APEX, provided that mixed layer depth is restricted to the layer of weakest observable stratification, interpreted as the maximum depth which remains mixed over an inertial period. Simulations using the Price-Weller-Pinkel model, which permits time varying stratification, provides a better match to the observations; emphasizing the importance of near-surface stratification in amplifying wind power input. These simulations indicate an average wind power input of 3

mW m^{-2} in the eastern Pacific sector of the Southern Ocean.

The thickness of the active mixing-layer, the turbulent layer in contact with wind stress, is needed to accurately estimate wind power input. Vertical shear, Langmuir cells, and buoyant convection were investigated as possible mechanisms for maintaining turbulent mixing within the mixing-layer. Over 90% of the observed variance of the mixing-layer thickness is explained by either shear-driven entrainment, which is simulated using the Price-Weller-Pinkel model, or by a parameterization of downwelling plumes due to Langmuir cell convergence. In general, surface buoyancy fluxes are too weak to drive mixed-layer turbulence. The density profiles shown here indicate that a fine-density threshold between the finest possible criterion of 0.002 kg m^{-3} and the previous finest criterion of 0.01 kg m^{-3} is needed to better diagnose the surface mixed-layer thickness. The results of wind driven simulations suggest that this criterion is 0.005 kg m^{-3}. Comparison of National Oceanographic Data Center (NODC) climatological mixed-layer thickness to those determined using the 0.005 kg m^{-3} density threshold suggests a multiplicative seasonally varying correction of 1.5 to 3.5 should be applied to estimates of wind work made using the NODC climatological mixed-layer thickness in the Southern Ocean.

The vertical structure of the inertial-band of the internal wave field was observed by EM-APEX in the eastern Pacific, Scotia Sea, and western Atlantic sectors of the Southern Ocean. Downward propagating internal wave variance is shown to vary with the seasonal cycle in both wind stress and surface mixed-layer depth. Mixed-layer depth was found to inhibit the formation of near-inertial waves in the Pacific during the austral winter. Inertial-band internal-wave energy in the Scotia Sea is dominated by upward propagating waves, likely generated by interaction of the strong currents found in this region with rough seafloor topography. Inertial-band internal wave energy in the Atlantic was observed to vary with the seasonal cycle in near-inertial wind-stress.

Diapycnal diffusivity in the 300 to 1500 m depth range, estimated using observed vertical shear in the Gregg et al. (2003) parameterization, is $1.96\pm0.36\times10^{-5}$ m^2 s^{-1}, $1.08\pm0.08\times10^{-4}$ m^2 s^{-1}, and $7.96\pm1.17\times10^{-5}$ m^2 s^{-1} in the eastern Pacific, Scotia Sea,

and western Atlantic sectors of the Southern Ocean. In the eastern Pacific and Scotia Sea these values similar to direct observations of diapycnal diffusivity inferred from the vertical spread of tracer in the Diapycnal and Isopycnal Mixing Experiment in the Southern Ocean.

TABLE OF CONTENTS

LIST OF FIGURES

Figure Number Page

LIST OF TABLES

ACKNOWLEDGMENTS

The scientific discovery in this dissertation represents original work, but would not have been possible if not for many past and present contributions to physical science and mathematics which provide the pillars upon which this and future research is constructed. The author would like to particularly acknowledge Isaac Newton, James Clerk Maxwell, Jean-Baptiste Joseph Fourier, and Thomas B. Sanford without whom the following observations and analysis would have been '*inconceivable*.' In addition, the author acknowledges the National Science Foundation for economic support of this research through grants OCE0623177 and OCE1129564.

DEDICATION

to the spirit of discovery, lest it be forgotten

Chapter 1

INTRODUCTION

1.1 Global significance of the Southern Ocean

1.1.1 Meridional overturning circulation

The global deep meridional ocean circulation (MOC) is driven by the convection of cold and saline waters in the North Atlantic and Antarctic regions. These deep water masses, styled by oceanographers as North Atlantic Deep Water (NADW) and Antarctic Bottom Water (AABW) respectively, flow from their source regions along the sea floor and are slowly incorporated into the pelagic interior.

North Atlantic Deep Water is transformed in the Southern Ocean where it is either mixed and recirculated into Upper Circumpolar Deep Water (UCDW) or Lower Circumpolar Deep Water (LCDW). In the former case, NADW mixes with less dense water and returns to the ocean interior at mid-depth and in the latter case, NADW mixes with dense AABW and returns to the sea floor. The rate at which NADW is transformed in these overturning branches is controlled by diapyncal diffusivity, which is driven by turbulent dissipation of energy at fine scales (McComas and Müller, 1981). A consequence of the dependence of diapycnal diffusivity on internal wave driven dissipation is that the strength of the MOC is at least partially controlled by the internal wave field in the Southern Ocean. This research on the topic of internal wave variability near the Coriolis, also referred to as the inertial, frequency seeks to establish the contribution of near-inertial internal waves to diapycnal diffusivity, and through that interior upwelling, in the Southern Ocean and to illuminate the physical processes driving the generation and distribution of these waves.

1.1.2 The Diapycnal and Isopycnal Mixing Experiment in the Southern Ocean

The research described in this dissertation was completed in support of the Diapycnal and Isopycnal Mixing Experiment in the Southern Ocean (DIMES). DIMES was a large inter-

national study involving many researchers in the United States and the United Kingdom. The experiment consisted of theory, simulations, and observations of the horizontal and vertical structure of the Southern Ocean. The goal of the experiment was to "... obtain measurements that will help us [*sic*] quantify both along-isopycnal eddy-driven mixing and cross-isopycnal interior mixing." The core of the field campaign was composed of the release and subsequent sampling 76 kg of CF_3SF_5 tracer into the eastern Pacific sector of the Antarctic Circumpolar Current (ACC) along the 27.9 kg m^{-3} neutral density surface between the Subantarctic and Polar Fronts of the ACC near 107°W and 58°S Ledwell et al. (2011). In complement to the tracer release, a panoply of autonomous floats, Lagrangian drifters, and moorings were deployed to observe the vertical and horizontal structure of the ACC along the tracer trajectory. The research described in the following sections was largely developed from the analysis of a subset of these measurements from nineteen electromagnetic autonomous profiling explorers (EM-APEX).

1.2 Internal waves

Much of the vertical structure of the ocean interior away from boundaries is attributable to freely propagating internal gravity waves (Gregg, 1976). Internal waves are described mathematically by their intrinsic frequency ω, and wavevector $\vec{k}$. Phase velocity $\vec{C}_p = \frac{\omega\vec{k}}{|\vec{k}|^2}$, the propagation direction of wave crests, is orthogonal to group velocity $\vec{C}_g = \frac{d\omega}{d\vec{k}}$, the direction of energy propagation, in internal waves. Freely propagating internal gravity waves transport energy away from their generation sites in the direction of $\vec{C}_g$ according to, $\vec{F} = E\vec{C}_g$, where $\vec{F}$ is the energy flux vector and E is the wave energy. The frequency range of internal waves is determined by the dispersion relation

$$\omega^2 = \frac{k_z^2}{|\vec{k}|^2} f^2 + \frac{k_H^2}{|\vec{k}|^2} N^2 \tag{1.1}$$

(Kundu, 1990), where k_H and k_z are respectively the horizontal component and vertical component of the wavevector, $f = 2\Omega\, sin(latitude)$($\Omega$ is the Earth's angular velocity) is the Coriolis frequency, and $N = \sqrt{\frac{-g}{\rho}\frac{d\rho}{dz}}$ is the buoyancy frequency. The right hand side of equation 1.1 shows that, because $\frac{k_z}{|\vec{k}|}$ and $\frac{k_H}{|\vec{k}|}$ are never greater than one, the intrinsic wave

frequency of internal gravity waves is constrained between the Coriolis frequency f and the buoyancy frequency N. The dispersion relation highlights an important feature of internal waves near the inertial frequency. When $\omega \approx f$ then $|\vec{k}| \approx k_z$ indicating that the horizontal scale λ_H is much greater than than the vertical scale λ_z, and that the wavevector $\vec{k}$ and phase velocity $\vec{C_p}$ are nearly vertical.

Internal waves near the inertial frequency are sufficiently common in the ocean (Elipot and Lumpkin, 2008a) that they are thought to dominate both the energy and shear of the internal wave field (Garrett, 1999). Near-inertial motions have been extensively studied because of their ubiquity, role in energy transport, and contribution to mixing. A long and detailed history of research on the topic provides the foundation for the various sections of this research. Internal waves near f are typically generated at the ocean surface by wind (Webster, 1968; Pollard and Millard, 1970; Gill, 1984). The initial large scale surface response decays into smaller cells due to variation in f (β dispersion) and due to mesoscale vorticity ζ creating spatially varying $f_{eff} = f + \zeta/2$ (D'Asaro, 1985; Kunze, 1985; D'Asaro et al., 1995). A fraction (determining this fraction is a topic of ongoing research) of near-inertial mixed-layer kinetic energy radiates as propagating near-inertial internal waves (Gill, 1984; Munk and Wunsch, 1998; Alford, 2001, 2003).

As internal waves of relatively low frequency propagate poleward, they approach their 'turning latitude', where the intrinsic frequency equals the local Coriolis frequency. Because internal wave frequency is bounded at f, waves cannot cross this boundary and are refracted equatorward. The turning latitude is often close to the generation region because, outside of tides, there are few mechanisms generating low frequency internal waves in the open ocean. As a result, most wind-generated near-inertial waves eventually propagate equatorward and downward due to the aspect ratio of the wavevector. Observations of near-inertial waves in this study and others suggest that individual wave packets persist for several weeks. Ray tracing solutions of near-inertial waves with typical $\vec{k}$ ($|k_z| \approx 5{\times}10^{-3}$ cpm) and ω near f in the Southern Ocean indicate that horizontal C_g is typically much less than the background geostrophic velocity. Given the weak (estimates of) C_g, this amount of time is insufficient for a wave packet to propagate a significant distance from the generation site. This is advantageous for the purpose of sampling internal waves using profiling floats as the

trajectories of drifting autonomous instruments and wave packets diverge slowly.

1.3 Overview of the dissertation

The research presented here is sub-divided into three distinct processes, each detailed in one chapter. Chapter two describes highly resolved observations of a storm at sea and the following near-inertial current response and extrapolates the analysis to infer the wind power input in a float-following sense. The consequences of estimating wind power input using six-hourly gridded wind products and constant mixed-layer depths are investigated (Kilbourne and Girton, 2015a). The third chapter deals with the identification of the active-mixing layer thickness, which is defined as the thickness of the layer in direct contact with surface wind-stress. The consequences of mis-estimating mixing-layer thickness, and corrections to previous estimates of wind power input in the Southern Ocean are discussed (Kilbourne and Girton, 2015b). Chapter four details observations of vertical finestructure made by EM-APEX floats in the Southern Ocean. Inertial-band variability was isolated from vertical profiles of horizontal velocity. The inertial-band variability was compared with available gridded global wind, satellite altimetry, and high-resolution topography to identify the processes controlling the generation and distribution of energy in inertial-band motions. These observations of inertial-band vertical finestructure were used to estimate upper-ocean interior diapycnal diffusivity along the DIMES tracer path for comparison with direct observations of diapycnal diffusivity from the tracer.

Chapter 2

QUANTIFYING HIGH-FREQUENCY WIND ENERGY-FLUX INTO NEAR-INERTIAL MOTIONS IN THE SOUTHEAST PACIFIC

2.1 Introduction

[1] The study of near-inertial oscillations and internal waves began with the advent of moored self-recording current meter measurements in the 1960's. These instruments revealed considerable variance near the local inertial frequency (Webster, 1968) and motivated a series of efforts to better understand near-inertial variability, its predominant generation mechanisms, and its role in other ocean processes such as diapycnal mixing and energy transport: Pollard and Millard (1970) found that the ocean surface mixed-layer responds like a damped harmonic oscillator to impulsive wind forcing if momentum is assumed to diffuse instantaneously throughout the surface mixed layer (*i. e.*, the layer acts like a solid, rather than a liquid, at timescales long relative to turbulence but short relative to the general circulation and mesoscale eddies). D'Asaro (1985) used this "slab" model to estimate the average wind energy-flux from several long-term wind recording moorings surrounding North America. Alford (2001), Watanabe and Hibiya (2002), and Alford (2003) expanded the use of the slab model to estimate the global flux using long term global reanalysis surface winds. Since then, a number of studies have investigated the sensitivity of the global wind-work calculation to the properties of the input fields and mixed-layer climatology (Jiang et al., 2005; Rimac et al., 2013). Direct connections between observations and simulated currents have remained elusive (Alford et al., 2012).

The Diapycnal and Isopycnal Mixing Experiment in the Southern Ocean (DIMES) is a long-term international tracer-release experiment designed to investigate interior mixing in the Antarctic Circumpolar Current (ACC). The studied area extends from the relatively

[1]This chapter was published as, Kilbourne, B. F., and J. B. Girton, 2015: Quantifying high-frequency wind energy flux into near-inertial motions in the southeast pacific. *Journal of Physical Oceanography* 45, 369-386.

weak and diffuse region of the ACC found in the eastern South Pacific to the more constricted and energetic currents of the Scotia Sea and the South Atlantic. The ship observations presented here come from the first field expedition of the experiment aboard the R/V Roger Revelle in January 2009 and returned late February 2009 (Fig. 2.1). This cruise was tasked with the deployment of profiling floats, RAFOS floats and sound sources, the CF_3SF_5 tracer release, and initial tracer sampling (Ledwell et al., 2011). The cruise covered a wide swath of the eastern South Pacific sector of the ACC. On 7 February 2009 the ship weathered a strong storm. This provided an excellent case study for wind generation of mixed-layer near-inertial oscillations (NIOs) and downward-propagating near-inertial waves (NIWs). Three Electro-Magnetic Autonomous Profiling Explorer (EM-APEX) floats deployed during the cruise and active from February through November 2009 show evidence of downward-propagating near-inertial internal wave packets. The energy contained within observed wave packets, and its relationship to the surface wind-stress, is investigated in this study.

Section two describes the wind and current data used in the analysis. Section three describes the methods used to model the surface response to wind and to interpret float velocity profiles. In section four the results from one-dimensional mixed-layer models are shown and compared with the results from EM-APEX observations. Sections five and six discuss these results and their contribution to global wind energy-flux estimates.

2.2 Data

Data for this analysis comes from (i) the now defunct QuikSCAT satellite, (ii) National Center for Environmental Prediction (NCEP) reanalysis wind, and (iii) Cross-Calibrated Multiplatform (CCMP) wind, (iv) profiling Lagrangian EM-APEX floats, and (v) ship-based meteorological, (vi) ship-based conductivity, temperature, and depth (CTD), and (vii) ship-based Acoustic Doppler Current Profiler (ADCP) measurements.

2.2.1 Observed wind and currents

Two vector-measuring wind sensors mounted on the bow and main masts of the ship recorded winds every 30 s. A hull-mounted Teledyne-RDI 150kHz acoustic doppler current profiler (ADCP) was used to measure water velocity between 29 and 200 m. The

ADCP is sensitive to sea-state (due to bubbles beneath the transducers) and the presence (or absence) of scatterers in the water column. Its range was limited during the times of peak winds due to bubbles under the hull and during daylight due to the diel migration of zooplankton (scatterers). The ship stayed within a 48km square region from 3 to 10 February 2009. The majority of this time was spent within a smaller 10km radius (Fig. 2.1B). The location was chosen for its weak tides and geostrophic currents which were confirmed by an initial hydrographic survey of the region. Weak background currents combined with the assumption that NIOs have a horizontal scale of at least 50 km (size of the survey region) allow for the reasonable treatment of the ADCP current record as stationary.

2.2.2 Gridded winds

We use National Centers for Environmental Prediction (NCEP) blended sea winds (Zhang et al., 2006) and Cross-Calibrated MulitPlatform (CCMP) ocean surface winds (Atlas et al., 2011) in three distinct comparisons. These products were interpolated onto the ship position to compare with in-situ measurements. A subset of this ship-following time series was sampled between 3 and 10 February 2009 to simulate the observed storm. CCMP winds were interpolated onto the float trajectories to drive a float-following slab model to estimate the ability of these products to reproduce surface oscillations over longer time scales.

Gridded QuikScat satellite data show the storm was a large diffuse cyclone spanning 30^o of longitude. This storm organized around a low pressure center just before it passed the ship's location and its cyclonic structure persisted for 2 days before dissipating into a disorganized wind field. Examination of a ten-year CCMP wind time series at 58^oS and 108^oW shows storms with wind speed in excess of 20 m s^{-1} are common with an average occurrence of once every ten days. QuikSCAT global images show a near-constant chain of large cyclones across the South Pacific. The strong winds and rotation near the inertial frequency made this storm an excellent candidate for the study of wind generation of mixed-layer near-inertial motions.

2.2.3 EM-APEX profiling floats

Vertical profiles of horizontal velocity were obtained by EM-APEX floats. These floats measure the horizontal electric current produced by the motion of seawater through Earth‘s magnetic field (Sanford et al., 2005). The floats are autonomous and typically collect about 300 vertical profiles before exhausting battery power. The data is relayed back for processing through the Iridium satellite network. In addition to velocity measurements, the floats are equipped with an SBE 41 CTD. The floats record horizontal velocity, conductivity, salinity, and pressure every 25 s, corresponding to a depth resolution of 2-3 m (Sanford et al., 2005). These floats were programmed to profile in bursts such that ascending profiles are separated by one half the local inertial period, in this case about 7 hours (Fig. 2.2). The floats also transmit surface location (from GPS), time, and various performance metrics. Details of post processing techniques used to convert raw data into water velocities are described in Sanford et al. (2005). Each velocity datum has an associated error estimate which represents the residual signal amplitude after processing. Data with error greater than 0.01 m s^{-1} were removed.

2.3 Methods

The goal of this work is to clarify the connection between high-frequency winds and subsurface near-inertial wave activity. We therefore require (a) a thorough understanding of the spectral and statistical properties of the wind products, (b) a model for the upper-ocean forcing process, and (c) a way to diagnose downward-propagating internal wave energy, both from the rotary-spectral properties of velocity profiles and from half inertial differences of pairs of profiles. Each of these is discussed below.

2.3.1 Wind time series

Smoothing and subsampling the ship wind

High-resolution observed winds (30s sampling) were smoothed with a six hour running rectangular filter and subsampled to six hour resolution for comparison with the gridded products (Fig. 2.3). The smoothed and subsampled wind was used to assess the impact

of the six hour time resolution inherent in the gridded wind products on spectral levels (Fig. 2.4A) and air-sea energy flux. These fully resolved and smoothed ship-wind records are referred to hereafter as SW and SSW.

Spectral analysis of wind time series

The rotary power spectrum of wind speed was computed for each of the four wind time series (CCMP, NCEP, SSW, and SW) (Fig. 2.4A). The full 40-day record from 12 January to 20 February 2009 was separated into 15 five-day half-overlapping windows. The coherence between the gridded products and the smoothed subsampled ship wind was computed using the same five-day window (Fig. 2.4B).

2.3.2 Mixed-layer models

The upper-ocean response was modeled using two 1-D mixed-layer models; the Price-Weller-Pinkel (PWP) and the damped-slab models (Pollard and Millard, 1970; D'Asaro, 1985; Price et al., 1986; Plueddemann and Farrar, 2006). The slab model is desirable for its simplicity but replaces important physics with simple parameterizations. It cannot simulate or accommodate the sudden changes in mixed-layer depth seen during strong forcing and the radiation of near-inertial energy by internal waves is parameterized through a damping coefficient. The first of these limitations is remedied by the PWP model (Price et al., 1986), which includes physically-based vertical mixing of momentum and buoyancy but continues to neglect the lateral gradients responsible for wave radiation. PWP lacks the numerical simplicity and possibility of analytic solution. Longer PWP simulations require high-frequency heat and freshwater fluxes. These are unavailable and limits PWP's use to brief simulations of a single storm event. Comparison between the two models here is a vital step for evaluating the importance of mixed-layer depth evolution during a forcing event. We focus on the ocean mixed-layer response from 3 to 10 February 2009 (Fig. 2.5). Wind speed was converted to stress using speed-dependent drag coefficient (Large and Pond, 1981). Both models were initialized at rest. The PWP model was initialized with a temperature and salinity profile from the ship's CTD on 3 February 2009.

Slab model

The inertial current response equation ((D'Asaro, 1985))

$$\frac{d\vec{Z}}{dt} = -\omega\vec{Z} + \frac{\vec{T}}{H} \tag{2.1}$$

where

$$\vec{T} = \frac{\tau_x + i\tau_y}{\rho} \ , \tag{2.2}$$

$$\omega = r + if \ , \tag{2.3}$$

and

$$\vec{Z} = u + iv \ , \tag{2.4}$$

was solved using the integrating factor method (appendix A) to obtain

$$\vec{Z} = \frac{\int e^{\omega t}\frac{\vec{T}}{H}dt}{e^{\omega t}} \ . \tag{2.5}$$

τ_x, τ_y and u, v are the east and north components of wind stress on the ocean surface and the ocean surface currents respectively, H is the mixed-layer depth, and ρ is the density of seawater. f is the Coriolis frequency defined as $2\Omega sin(\theta)$ where Ω is the rotation rate of the Earth and θ is latitude. Energy radiation from the mixed layer is parameterized using a damping factor $r = 0.04\,|f|$ (determined empirically by fitting model output to ADCP currents).

Price-Weller-Pinkel model

The PWP model (Price et al., 1986) was originally developed to model the influence of heat, salt, and momentum fluxes on the diurnal cycle of upper-ocean stratification at the ocean surface. PWP uses forward time-stepping to evolve upper ocean temperature, salinity, and velocity with depth. We used a 900 s time-step and 5 m depth levels to 300 m. For better comparison with the slab model, our implementation of the PWP model also included the

linear drag/wave-radiation parameter $r = 0.04|f|$. Though numerically more complex than the slab model, the ability to simulate changes in mixed-layer depth due to wind forcing makes PWP an important component of this study. Buoyancy fluxes were not included to facilitate comparison between the models, and so this approach is limited to short (single wind event) simulations; in the absence of restratifying buoyancy fluxes, mixed-layer depth can only increase.

Mixed-layer depth

Mixed-layer depth H is important for accurately modeling the amplitude of the ocean current response to wind variations. When H is constant, $|\vec{Z}|$ scales as $1/H$. For the storm-response period, the slab model mixed-layer depth was held constant at 80 m, which matches vertical density profiles near the time of the storm. Other slab model studies have used smoothed or climatological mixed-layer depths (Alford, 2001; Plueddemann and Farrar, 2006). These time varying mixed-layers accurately modulate the seasonal cycle of mixed-layer current amplitude but do not change quickly to simulate a storm response. This leads to poor simulation of current speed for any particular storm. Underestimating the mixed-layer depth will result in overestimating wind work. Our choice of a constant mixed-layer depth simplifies the analysis and is motivated by the presence of slab like inertial oscillations to 80 m in the pre-storm period and by post-storm vertical density-profiles. This choice also minimizes root-mean-square difference between model and ADCP currents. As seen in Fig 2.5B, stratification and shear are present throughout the upper 80 m highlighting inherent inaccuracy of the slab (instantaneous vertical mixing) approximation. In the PWP model mixed-layer depth evolves through shear instability parameterizations. This allows PWP to better simulate currents while the mixed-layer is deepening.

Isolating the inertial-band model response

We chose not to separate the inertial component from the model output using the substitution $Z = Z_I + Z_E$ into equation 1, where $Z_E = \frac{T}{\omega H}$ (D'Asaro, 1985). This method removes instantaneous "Ekman" variance from the inertial band (because of the drag term in ω)

which diminishes the integrated wind-work. The frequency domain solution (Alford, 2003) addresses this by using a frequency dependent damping $r(\sigma)$ where low frequencies have no component in the direction of the wind and thus do not impact $\vec{\tau} \cdot \vec{Z}$. The frequency-domain solution is difficult to implement for short time series as poor frequency resolution creates artifacts in the solution. In place of frequency-domain solution we broadly high-pass the model output using a 57 hour (four times the inertial period) filter. This approach removes low-frequency "Ekman" currents while retaining all near-inertial variance.

Wind energy flux

The slab and PWP models were forced with each wind-stress time series. Energy flux

$$\Pi_w = \vec{\tau} \cdot \vec{Z}_I \tag{2.6}$$

and work

$$P = \int \Pi_w dt \tag{2.7}$$

were computed using the inner product of wind-stress with high-passed surface currents (D'Asaro, 1985). Observed wind flux was computed between the surface wind and currents at 29 m depth, the shallowest available ADCP time series. We expect the 29 m currents are representative of the surface conditions.

Error of energy-flux estimates

These wind-work estimates are highly sensitive to both the methods used to obtain them and the data from which they are obtained, evidenced by the large scatter in results (Table 2.1). The flux computation $\vec{\tau} \cdot \vec{Z}$ is quite sensitive to the phasing of the wind and currents. six-hourly forcing is often unable to reproduce the exact phasing of observed wind. Mixed-layer depth is a further source of error in these estimates, in the slab-model the work is proportional to $1/H$. The mixed-layer depth can be tuned to minimize the error between the observed and modeled currents (as we have done here). This favors a deeper slab model mixed-layer as the data is fit to post-storm (deeper mixed-layer) currents. The vast majority of the wind-work is done at the onset of the storm (Fig 2.5). Tuning the mixed-layer depth

to reproduce the observed energy-flux results in a more shallow layer. This highlights the importance of the initial stratification in determining the wind-work. Peak wind for this storm varies from 21 to 33 m/s. Here we use a speed dependent drag coefficient which ignores sea-state (Large and Pond, 1981) to derived the stress. It should be noted that the peak stress corresponds with large surface waves. This further compounds the uncertainty of the wind-stress used here. Given these sources of error any confidence limits on the wind-work results seem quite arbitrary. A better criterion to validate the model response is to compare with the ship's ADCP, as we have done.

Monte Carlo methods were used to better estimate the effects these uncertainties introduce into the integrated wind work. Each winds-stress time series was randomized with a gaussian noise of an amplitude set by its root-mean-square difference with the fully-resolved wind. Integrated wind-work was computed for each realization. The values from ± 2 standard deviations from the ensemble mean are shown in table 2.1 as the 95% confidence limits.

Float-following slab model

Over the nine-month deployment of the three EM-APEX floats, the upper-ocean stratification changed gradually (Fig. 2.6). CCMP winds were sampled along the EM-APEX drift trajectories to produce float-following wind time series. These winds were used to force the slab model. Coriolis frequency variations due to the moving model domain were included (though are not a large effect). Mixed-layer depth interpolated from monthly, ARGO-based climatology (de Boyer Montégut et al., 2004) gave similar values to those derived from the EM-APEX float CTD measurements. Float profiles and climatology both show winter mixed-layer depths in excess of 400 m, but density-compensating temperature and salinity variance indicate that these deep 'mixed' layers are not actively mixing. This suggests these depths do not represent the vertical extent of wind-forced inertial oscillations and should not be used with the slab model. Average turbulent vertical velocities derived from wind-stress time series (D'Asaro, 2001) indicates the timescale of vertical momentum transport in deep mixed layers is often greater than half of the inertial period. It is unlikely that wind-driven

turbulent vertical momentum transport could drive the near-instant current response assumed in the slab and PWP models over such a large vertical range. In consideration of this we constructed a mixed-layer depth time series based on weak stratification seen in the float record. The average monthly mixed-layer depth was chosen as the depth where monthly-average buoyancy frequency begins to increase (Fig. 2.6).

2.3.3 Identifying near-inertial internal waves

Half-inertial differencing

The EM-APEX burst profiling was designed to collect repeat measurements at half the local inertial period. The difference between half-inertial spaced profiles ($\vec{Z}_1$ and $\vec{Z}_2$ represent the two profiles as complex valued current vectors) serves as a crude bandpass filter (Leaman and Sanford, 1975) to determine the of the near-inertial band current

$$\vec{Z}_{I_{float}} = \frac{\vec{Z}_2 - \vec{Z}_1}{2} \ . \tag{2.8}$$

The result of this operation applied to a velocity profile showing a likely near-inertial wave is shown in figure 2.7. This method works well as long as inertial signals dominate, but it is vulnerable to aliasing of higher frequencies. For example, simulations indicate M_2 variance, if present, is aliased into the half-inertial difference. However, a frequency spectrum from the ship ADCP time series (not shown) indicates that near-inertial variance is much greater than M_2 in this data. As a test of the half-inertial method, we have also made use of additional profiles collected by the EM-APEX to construct a high-passed view of currents (not shown) by removing the burst average velocity profile. The extent to which half-inertial differences and high-passed profiles, which include all measured internal wave variance, agree is evidence that the near-inertial band dominates high-frequency motions in this sector of the Southern Ocean. This agreement strengthens the argument that downward propagating beams (Fig. 2.8) are indeed near-inertial wave packets.

We identify downward-propagating, near-inertial waves in the EM-APEX velocity profiles based on the following criteria: mirror-imaging in half-inertial pairs indicating a dominance of inertial-band energy (Sanford, 1975), clockwise rotation of horizontal velocity with

depth (Leaman and Sanford, 1975), and downward progression of kinetic energy maxima over time (Rossby and Sanford, 1976) (Fig. 2.8). The relationship of these downward-propagating wave packets to the wind-forcing and mixed layer inertial oscillations is discussed in the results section.

Single wave packet spectral analysis

A wave packet observed by three floats from 20 February to 31 March 2009 was selected for a more focused analysis of vertical structure and downward energy flux. The 2000 m record was separated into seven half-overlapping 500 m segments. For each data segment a linear fit was removed from the record and the Hamming tapering window (a modified cosine window) was applied to the data (Harris, 1978; Welch, 1967). Directional and rotary shear spectra were calculated in each segment (Leaman and Sanford, 1975). Spectra were then time-averaged in each depth range (Fig. 2.9).

To characterize the rotary polarization of the float data individual full-depth rotary spectra were integrated to determine the CCW/CW variance ratio

$$\frac{\int_{k_z^+} S dk_z}{\int_{k_z^-} S dk_z} \tag{2.9}$$

(S is the rotary shear spectrum, k_z is vertical wavenumber). When near-inertial wave packets are present this ratio ranges from 5 to 35 (Fig. 2.10) consistent with expectations for downward propagating NIWs.

2.4 Results

2.4.1 Wind products

Comparison of the two reanalysis products NCEP and CCMP with the filtered, decimated ship wind time series (SSW) shows good correlation (Fig. 2.3), with CCMP matching the observations more closely than NCEP except at the point of strongest wind. Root-mean-square scatter of NCEP and CCMP around the observations is 10.2 and 6.1 m s^{-1}, respectively, in rough agreement with validation statistics (Atlas et al., 2011).

All three low-resolution (*i. e.,* six-hourly) wind time series are reduced in amplitude (relative to SW) at frequencies above 1 cycle day^{-1} (Fig. 2.4). In the case of the degraded

ship-wind time series (SSW), this can be partially explained by the spectral response of the six hour boxcar (running mean) filter applied before decimation to six hour sampling. Such a filter has a $\mathrm{sinc}^2(pf)$ behavior (for filter width p and frequency f), resulting in a reduction factor in spectral level at the inertial frequency of 0.53 (intersection of the dashed and solid lines in Fig.2.4. Interestingly, the difference in spectral level between the six hour and fully resolved spectra is roughly a factor of 4, the filter response makes up slightly less than half the attenuation of variance at f. The similarity of the NCEP and CCMP spectral levels to the SSW suggests that their levels are also influenced by a similar filter (though likely one more complex than a simple rectangular window). Gridded winds are coherent with observed winds to just over 1 cycle day^{-1}, but are not significantly coherent at the inertial frequency (Fig. 2.4). The drop in coherence corresponds to the frequency at which the spectral levels of NCEP and CCMP become significantly different from spectrum of SW.

2.4.2 Model results

Ship observation period

During the period of the storm and upper-ocean response observed by the *R/V Revelle*, both the slab and PWP models are able to largely reproduce the wind-forced evolution of the near-inertial currents (Fig. 2.5), with PWP additionally simulating deepening of the mixed-layer. A difficulty for the models is reproducing the initial mixed-layer response to the strongest wind. Initial currents quickly deepen the mixed-layer leading to a steep initial decline in current amplitude. PWP performs better in this respect but underestimates the full strength of the initial current response. In the wake of the storm the current direction and amplitude remain in fairly close agreement until the end of the observation period.

The simulated mixed-layer currents from all model scenarios were compared with ship-based ADCP observations. The result of these simulations is the integral $P = \int \vec{\tau} \cdot \vec{Z} dt$, the total work done by the wind on the internal wave-band ocean surface currents. A total wind work of 3.51 kJ was computed (Fig. 2.7) from observed winds and currents. SW give the most accurate results in both models. The wind work results for each model run are shown in Table 2.1. PWP wind-work estimates results are consistently higher than for slab model.

This is due to the constant mixed layer thickness used for the slab model. Mixing and deepening of the mixed-layer reduced the currents, bringing the observations and models into agreement after the storm.

Wind-work estimates from the various slab model runs vary considerably with the wind-forcing time series used (Table 2.1). Much of this variability can be attributed to a single point in the wind-forcing time series—the maximum wind-stress at the onset of the storm. At 1800 UTC 7 February 2009 wind speeds were 29.5, 23.7, 33.2 and 20.5 m/s for the CCMP, NCEP, SW, and SSW respectively, corresponding to wind-stresses of 2.53, 1.4, 3.56 and 0.95 Pa. Six hour resolution does not allow faithful reproduction of the wind variations over the course of the storm, which remained near the maximum speed for less than 2 hours. Depending on the timing of the samples, this can result in an over- or under-estimation of the rate of acceleration and rotation of the winds which impacts the overall momentum input. On average, the wind's near-inertial energy level reduction due to six hour filtering and/or sampling (described above and in Fig. 2.4) should be the dominant effect but for a single storm there is considerable uncertainty in the result. Monte-Carlo testing shows a range of 0.25 to 0.33 kJ m^{-2} simply from moving the starting point of the subsampling used to generate SSW. It is possible that different data assimilation and interpolation approaches used in NCEP and CCMP also have an influence, but the large single-storm uncertainty outweighs any systematic differences between these datasets. However, SSW slab model wind work (Table 2.1) is approximately 1/5 that from the SW due to a reduction in peak wind-stress. This is somewhat less than the 1/3 ratio between the globally-averaged wind work from six hour NCEP forcing and 1-hour forcing found by Rimac et al. (2013). However, the ratio of between highly SW and SSW forced PWP simulations is 0.4. If this wind-work reduction comes equally from a reduction in wind stress and mixed-layer currents, it would imply a $1/\sqrt{3} = 0.58$ reduction in wind spectral level—quite close to the 0.53 expected from a six hour filter, as described above.

Lagrangian / float-following slab-model

Longer-duration slab model simulations of mixed-layer motions (using CCMP winds interpolated to each float's trajectory) confirm that mixed-layer wind energy inputs occur around the time of each subsurface near-inertial wave packet observed by the floats. Additionally, the times are coincident with enhanced tracer-depth shear seen by Ledwell et al. (2011). The float-following slab output was compared to float-observed mixed-layer currents. A complicating factor is the treatment of mixed-layer depth in the Lagrangian model; this can be (a) held constant, (b) follow climatology (*e. g.,* de Boyer Montégut et al., 2004), or (c) be derived from float observations (which is done here). One of the greatest challenges to an observationally-based approach is that the definition of the mixed-layer typically used for large-scale climatology is not appropriate for wind-forced near-inertial current models. Here we construct a time series of mixed-layer depth using the payer of weakest monthly-averaged stratification (dashed line, Fig. 2.6). Additionally, two established mixed-layer criteria were applied to the data (Fig. 2.6) but both criteria fail to capture the weak stratification determining mixed-layer current response to the wind. As a result, they dramatically under-predict mixed-layer inertial oscillation amplitudes during the Austral winter.

The half-inertial differencing operation amplifies noise in the float measurements, resulting in a noise floor of 0.05 m s^{-1}. The empirical probability distributions of the model results and observations look quite similar (Fig. 2.11, inset). The Kolmogorov-Smirnov test, applied to these data above 0.05 m s^{-1}, indicates the modeled NIOs and float observations are drawn from the same underlying distribution at the 95% confidence level. Monthly means of both modeled and observed near-inertial amplitudes (Fig. 2.11) show a similar seasonal cycle, with the exception of excess observed energy in April 2009. The source of the excess energy is unknown but may be trapped NIWs. In April the floats were traveling near the northern (anticyclonic) flank of the Polar Front where trapping of sub-inertial NIWs is likely due to the strong vorticity (Kunze, 1985).

2.4.3 Float observations of downward propagating waves

Near-inertial wave packet case study, March 2009

We estimate that the storm on 7 February 2009 input 3.51 kJ m^{-2} of kinetic energy into inertial motions in the ocean surface layer, and the 3 EM-APEX observed column-integrated kinetic energy over the following month at a level similar to this input (Fig. 2.8). The EM-APEX data during March 2009 are unique in that multiple floats sampled the same wave packet as they transited the outer edge of an anticyclonic eddy and remained within about 10 km of one another. The burst sampling executed by the floats yields at best 4 evenly-timed current observations at a given depth. These data are insufficient to exactly determine the wave's intrinsic frequency, but plane wave fits indicate the frequency of the observed waves is not more than 2% greater than the local inertial frequency. Downward energy-flux within the packet, diagnosed by combining the energy density with a vertical group velocity 0f 40 m day^{-1} estimated from the downward slope of the packet over time (Fig. 2.8; March 2009), is above 1 mW m^{-2} at the depth of the largest current amplitude, decreasing below 900 m depth (Fig. 2.12). The CCW (downward energy propagation) rotary wavenumber spectrum of vertical shear from this period (Figs. 2.9, 2.10) is markedly peaked around 5×10^{-3} cpm (200 m vertical wavelength) in contrast to the CW spectrum (upward energy) which more closely matches the GM76 (Garrett and Munk, 1975; Cairns and Williams, 1976) model of the typical background internal wave field.

Vertical ray-tracing solutions (Kunze, 1985), assuming a horizontal scale of 20–30 km, show the wave as having been generated within 40 km of the observed location between 5 to 20 February 2009 (*i.e.,* likely by one of the two storms passing through the area on 7 and 19 February).

Half-inertial period differencing and kinetic energy

Over the 9 months sampled (February to November 2009), a series of downward-propagating near-inertial wave packets were observed by each float. The apparent downward trajectory of the amplitude peaks, combined with the dominance of counterclockwise rotation with depth indicates downward-propagating energy in these wave packets.

EM-APEX floats over the 9 months following the cruise show depth-integrated (0 to 1500 m) kinetic energy ranging from 1 to 7 kJ m^{-2} with a long term mean of 1.6 kJ m^{-2} (Fig. 2.8). The time-mean kinetic energy profile from all half inertial differences shows energy decreasing from 6 to 1.5 J m^{-3} over the measured depth range (Fig. 2.12). When combined with the 40 m day^{-1} group velocity observed from the March 2009 wave packet, this gives an energy flux of 3 mW m^{-2} at the mixed-layer base decreasing to 0.7 mW m^{-2} at 1500 m depth. However, our ability to quantify the vertical group velocity is poor making this estimate highly uncertain.

Shear and strain spectra of the near-inertial band

A rotary spectral decomposition was computed for each velocity profile. Increased variance near the 200 m wavelength is prominent in profiles with also exhibit elevated inertial-band currents in the time domain. The ratio of integrated rotary variance (Fig. 2.10) shows the predominance of energy in positive (CCW) wavenumbers. Shear spectra from profiles containing near-inertial wave signals are elevated at low wavenumber, significantly departing from the spectral levels predicted in the Garrett-Munk model of the typical background IW field. Depth windowing of velocity data from March 2009 shows the depth evolution of the rotary polarization 2.9. Near surface spectra are highly polarized with a CCW/CW ratio near 10. This ratio approaches 1 with increasing depth.

Strain spectra (not shown), computed from ascending CTD profiles, do not appear elevated in the corresponding wavenumber range. This is consistent with wave motion near the inertial frequency which is expected to be nearly horizontal.

2.5 Discussion

2.5.1 Gridded wind products

The six-hourly wind products cannot force a realistic one-dimensional model response due to their lack of high frequency variance. The 10 m wind spectrum is “red”, and near-inertial variance makes up a small fraction of total wind variance. Wind events of importance to NIO/NIW generation occur at and above the inertial frequency. All of the variance driving

near-inertial motion at relatively high latitudes occurs very near the Nyquist frequency of six hour products. Small-amplitude high-frequency winds constantly drive low amplitude inertial responses in the mixed layer. Integrated wind-work from fully resolved observations shows a gradual increase over time which is the result of high-frequency flux. In contrast the wind-work time series generated using six hour gridded-winds is dominated by large steps at higher strength wind events. Our comparison of ship wind to gridded products indicates that the spectral properties of gridded winds might be corrected with a by accounting for a six hour filter (Fig. 2.3A). Higher temporal resolution of wind is necessary to accurately model wind-energy flux.

2.5.2 Mixed-layer models

Comparison of wind work to previous estimates

Previous studies highlight the predominance of near-inertial band energy in the ocean surface (Elipot and Lumpkin, 2008b). The key results in the series of papers by Alford (2001); Watanabe and Hibiya (2002) are both the total integrated wind-flux estimate and its global distribution. These global estimates require wind and mixed-layer depth from reanalysis and climatology respectively. This study shows the energy flux, $\vec{\tau} \cdot \vec{Z}$, to be directly proportional to mixed-layer depth. Climatological mixed-layer depths significantly misrepresent the ocean response to impulsive wind forcing when upper ocean buoyancy gradient is small. This could lead to significant error in globally integrated wind-energy-flux estimates, we hope to address this further in future work. We also find that smoothing the highly resolved wind record with a six hour filter attenuates wind variance in the inertial band by a factor of 4, in rough agreement with a recent study on attenuation of wind variance by decimating in space and time (Rimac et al., 2013). The resulting energy-flux from our wind time series vary considerably, indicating that although two wind-stress time series can resemble one another statistically, they do not contribute the same energy into the ocean surface. Two factors are key in influencing the energy-flux, the wind-stress and the actively mixing depth at the onset of the storm. We cannot directly compare our results with previous energy-flux estimates because we have simulated one event, however these results show

estimates for one event are influenced by small variations in wind and mixed-layer depth.

Models forced with fully resolved wind were able to capture the initial storm response and, in a bulk sense, accurately predict the momentum-flux into the upper ocean using only a wind time series. Models forced with low-resolution time series did not perform as well. Model results could be made to fit the observations very well by fine-tuning the linear damping/radiation and mixed-layer depth terms at the expense of generality. Despite this, no one set of mixed-layer depth and damping parameters could reconcile results using low and high-frequency forcing. Ocean inertial currents are driven by sharp changes in the magnitude and direction of wind stress at and above the inertial frequency. Six-hourly wind time series either miss these brief impulse events completely and/or overestimate the temporal extent of peak winds. The result is a total wind work estimate that may be much higher (CCMP here) or lower (NCEP here) than the real ocean. During this time period the CCMP product over predicted wind-work, however at other times the results were opposite with the NCEP product over predicting wind-work. In both cases the results come down to a small number of data points during peak wind periods.

Lagrangian mixed-layer model

The slab model, forced with CCMP winds following the nine month float trajectories (Fig. 2.11), estimates an average energy flux into near-inertial currents of 3 mW m^{-2}. While monthly averages of modeled currents and float observations agree well, these data are not ideal for computation of the wind-energy flux into inertial oscillations. We have seen in our highly resolved case that the six hour winds can both overestimate and underestimate the real fluxes. The key to matching the modeled currents with the data became the identification of the mixed-layer depth. Our mixed-layer time series is motivated by near-surface variability in the float CTD data, but it is difficult to construct an objective algorithm which finds a similar trend. The reliance of these results on mixed-layer depth highlights both the current lack of understanding of the vertical distribution of near surface momentum transport and the sensitivity of the slab model to its parameterization.

2.5.3 Wave observations

The highest-amplitude near-inertial waves we observe here have a vertical wavelength near 200 m. Internal wave observations frequently occur in the narrow depth range of 500 to 1000 m near the base of geostrophic shear. This hints that these waves may be trapped by the horizontal eddy structure (modulating f_{eff}) and vertical (critical layer) shear. A topic for further study will be to model the three dimensional near-inertial wave ray-paths through a flow field resembling the observed background conditions. Observed wave packets appear to lag periods of energetic wind forcing making one-to-one correspondence between the subsurface waves and wind-driven mixed layer motions difficult to verify. These data highlight the complex three dimensional structure of the wave-field. Propagating waves appear at mid-depth throughout the EM-APEX record. Wave energy may preferentially collect in some regions (near fronts or within eddies) making observations more likely.

The decay in downward energy in the March 2009 wave packet (Fig. 2.12) could be interpreted either as being due to turbulent dissipation or simply as a lower boundary of a vertically-localized wave packet. If the former, a rate of 8×10^{-10} W kg^{-1} is inferred, which is considerably larger than the 1×10^{-10} W kg^{-1} found by the High Resolution Profiler measurements reported in Ledwell et al. (2011). Thus, a vertical limit of a transient event appears more likely. It is also possible that vertical group velocity decreases with depth. However, this is not clearly seen in the depth *vs.* time maps (Fig. 2.8).

2.6 Conclusions

This case-study of near-inertial wind forcing and downward energy propagation in the Southern Ocean illustrates several features of the upper-ocean forcing of internal waves that have long been suspected but have been difficult to observe in entirety. These include:

- the quantitative connection between episodic near-inertial wind work and the increase of kinetic energy in the mixed layer (Fig. 2.5 and Table 2.1);

- the sensitivity of wind-work calculations to the details of the wind time series, particularly the spectral level at the inertial frequency (Fig. 2.4), to the maximum wind

stress in an event, and to near-surface stratification;

- the radiation of the bulk of mixed-layer inertial energy in the form of downward-propagating near-inertial internal waves;

- the ubiquity of downward-propagating near-inertial wave energy in the upper 1500 m of the southeast Pacific sector of the Southern Ocean (Fig. 2.8); and

- the decay of the downward-propagating energy well above the deep-ocean bottom (Fig. 2.12).

The range in total wind work inferred from model runs forced by different wind products highlights the sensitivity of these models to both wind-stress peaks and temporal resolution. The slab model forced with smoothed winds produced just 21% of the wind-work found by the same model forced with fully resolved winds (2.1). Gridded wind products provide an excellent statistical picture of the scale and duration of large storms, but may not accurately reproduce the shape, location, and speed for any given storm, particularly in regions with little in-situ data such as the Southern Ocean. During the period ship-winds were available, January and February 2009, the CCMP product appears to do a better job of matching the observations and of creating a realistic model response, but this may simply be fortuitous.

From float velocity data, we observe downward-propagating features in kinetic energy. Analysis of these energetic periods shows counter-clockwise rotation with depth, consistent with downward-propagating near-inertial waves. A large fraction of the variance in these packets lies in the vertical wavenumber range 0.001 to 0.01 cpm (100 to 1000 m). The largest amplitude horizontal velocities are associated with wavenumbers near 0.005 cpm (200 m), usually occurring between 500 and 1200 m depth. This depth range coincides with increased buoyancy frequency at the base of the winter mixed layer (Fig. 2.6). Velocity profiles also indicate that the majority of the geostrophic shear in the ACC eddies and fronts decays with a scale of approximately 1000 m, suggesting the possibility that the observed waves are slowed and amplified as the background shear or vorticity decreases with depth Kunze (1985).

Over the full nine month EM-APEX observation period, both slab model wind-work and downward near-inertial energy flux are estimated at approximately 3 mW m^{-2}. Given the above caveats about gridded wind products the wind work may still be an overestimate, in spite of the fact that surface current amplitudes are well predicted by the slab model. Additionally, the downward flux estimate relies on the assumption of constant vertical group velocity and can only be regarded as a ballpark figure. Nevertheless, the agreement suggests that most of the near-inertial wind-energy input is able to radiate from the mixed-layer as propagating near-inertial internal waves.

2.7 Acknowledgments

We gratefully acknowledge the use of several freely available global datasets. NCEP Reanalysis 2 data were provided by the NOAA/OAR/ESRL PSD, Boulder, Colorado, USA. CCMP wind were provided by NASA/JPL PODAAC. The QuikSCAT data used in this study are distributed from the NASA/JPL PODAAC and Remote Sensing Systems. Sea surface altimeter products were produced by Ssalto/Duacs and distributed by AVISO with support from CNES. Thanks to Dr. Eric Kunze providing essential scientific and editorial advice. Useful comments were provided by Brian Chinn and Andy Pickering. Many thanks to the Captain and crew of the R/V Roger Revelle. This research was funded through NSF grants OCE0623177 and OCE1129564.

2.8 Appendix: Integrating factor solution to Pollard & Millard 's mixed layer current model

The ocean surface current response to wind stress is described by the simple set of equations

$$\frac{du}{dt} - fv = F - cu \tag{2.10}$$

and

$$\frac{dv}{dt} + fu = G - cv \tag{2.11}$$

(Pollard and Millard, 1970).

(F, G) are vector components of the wind, (u, v) are vector components of the ocean surface current, f is the Coriolis frequency, and c is a damping coefficient. The damping

term c represents radiation of energy away from the surface as internal gravity waves (F, G) are defined as

$$(F, G) = \frac{\rho_a C_D U^2}{\rho_w H_0} * (sin(\theta), cos(\theta)) \ . \tag{2.12}$$

C_D is the drag coefficient between water and air and $|U|$ is the 10 m (height above sea surface) wind speed. ρ_a and ρ_w are the densities of air and water respectively, θ is the wind direction, and H_0 is the mixed layer depth. Substituting the wind stress $\tau = \rho_a C_D U_i^2$ into 2.12, equations 2.10 and 2.11 become

$$\frac{du}{dt} - fv + cu = \frac{\tau sin(\theta)}{\rho_w H_0} \tag{2.13}$$

and

$$\frac{dv}{dt} + fu + cv = \frac{\tau cos(\theta)}{\rho_w H_0} \ . \tag{2.14}$$

Adding 2.13 to i*2.14 gives

$$\frac{dZ}{dt} + \omega Z = \frac{T}{H} \tag{2.15}$$

where $(\tau_x, \tau_y) = \tau * (sin(\theta), cos(\theta)), Z = u + iv, T = \frac{\tau_x + i\tau_y}{\rho_w}$, and $\omega = c + if$ (we drop the the subscript from H_0) (D'Asaro, 1985).

We refer to 2.15 as the "slab" mixed-layer model; it is a linear inhomogeneous first order ordinary differential equation of the type $\frac{df}{dx} + P(x)f = Q(x)$. A solution to this type of equation can always be found using an integrating factor (Bender and Orszag, 1978). A common technique used in the solution of 2.15 is the Fourier transform . The Fourier solution is inappropriate for very brief simulations because resolution in the frequency domain is $1/L$, where L is the simulation period. The integrating factor solution is advantageous in this study for two reasons: (1) the solution is exact over short simulation periods and (2) the general solution highlights the dependence of inertial currents on the mixed-layer depth.

To apply this method to the slab model we first multiply each term in 2.15 by $M(t)$ to yield

$$M(t)\frac{dZ}{dt} + \frac{dM(t)}{dt}Z = M(t)\frac{T}{H} \; . \tag{2.16}$$

Combining the derivatives in 2.16 and integrating both sides results in

$$M(t)Z(t) + k = \int M(t)\frac{T}{H}dt \; . \tag{2.17}$$

2.17 can then be rearranged to isolate the surface current response

$$Z(t) = \frac{\int M(t)\frac{T}{H}dt}{M(t)} + k \; . \tag{2.18}$$

Solving 2.18 for the general form of $M(t)$ is straightforward. Dividing

$$M(t)P(t) = \frac{dM(t)}{dt} \tag{2.19}$$

and integrating to obtain

$$\int P(t)dt + l = ln(M(t)) \tag{2.20}$$

results in the general form for the integrating factor

$$M(t) = e^{l}e^{\int P(t)dt} \; . \tag{2.21}$$

In the slab model, $P(t) = \omega(t)$ and if ω is typically constant so that $M(t) = e^{l}e^{\omega t}$. Substituting 2.21 into 2.17 gives the general analytic solution to the slab model

$$Z(t) = \frac{\int e^{\omega t}\frac{T}{H}dt}{e^{\omega t}} + k \; . \tag{2.22}$$

The slab model has a particular analytic solution whenever $\int e^{\omega t}\frac{T}{H}$ is integrable. When this is not the case, for example when T is computed from natural wind data, this solution is a computationally efficient method relative to an iterative time-stepping solution. Numerical integration of 2.22 becomes difficult when $e^{\omega t}$ becomes large because both numerator and denominator approach the limits of double-type precision. This limits the utility of the technique to relatively short periods.

This solution technically allows for a time-varying mixed-layer depth. While 2.22 can still be evaluated with $H = H(t)$, this does not explicitly conserve momentum in the mixed-layer. For example, if a mixed-layer deepened by a factor of two under increased wind-stress this would not dampen the surface currents and would effectively double the momentum in the model domain. Slowly varying $H(t)$, as is used here in the float-following model, has little effect on the momentum budget over short-time scales.

With constant mixed-layer depth, 2.22 becomes

$$Z(t) = \left(\frac{1}{H}\right) \frac{\int e^{\omega t} T dt}{e^{\omega t}} + k \; . \tag{2.23}$$

The amplitude of near-inertial currents is proportional to $1/H$, an important factor in interpreting the results from this model.

Table 2.1: Wind energy input into internal wave band motions across all model scenarios from 3 to 10 February 2009. * Observed energy input computed from SADCP and observed winds.

Wind time series	Peak wind stress (Pa)	Wind Energy input Π (kJ)	
Ship wind	1.95	3.51*	–
–	–	Slab model Π (kJ)	PWP model Π (kJ)
Ship wind	1.95	1.69	2.84
Decimated ship wind	0.95	0.35 (0.2,0.7) 95% CL	1.18 (0.64,2.23) 95% CL
NCEP	1.40	0.34 (0.1,1.3) 95% CL	1.11 (0.33,4.24) 95% CL
CCMP	2.53	2.82 (0.7,13.2) 95% CL	4.25 (1.06,19.89) 95% CL

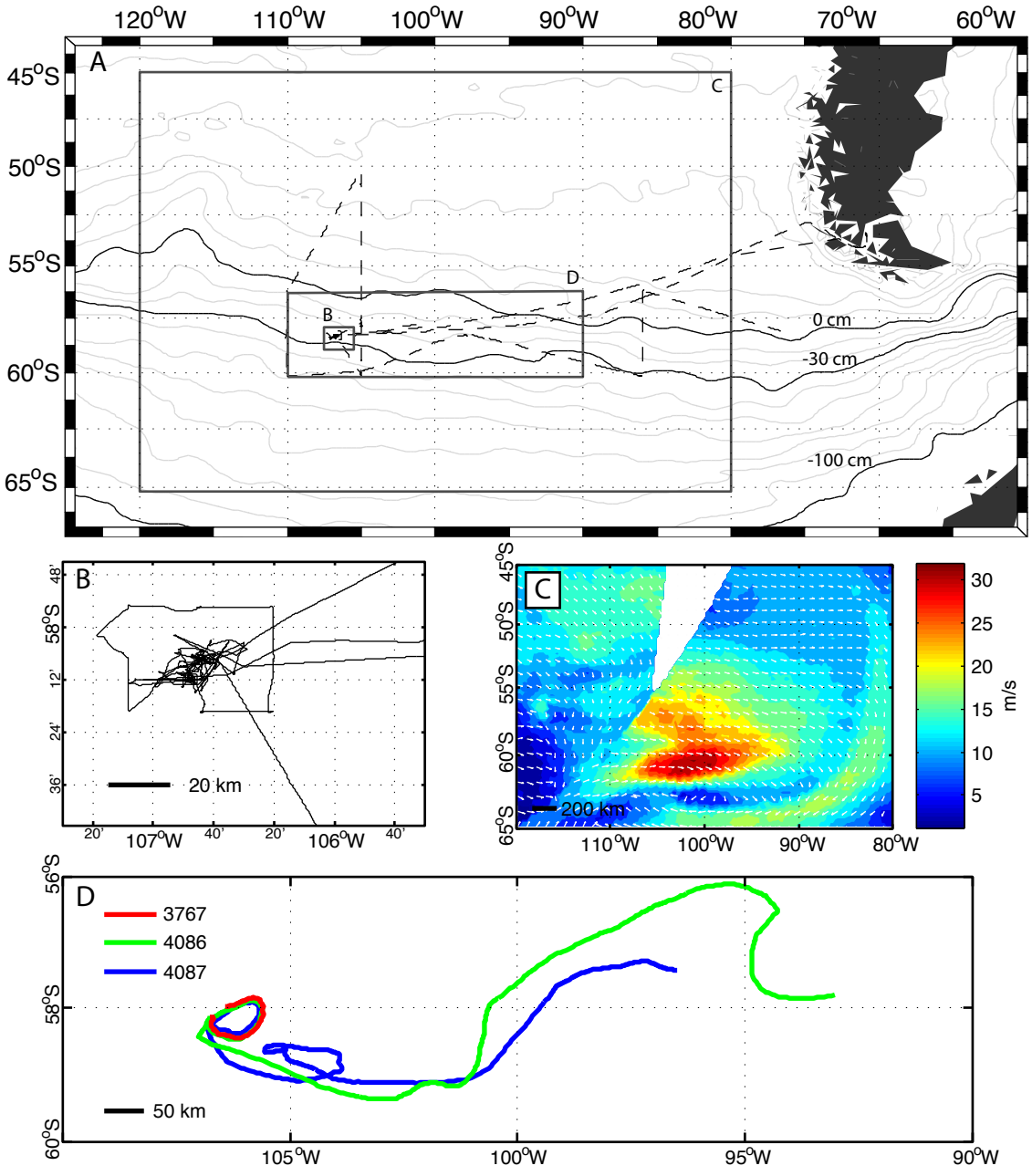
120°W
110°W
100°W
90°W
80°W
70°W
60°W
45°S
50°S
55°S
60°S
65°S
A
B
C
D
0 cm
-30 cm
-100 cm
20 km
107°W
106°W
58°S
48'
12'
24'
36'
20'
40'
200 km
110°W
100°W
90°W
80°W
m/s
30
25
20
15
10
5
3767
4086
4087
50 km
105°W
95°W
90°W
56°S

Figure 2.1: Study region in the Southern Ocean west of Drake Passage. A) Cruise track (dashed) and contours of AVISO absolute dynamic topography averaged from 2000 to 2013. Solid contours approximately correspond to the Subantarctic Front, the Polar Front, and the Southern Antarctic Circumpolar Current Front at 0,-30, and -100 cm respectively. B) Close-up of the DIMES tracer release location, with ship track from 2 to 19 February 2009. Shipboard data in this region are treated as a stationary time series in Fig. 2.5. C) Gridded wind speed and direction from QuikSCAT descending pass on 7 February 2009, illustrating storm size and shape. D) Trajectories from three EM-APEX profiling floats (colored by serial number) deployed near 108^o W and 58^o S.

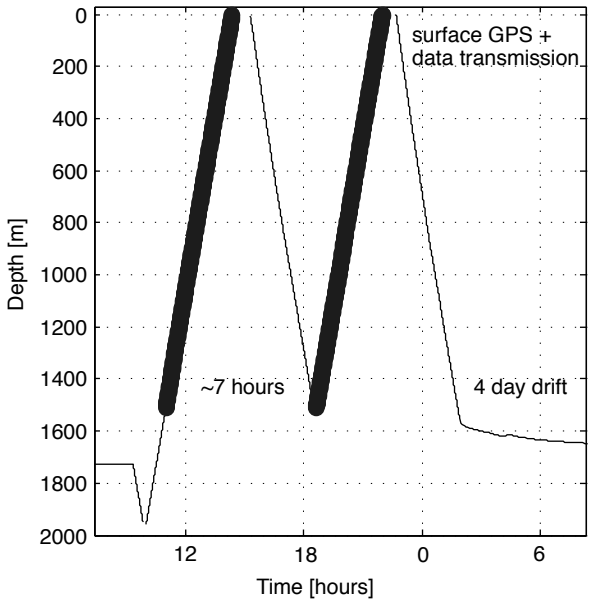

Figure 2.2: Diagram of EM-APEX float path through one burst cycle. The burst begins with the float descending to 2000 m, then surfaces, descends to 1500 m, and surfaces again. The two ascending profiles are separated by approximately one half the inertial period. The drift time between bursts is adjustable, a four-day drift is typical in these data.

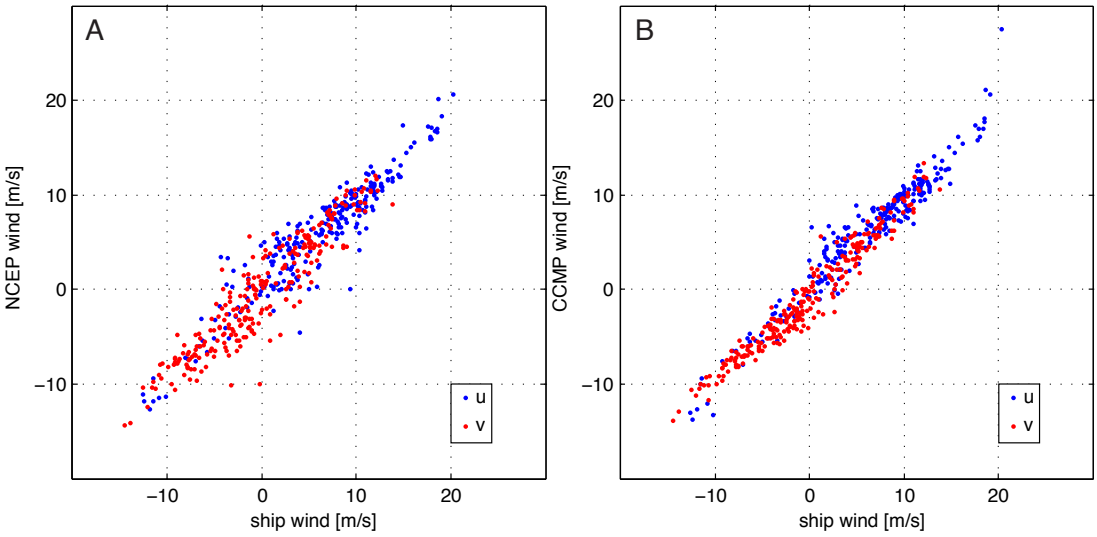

Figure 2.3: Comparison of global gridded wind products to measurements by the ship's sensors. A) 10 m wind from the National Center for Environmental Prediction (NCEP, interpolated onto the cruise track) plotted against measured wind speed. The eastern component of the wind is shown in blue and the northern component is shown in red. B) Same as in A, but comparing Cross Calibrated Multiplatform wind (CCMP) to the measured wind.

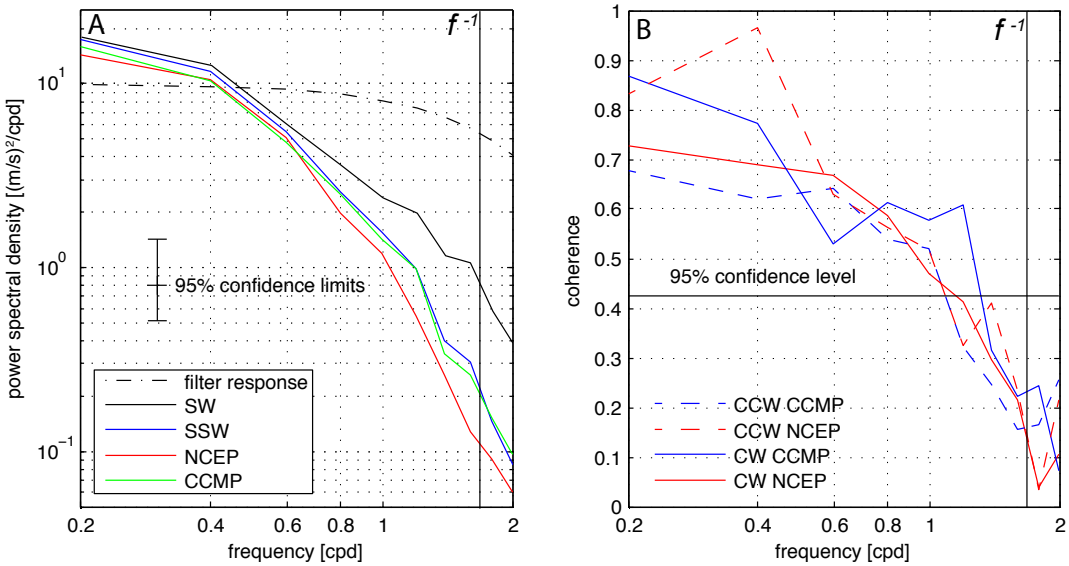

Figure 2.4: Spectral analysis of wind records. A) Power spectrum of wind speed from gridded and measured winds. The local inertial frequency is shown by the solid vertical line. Spectrum from the measured winds smoothed using a six hour rectangular filter match well with the spectra from gridded winds. The response of the smoothing filter is shown by the dashed black line. B) The coherence between gridded and smoothed, observed winds.

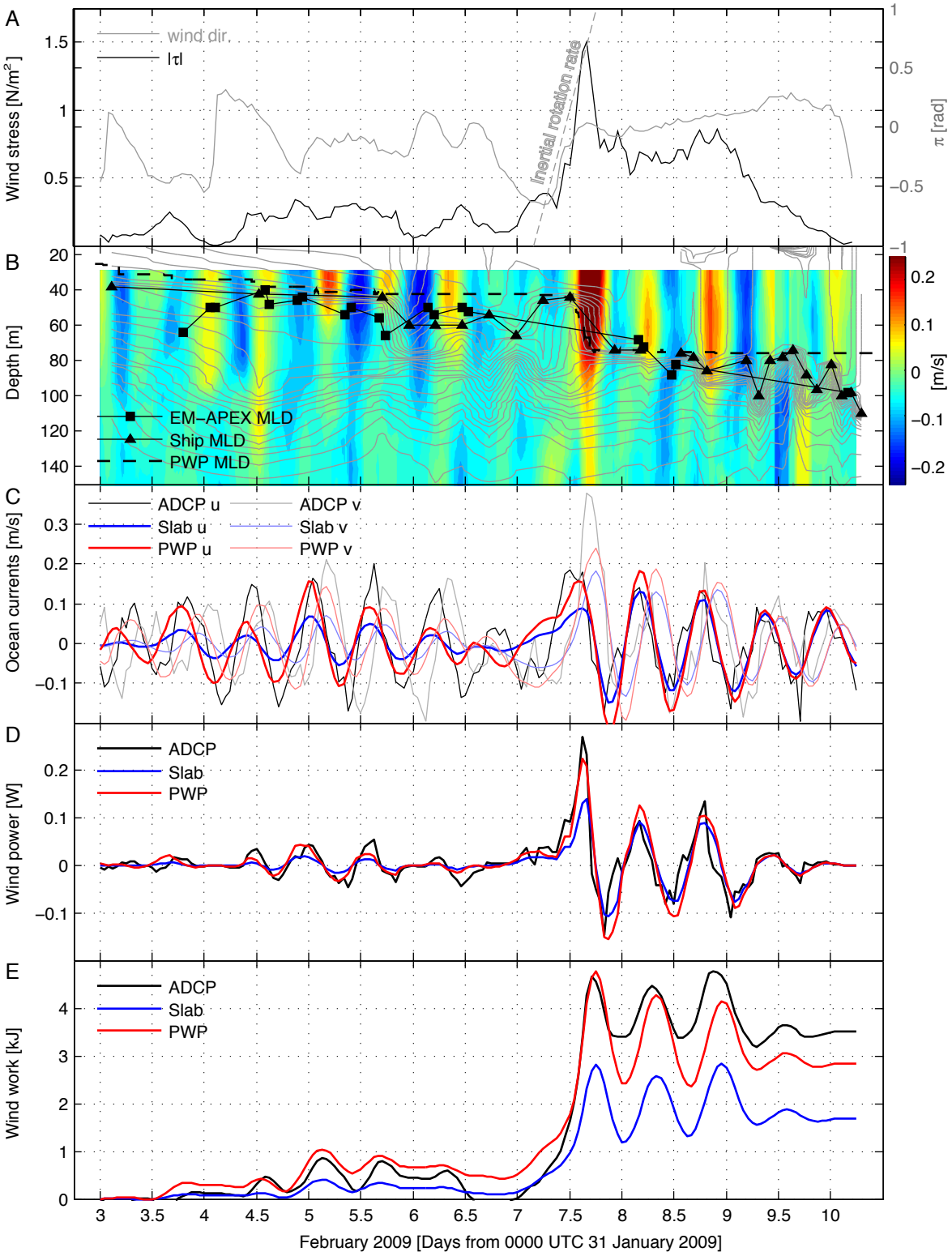
A
Wind stress [N/m^2]
wind dir.
|τ|
inertial rotation rate
π [rad]
B
Depth [m]
EM–APEX MLD
Ship MLD
PWP MLD
[m/s]
C
Ocean currents [m/s]
ADCP u
ADCP v
Slab u
Slab v
PWP u
PWP v
D
Wind power [W]
ADCP
Slab
PWP
E
Wind work [kJ]
ADCP
Slab
PWP
February 2009 [Days from 0000 UTC 31 January 2009]

Figure 2.5: Observed and modeled upper-ocean wind and current time series during the storm period. A) Wind stress determined from shipboard wind measurements is shown by the solid black line. The gray line shows wind direction with 0 radians = East. Dashed line shows the angular rate of change at the inertial frequency (58^o S). B) Shipboard ADCP currents (east component) shown in color. Background density field from ship CTD shown in gray contours (0.01 kg m^{-3} σ_0 isolines). Three time series of mixed-layer depth diagnosed from EM-APEX, ship CTD, and PWP model respectively are shown by black lines. C) Thick lines indicate eastward currents (u) and thinner lines indicate northward currents (v). The band-passed ADCP measurements, slab model currents, and PWP model currents are shown in black, blue, and red respectively. D) Energy flux into near-inertial motions ($\vec{\tau}\cdot\vec{U}$) between wind stress and surface currents. E) Wind-work ($\int \vec{\tau}\cdot\vec{U}dt$) from observations, slab model, and PWP model (black, blue, and red lines respectively).

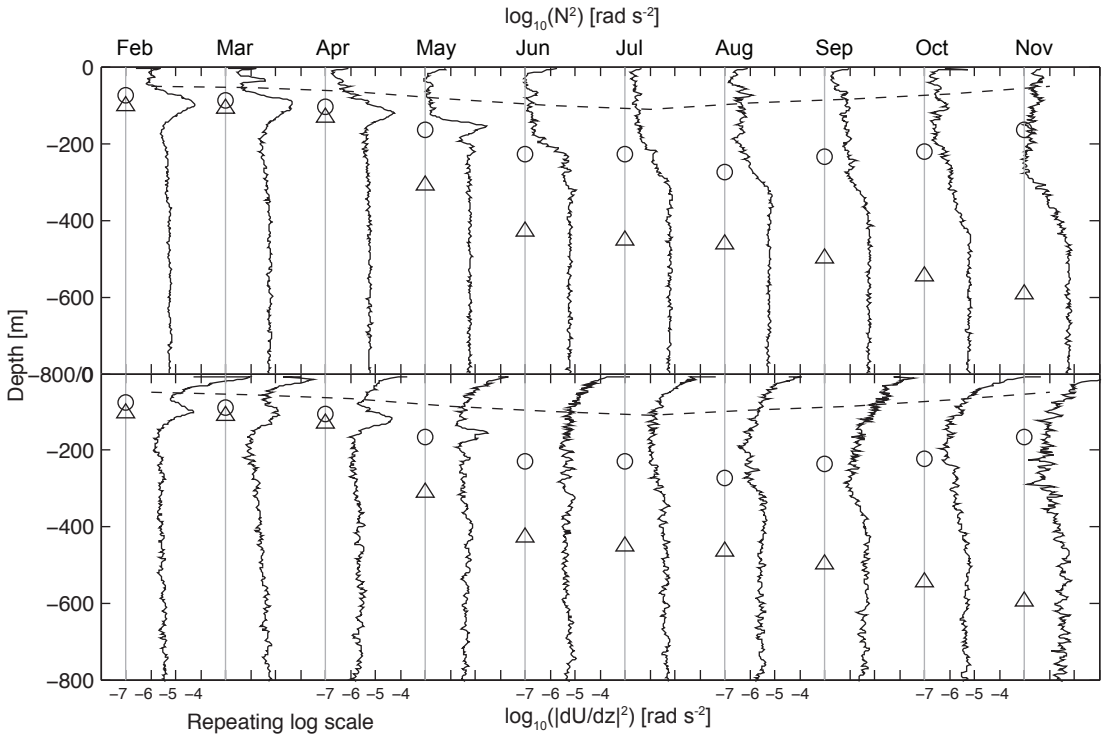

Figure 2.6: Monthly averaged buoyancy frequency squared (upper panel) and shear squared ($|d\vec{U}/dz|^2$) (lower panel) plotted on a repeating logarithmic scale from 10^{-7} to 10^{-4}. Monthly average mixed-layer depth using 0.05 and 0.1 kg m^{-3} criteria shown as open circles and triangles respectively. The mixed-layer time series used with the float following slab model is shown by the dashed line.

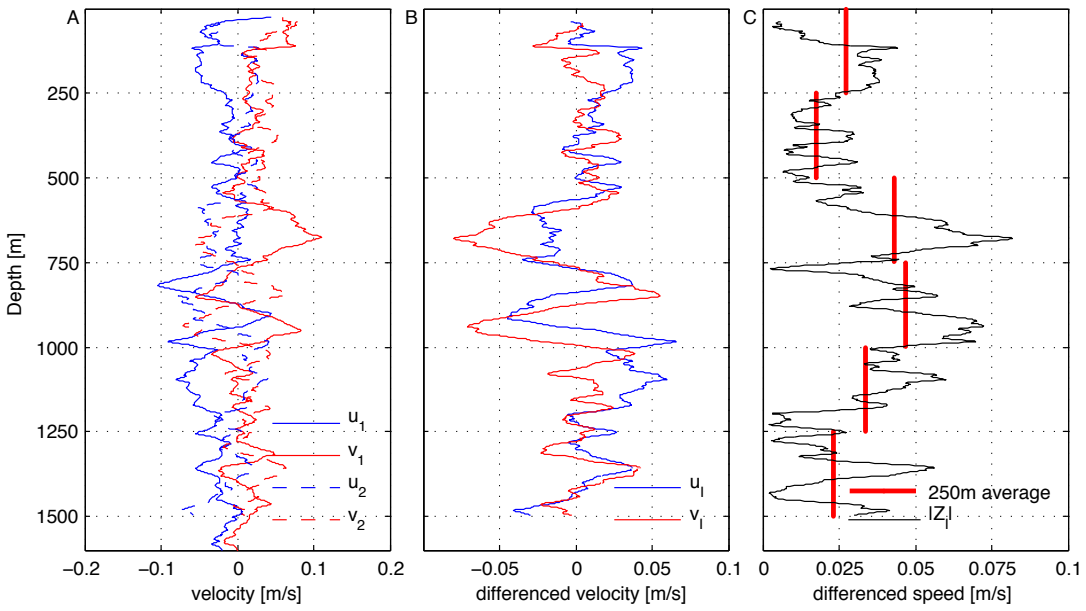

Figure 2.7: A) Ascending profiles of horizontal velocity. Eastward currents (u) are shown in blue, northward currents (v) are shown in red. B) Eastward and northward inertial-band currents after differencing. C) Inertial-band current speed (black) and 250 m average speed (red).

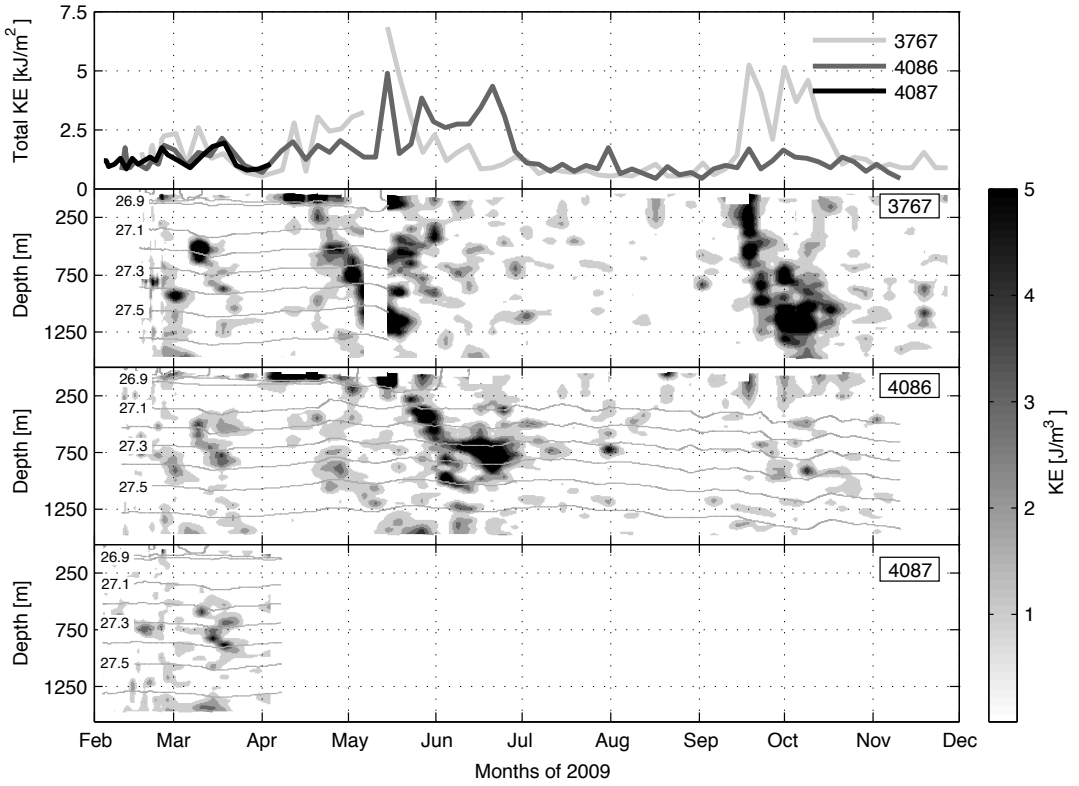

Figure 2.8: Kinetic energy of inertial-band motions observed by EM-APEX. Upper panel: Column integrated (0 to 1500 m) kinetic energy for each float. Lower panels: Kinetic energy from half-inertially differenced velocity profiles from February to November 2009 from each EM-APEX float. Grey contours show potential density anomaly as seen by each float at 0.1 kg m^{-3} spacing.

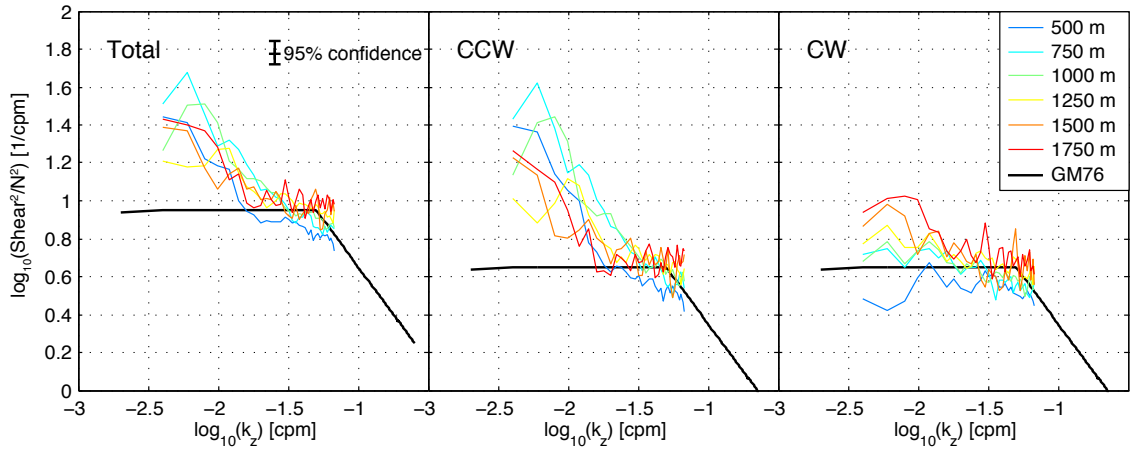

Figure 2.9: Left panel: Vertically binned (500 m bins) power spectra of vertical shear normalized by buoyancy frequency (bin average N^2). The Garret-Munk (GM76) reference shear spectrum at twice the base energy level is shown by the solid black line. The color scale (the same across all panels) denotes increasing depth. Center panel: Counter-clockwise (positive k_z) rotary power spectrum of vertical shear. Right panel: Clockwise (negative k_z) rotary power spectrum of vertical shear.

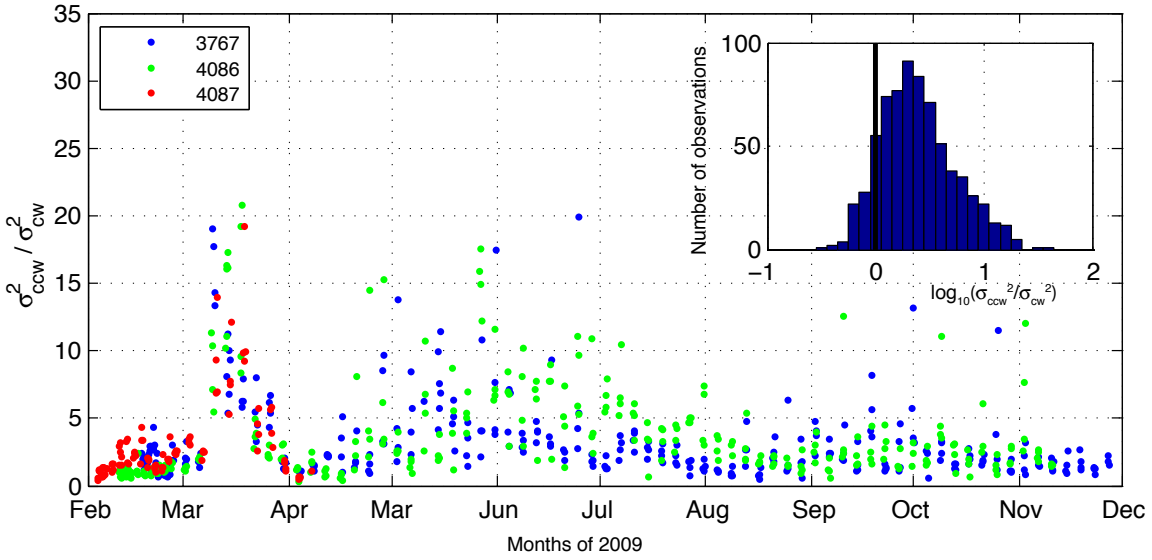

Figure 2.10: Ratio of counter-clockwise to clockwise variance from integrated rotary power spectra. Values above one indicate the majority of the variance is counter-clockwise (indicating downward propagating waves). Inset panel: Histogram of the $\log_{10}$ of the the ratio, the solid black line separates predominantly counter-clockwise variance from predominantly clockwise variance.

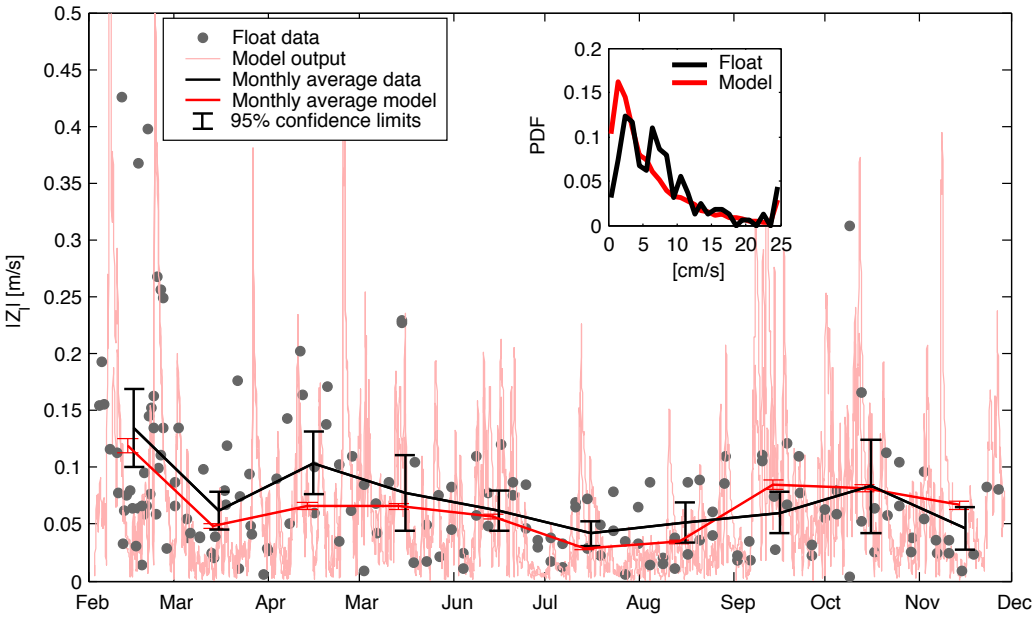

Figure 2.11: Results from the slab model in a float-following reference frame. The current speed from the float following model is shown in light red (results from three model runs are superimposed) and observed mixed-layer currents are shown by gray circles. Colored red and black lines show the monthly average mixed-layer current speed from the model and observations respectively. 95% confidence limits are indicated by vertical error bars. Inset: The empirical probability density function of the EM-APEX observations (black) and the model currents (red). A Kolmogorov-Smirnov test applied to these data does not reject the null hypothesis ($\alpha = 0.05$) that the data are drawn from the same continuous distribution.

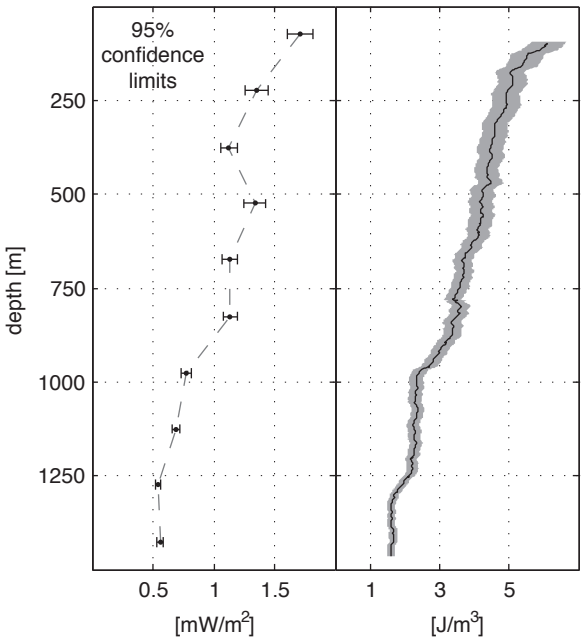

Figure 2.12: Left panel: Vertical energy flux ($E \cdot C_{g_z}$) due to near-inertial waves during March 2009. Error bars show the 95% confidence limits. Right panel: Average near-inertial internal wave energy density over all 2009 data (black line) with 95% confidence limits (gray shading).

Chapter 3

SURFACE BOUNDARY LAYER EVOLUTION AND NEAR-INERTIAL WIND POWER INPUT

3.1 Introduction

[1] Previous studies have used the damped-slab model of inertial-frequency ocean-surface currents (Pollard and Millard, 1970) to estimate the flux of kinetic energy from wind into the ocean surface boundary layer (D'Asaro, 1985; Alford, 2001; Watanabe and Hibiya, 2002; Alford, 2003; Plueddemann and Farrar, 2006). These studies show that this simple model can reproduce observed currents relatively well but is of limited skill in replicating the observed wind power input due to the nonlinear sensitivity of power to small deviations in surface current phase and amplitude. The analytic solutions to this model (Alford, 2003; Kilbourne and Girton, 2015a) show that currents, wind power (W m^{-2}), and wind work (J m^{-2}) scale as the inverse of the mixed-layer thickness H when H is held constant. However, observations from autonomous floats show that near-surface stratification evolves under wind-forcing, as is expected from shear at the mixed-layer base leading to supercritical gradient Richardson numbers $Ri_g = \frac{N^2}{S^2} < 0.25$, where N is the buoyancy frequency and S is the vertical shear ($|d\vec{U}/dz|$). In many cases, the time variation of the mixed-layer depth dramatically influences the resulting wind work due to the H^{-1} dependence of wind power input.

A strong pycnocline acts as a barrier to the vertical extent of turbulence under calm to extreme surface wind conditions. In many cases, the mixed-layer base and upper bound of the seasonal pycnocline are reasonably assumed to be equivalent. However, in the presence of weak near-surface stratification, the assumption of a constant mixed-layer depth is poor due to its rapid evolution under forcing. A better understanding of the temporal evolution and ultimate depth of the actively mixing-layer is needed to improve estimates of the

[1]This chapter was submitted to the Journal of Geophysical Research-Oceans on 9 August 2015.

wind power input driving near-inertial currents. It is critical to improve these estimates as surface inertial oscillations drive the radiation of propagating inertial-internal waves which contribute to the internal upwelling of the global overturning circulation (Munk and Wunsch, 1998).

In the Southern Ocean along the northern boundary of the Antarctic Circumpolar Current (ACC), density profiles do not indicate a clear mixed-layer base or seasonal pycnocline. Upper-ocean stratification is weak, often just above the instrument's limit of measurement. This weakly stratified layer can extend hundreds of meters from the ocean surface (de Boyer Montégut et al., 2004; Lorbacher et al., 2006; Dong et al., 2008; Holte and Talley, 2009). Close inspection of these data often reveals small but measurable stratification at all depths which implies that fully 'mixed' surface layers are somewhat more rare than is typically assumed.

Stratification traps momentum near the surface. The result is that wind-forced surface currents are quite strong at the onset of an event, before momentum is vertically distributed through entrainment, and this enhances wind power input (figure 3.1). This is illustrated through a simple, idealized experiment. Wind power input, defined as

$$\pi = \vec{\tau} \cdot \vec{Z} \ , \tag{3.1}$$

where $\vec{\tau}$ is the complex valued wind-stress $\tau_x + i\tau_y$ and $\vec{Z}$ is the complex valued surface current $u+iv$, is often impulsive. Wind work, defined as the time integral of the wind power

$$P = \int_0^t \pi dt \ , \tag{3.2}$$

is significantly increased in the relative to the unstratified case (the analogue of the damped-slab model). Some of the difference in work can be attributed to the energy required to mix the layer, but the remainder is available for the downward radiation of near-inertial waves.

When the duration of strong wind is much longer than the initial mixing-layer expansion, or when a fully-mixed layer overlies a pycnocline (ie constant H), the damped-slab solution provides a better approximation of wind power input. If the time-scale of strong winds

is approximately the same as that of the mixing-layer expansion, then the time-varying mixed-layer depth must be accounted for to accurately estimate wind power input. When the duration of strong winds is equal to or shorter than the time required to accelerate, entrain, and mix the surface boundary layer, then a constant mixed-layer assumption (ie. the slab model) dramatically misrepresents the energy flux.

The weakly stratified upper-ocean conditions described above are common near the Subantarctic Front (SAF) of the Antarctic Circumpolar Current during austral autumn, winter, and spring. During these seasons, inertial-band winds are strongest. As a result, estimates of wind power input appear weakest when the inverse might be expected. This paper explores the sensitivity of Southern Ocean wind power input estimates to mixed-layer depth parameterizations, proposes a fine-density threshold criterion for estimating the mixing-layer from density profiles, investigates the processes maintaining these uniquely deep surface boundary layers, and proposes improvements to the current wind power estimates in the Southern Ocean.

3.2 Data

3.2.1 Floats

Ocean density profiles from electromagnetic autonomous profiling explorer (EM-APEX) (Sanford et al., 2005) and ARGO program floats across the eastern Pacific, Scotia Sea, and western Atlantic sectors of the Southern Ocean between 2009 and 2013 were used for the development and evaluation of a fine-density threshold mixing-layer criterion. The combined dataset consists of 7039 vertical profiles of temperature, salinity, and pressure from nineteen EM-APEX supplemented with another 2187 profiles of temperature, salinity, and pressure from from eleven Iridium modem equipped, high-resolution ARGO program floats, which sampled approximately the same region and time as the EM-APEX field program (figure 3.2). EM-APEX Temperature and salinity were calibrated by reference to nearby shipboard CTD measurements when available, and were quality controlled to remove spikes and missing segments by visual inspection. The EM-APEX floats measure water velocity by measurements of motional induction (Sanford et al., 2005), but these measurements were

not used in this study.

3.2.2 Gridded products

Float-following wind time series were extracted from the Cross Calibrated Multiplatform (CCMP) 0.25° six-hourly gridded winds product (Atlas et al., 2011). CCMP winds are available through 2011, limiting wind-based comparisons to February 2009 through December 2011. Gridded, six-hourly reanalysis heat-fluxes from the National Center for Environmental Prediction (NCEP) were used as buoyancy forcing (Kalnay et al., 1996). Global mixed-layer climatologies from the National Oceanographic Data Center (NODC)(Monterey and Levitus, 1997), the French Research Institute for Exploitation of the Sea (IFREMER) (de Boyer Montégut et al., 2004), and Pacific Marine Environmental Laboratory (PMEL) (Schmidtko et al., 2013) were compared with mixed-layer observations to evaluate the performance of these climatologies in capturing the mixing-layer thickness.

3.3 Identification of the mixing-layer

3.3.1 Unique conditions in the Southern Ocean

Surface mixed-layers in the Southern Ocean often appear to be abnormally deep. This is reflected in several global climatologies of mixed-layer depth (de Boyer Montégut et al., 2004; Monterey and Levitus, 1997; Schmidtko et al., 2013), where the Southern Ocean is shown as having a weak seasonal cycle with deep surface mixed-layers throughout the year. Mixed-layers identified from the same methods applied to EM-APEX temperature and salinity profiles in the region generally confirm these climatological values. However, these same data show considerable temperature and salinity variance within the identified layers, indicating vertical homogenization of tracers was either not occurring or had not occurred. Published mixed-layer thickness climatologies are not incorrect, as the float data confirm the values. It is the criteria used to identify these mixed-layers that are inappropriate for determining the actively mixing-layer, and it is this which is critical in modeling the inertial-band wind work.

3.3.2 Existing mixed-layer criteria

Mixed-layer criteria currently in use largely fall into either density/temperature threshold or gradient categories. The notable exception is the mixed-layer algorithm developed to address the deep mixed-layers discussed here (Holte and Talley, 2009); this method is addressed in section 3.6.1, and typical density threshold values are 0.01, 0.05, and 0.125 kg m^{-3} used by Thomson and Fine (2003); de Boyer Montégut et al. (2004); Monterey and Levitus (1997) respectively. The application of threshold criteria typically require preconditioning of the density profile (i.e. as smoothing and/or sorting the data), a comparison of these different criteria (along with two finer thresholds discussed below) shows that clear seasonal cycles can be seen in all, but that the depths selected (and thereby, the layer of water implied to be in contact with the atmosphere) vary by a huge range – often several hundred meters (figure 3.3).

Mixed-layer thicknesses determined from density (also temperature) threshold criteria appear to be more statistically stable than those from gradients (Dong et al., 2008). Under weakly stable stratification conditions density gradient based criteria are not useful. Coarse gradient criteria are often not satisfied at any depth while fine gradient criteria are prone to false positive results.

High-resolution EM-APEX and Iridium equipped ARGO float data show that the water column is often weakly but stably stratified during the austral winter. In these conditions the application of the density threshold criteria simply identify a point along the stratified continuum as opposed to a mixing-layer. When weak-stratification is present, buoyant forces must be overcome to homogenize tracers and this has a non-trivial impact on the the energetics of the near-inertial response (an idealized simulation using the Price-Weller-Pinkel model illustrates this in figure 3.1).

While a fine-density criterion identifies the thickness of the layer in which tracers are fully homogenized, it does not provide sufficient evidence to identify the 'true' depth of active turbulence, as this requires microstructure observations. The first goal of this analysis is to determine an appropriate density-difference criterion which best identifies the thickness of the fully homogenized surface layer.

3.3.3 Fine density threshold criterion

It is for these weakly stable conditions that a new criterion is proposed for identification of the actively mixing-layer using profiling float data. These floats use the Sea-Bird SBE41 (later SBE41CP) sensor to measure in-situ temperature, conductivity, and pressure. Published error values (Sea-Bird electronics) for this instrument show that in typical temperatures and salinities in the Antarctic Circumpolar Current, this instrument has an approximate noise floor in density of 6×10^{-4} kg m^{-3}. Analysis of the in-situ temperature and salinity for spectral noise floors confirm the manufacturer's error values. These uncertainties were conservatively rounded up to 1×10^{-3} kg m^{-3} (one gram per cubic meter of seawater) for this analysis.

The use of such a fine-density criterion requires careful preparation of the density profile. The following method was used: *in-situ* temperature and salinity were used to compute the surface referenced potential density anomaly σ_0. The potential density profile was interpolated onto a uniform 2 m grid and rounded to the nearest 1×10^{-3} kg m^{-3} to remove variance below the instrument noise floor. The σ_0 profile was sorted to obtain static stability. As two identical *in-situ* values of σ_0 may have been rounded up or down as a result of instrument noise, two times the rounding value is the finest resolvable density difference in the processed profiles. Thus, the finest practical density-threshold criterion which can be generally applied to a density profile from float data from the SBE41 type sensor is $\Delta\rho = 0.002$ kg m^{-3} (figure 3.3). Although this value is the most rigorous in identifying the fully-homogenized surface layer, the differences among thresholds up to 0.01 kg m^{-3} are relatively small. We have selected an intermediate criterion of 0.005 kg m^{-3} on the basis of dynamical arguments presented in section 3.4, below.

There are two primary motivations driving the use of an extremely fine determination of the mixing-layer. The first is the work of Brainerd and Gregg (1995), where direct measurements of turbulent dissipation show sharp decline in dissipation rate below density increments of $\Delta\rho \approx 0.005$ kg m^{-3}. These direct observations of dissipation rate provide strong evidence that the active-mixing layer is often delineated from an apparently 'mixed-layer' by fine increments in vertical stratification. A second motivation comes from an

apparent inconsistency in the observations. For the purposes of modeling near-inertial wind work, the mixed-layer is assumed to actively homogenize all vertical tracers, including temperature, salinity, and momentum. However, the data presented here frequently exhibit non-trivial variations in temperature and salinity (figure 3.4) but exhibit very little stratification. These profiles are challenging to interpret because, while they require very little energy to drive vertical overturning, tracer profiles clearly indicate that active mixing is limited to a thinner layer than stratification alone would suggest. The adoption of the fine density criterion proposed here mostly excludes temperature and salinity variance from the mixing-layer.

Increasingly fine definitions of the mixing-layer thickness H also improve estimates of how often interior isopycnal surfaces come into direct contact with the atmosphere. For example, these data show that ventilation below 400 m is likely much more rare than coarse criteria would indicate (figure 3.5).

3.4 Mixing-layer processes

In order to justify the use of a fine-density threshold criterion (and to select the most appropriate value) it is important to explore the physical processes driving mixing in the surface boundary layer. Weakly stratified surface layers are often hundreds of meters deep. The time needed for momentum to stir to these depths through average turbulent vertical motions (shown by D'Asaro et al. (2014) to scale as $\langle w \rangle = u_*$) is, on average, in excess of one-half the local inertial period (figure 3.6). Because mixed-layer formation often occurs quickly, another explanation for the vertical expansion of the turbulent mixing-layer is required. Three plausible mechanisms for the creation of larger than average vertical velocities are explored here: rapid deepening through shear instability at the base of the mixed-layer driven by impulsive winds, rapid vertical injection of momentum from the surface through downwelling jets produced by Langmuir cells (Langmuir et al., 1938; Weller and Price, 1988), and surface buoyancy-driven convective plumes. These three mechanisms were explored through use of the Price-Weller-Pinkel (PWP) mixed-layer model (Price et al., 1986), a Langmuir cell parameterization following Li and Garrett (1997), and simulated buoyant convection forced by reanalysis heat-fluxes, respectively.

3.4.1 Shear instability

One mechanism by which tracers are homogenized throughout the surface layer is through entrainment of successively deeper layers due to shear instability brought on by supercritical vertical shears at the mixed-layer base. In this approach, changes at the surface must propagate downward through acceleration of successive stratified layers. This process continues until the gradient Richardson number at the base of the mixed-layer becomes subcritical, suppressing shear driven turbulence and preventing further deepening of the layer. The vertical mixing scheme used in PWP is based on critical gradient and bulk Richardson numbers (0.25 and 0.65 respectively), making this model useful for exploring how vertical shear forms mixing-layers in response to surface wind-stress.

Simulation of mixing-layer

Figure 3.7 illustrates a set of simulations exploring the parameter dependence of shear-driven mixed-layer deepening. Five synthetic wind time-series were created to force the PWP model across a range of realistic conditions. Each wind record was defined as a vector rotating counterclockwise at the inertial frequency (at 58° S) for four days. This rotary wind time series was windowed with a Gaussian filter of 0.59 day width (at half maximum) centered on day two to approximate the shape and duration of a passing ocean storm. The peak wind-stress was varied evenly from 0.5 to 2.5 Pa across the five scenarios (figure 3.7).

Temperature was constant and the model was run without surface buoyancy-fluxes, resulting in constant temperature throughout the simulation. Initial stratification conditions were set with five linearly increasing salinity profiles such that each simulation began with constant stratification (figure 3.7). Iterating over this set of five initial conditions and wind-stress scenarios yielded twenty five simulations of mixing-layer depth and near-inertial wind work. Results from these simulations show that mixing-layer depth increases with wind-stress; deeper mixed-layers have a weaker response due to dilution of momentum over a greater depth range. The time-integrated wind work increases with both wind-stress and initial stratification.

Comparison to float observations

The above suite of PWP simulations explored the response of the model under idealized conditions. In a set of more realistic tests, the PWP model was initialized using observed temperature and salinity profiles and forced with an idealized inertially-rotating wind representation of the 'observed' (via CCMP reanalysis) wind field. Only profiles with a corresponding wind-stress $\tau > 0.1$ (a subset of 2537 profiles) were used.

In each case the final PWP determined mixing-layer was compared to the corresponding density difference determined mixing/mixed-layer depths from the initial profile. The density difference that minimized the rms difference between the modeled mixing-layers and the observations is 0.005 kg m^{-3} (figure 3.8).

We use simple scaling arguments to suggest a relationship between wind work P, $\vec{\tau}$, and H that can be tested with these PWP simulations. The damped-slab model equation,

$$\frac{d\vec{Z}}{dt} + (r + if)\vec{Z} = \frac{\vec{\tau}}{\rho H} \ , \tag{3.3}$$

where f is the Coriolis frequency, r is a linear drag parameterizing inertial-internal wave radiation, and $\vec{Z}$ is the complex mixed-layer current $u + iv$ has a Fourier solution (D'Asaro, 1985; Alford, 2003), when mixed-layer thickness H and density ρ are held constant, of

$$\vec{Z}(\sigma) = \frac{\vec{\tau}(\sigma)}{\rho H} \frac{1}{r + i(\sigma + f)} \ . \tag{3.4}$$

Ignoring phase and substituting the magnitude of $\vec{Z}(\sigma)$ into equation(3.2) yields

$$P \approx \int_0^t \tau \cdot \frac{|\vec{\tau}|}{\rho H f} dt \ . \tag{3.5}$$

Approximating the time integral in equation(3.5) using an integration timescale of r^{-1} results in the approximate expression for wind work

$$P \approx \alpha \frac{|\vec{\tau}|^2}{\rho H f r} \ , \tag{3.6}$$

where α is a constant representing a number of integration time-scales. An minimization of root-mean-square error between PWP simulated wind work to that determined using

equation 3.6 results in $\alpha = 0.757$. The excellent agreement (figure 3.9) between the observed mixing-layer thickness H and the simulated mixed-layer depth and also between the parameterized wind work and the simulated wind work (figure 3.8) indicates that wind work can be parameterized with some skill using the inertial band wind-stress magnitude (from CCMP or a similar gridded product) and a mixing-layer depth (from any sufficiently well-resolved density profile).

3.4.2 Langmuir circulation

Observations from neutrally-ballasted, Lagrangian, mixed-layer floats show that average vertical velocity is related to wind-stress by $\langle w \rangle = \sqrt{\frac{\tau}{\rho}}$ (D'Asaro, 2001; D'Asaro et al., 2014). These velocities, which average 1 cm s^{-1}, cannot expand the mixing-layer to the observed depths within the short time periods observed in both the float data and the simulations. A mechanism for a more rapid delivery of momentum to the mixed-layer base comes in the form of elongated counter-rotating vortices generated in the direction of surface winds known as Langmuir cells (Langmuir et al., 1938). The convergent zones between cells generate relatively strong vertical currents capable of delivering momentum to the observed depths and observed time scales of mixed-layer deepening. A long and detailed literature on the topic of Langmuir cells exists (Thorpe, 2004), from which the parameterizations of the vertical scale of these cells

$$\tilde{h} = \frac{cu^*}{\bar{N}} \ , \tag{3.7}$$

and the convergent downwelling velocity

$$w_{dn} = 0.008 \, U_{10} \tag{3.8}$$

have been used (Li and Garrett, 1993, 1997). Here u^* is the friction velocity, defined as the square root of the wind stress divided by the water density $\sqrt{\frac{\vec{\tau}}{\rho}}$, c is a constant (approximately 10) derived using LES simulation, N is the (upper ocean average) buoyancy frequency of the water column, w_{dn} is the downwelling water velocity, and U_{10} is the 10 m

wind speed. The value 0.008 in equation 3.8 is based on the assumption that La (Langmuir number) = 0.01 (the values of c and La are determined in Li and Garrett (1997)).

Since N is not constant in observations, the Langmuir cell depth was determined from these parameterizations by balancing the downwelling kinetic energy $\frac{\rho_0}{2}\left(w_{dn}^2\right)$ with the near-surface buoyant potential energy $\int_0^H \rho(\acute{z})g d\acute{z}$. In this conceptual model the downwelling jet is resisted by positive buoyant forces, and we solve for H. Here ρ_0 is the reference density (10 m density was used in this study), $\rho(z)$ is the observed potential density, and $g = 9.81$ m s^{-2} is the acceleration of gravity.

These parameterizations were applied to each float density profile. Wind-stress was derived from CCMP wind using a speed dependent drag coefficient (Large and Pond, 1981) (appropriate for the wind speeds below 25 m s^{-1} (Powell et al., 2003)). To compare with $\tilde{h}$ expression (equation 3.7), $\bar{N}$ was defined as the the mean of all observed N between the surface and the depth of the maximum N. In practice this depth was usually the mixed-layer base, but in many profiles investigated here the peak buoyancy frequency occurs at mid-depth near 1000 m.

The $\tilde{h}$ parameterization does not appear to be well correlated with the observed mixing-layers. The dependence of this parameterization on the determination of $\bar{N}$ from the density profile limits this method's utility as the results are very sensitive to the method used to determine $\bar{N}$. The parameterization for downwelling convergent velocity performs very well. The depth at which downwelling kinetic energy and the depth integrated buoyant forces balance agrees with the depth of the 0.005 kg m^{-3} density difference (figure 3.10). These results indicate that convergent downwelling jets caused by Langmuir cell convergence are a plausible mechanism for rapid deepening of mixing-layers.

3.4.3 Convective plumes

Surface buoyancy forcing drives mixing-layer turbulence through formation of convective plumes (Marshall and Schott, 1999). Six-hourly NCEP reanalysis heat-fluxes were used to simulate buoyant convection. The flux data were interpolated onto float trajectories. These fluxes were integrated over six hours centered on the time of the observations to determine

the net change in heat content in the surface boundary layer. Heat content changes were applied to the upper meter of the profile and, if the resulting density profile was statically unstable, then the profile was vertically mixed using the static stability subroutine from the PWP model. The resulting depth convective penetration was interpreted as the depth to which buoyancy drives active mixing.

These results show that heat fluxes are rarely sufficient to account for the observed mixed-layers. In the majority of cases, convective plumes do not penetrate the full mixed-layer (figure 3.11). This indicates that density changes due to surface heat fluxes are too small to be solely responsible for the creation of the observed deep mixed-layers. It is clear that the cumulative effect of surface buoyancy flux drives the seasonal cycle in pycnocline depth, but these simulations suggest that surface heat loss does not maintain turbulence in the mixing-layer.

The scatter of convective depth around a linear fit to the data is approximately 100 m, which makes a detailed comparison of these two mixing-layer estimates impossible in the upper 100 m of the ocean. These results support the previous hypothesis that mixing-layers are maintained by wind energy, but may have alternate explanations. For example, the NCEP/NCAR heat fluxes used to drive convection may not accurately represent the *in-situ* conditions observed by the floats.

3.5 Impact on near-inertial wind power

3.5.1 Relationship between wind power and the mixing-layer

The wind power estimates from previous studies have used climatological mixed-layers in implementation of the Pollard-Millard near-inertial current response, or 'slab', model (equation 3.3). In that model, when the mixed-layer thickness H is assumed constant, the average wind power transferred to the ocean scales with H^{-1}. The previous sections have shown that a fine-density criterion is needed to improve estimates of the mixed-layer thickness H, and that in the Southern Ocean H is maintained by mechanical input from the wind. The discrepancy between mixing-layers determined from varying criteria is largest during the austral winter in the eastern Pacific sector of the ACC.

3.5.2 Comparison of climatological mixed-layers to observed mixing-layers

Accurate estimates of wind power require knowledge of how the mixing-layer evolves under forcing, which is unknown in general. The next best improvement to global wind power input estimates are a monthly climatology of correction factors, which we generate using the NODC mixed-layer depth climatology as a reference. The observed mixing-layers were separated into Pacific, Scotia Sea, and Atlantic regions. A comparison of the average monthly observed mixing-layer thickness with the NODC climatology shows that the climatological mixed-layer thicknesses exceed the observations by a factor of 1.5 to 3 over the year (figure 3.12). The deep mixed-layers which motivated this study were seen in only the Pacific region of the ACC, but the relationship of the climatology to the observations holds across each of the basins. During the austral summer, the coarse density threshold (0.125 kg m^{-3}) used to generate the climatology identifies mixed-layer depths comparable to the observations. As the seasons progress, the difference between the climatology and the observations increases, reaching a maximum in November. The four month lag between the austral solstice and the greatest disagreement is due to the coarse criterion failing to identify the formation of a weak pycnocline at the onset of the austral spring. The formation of the seasonal mixed-layer base in the austral spring is marked by a transitional time when shallow mixed-layers repeatedly form and are mixed away into the remnant layer beneath. During this time the climatology retains the deep mixed-layer from the winter, leading to extreme overestimates of the actively mixing depth.

In both the observations and climatological products, the deepest mixed/mixing-layers occur in the eastern Pacific sector. In this region the deep winter-mixed layers leave weakly stratified remnant layers below the actively mixing-layer. Close inspection of these remnant layers shows weak-stable stratification which is likely attributable to horizontal processes (Hosegood et al., 2008) which were not resolved by the data presented here. Weakly-stable stratification is important to near-inertial band energy in two important ways. In general, the buoyancy frequency associated with these remnant layers is greater than, but near, f; effectively limiting the downward-propagating internal wave band to near-inertial motions. The transition from the active mixing-layer into this weakly stratified layer is

often quite subtle, requiring a fine-density criterion to identify its existence. While the mixed-layer depths vary considerably between the Pacific, Scotia Sea, and Atlantic sectors of the Southern Ocean, the ratio between observations and climatology is similar across the study region (figure 3.12).

3.6 Discussion

3.6.1 MIMOC mixed-layer depths

The results shown here indicate that mixed-layer thickness H found using a density-difference criterion of $\Delta\rho = 0.125$ kg m^{-3} overestimate the monthly average H by as much as a factor of four. Recently, an algorithm was developed to specifically address the deep, weakly-stratified density profiles studied here (Holte and Talley, 2009). This algorithm was used to generate the Monthly Isopycnal and Mixed-layer Ocean Climatology (MIMOC) mixed-layer depth climatology (Schmidtko et al., 2013). This algorithm, which the authors provide as MATLAB code, was applied to EM-APEX and ARGO temperature and salinity profiles used in this study. The results show that this algorithm does identify the mixing-layer with better skill than the other criteria investigated here. However, in many cases this algorithm does overestimate the mixing-layer. Two scenarios which seem to present difficulty for the algorithm are: 1) compensating temperature and salinity inversions which have little expression in density and 2) weak but measurably stable stratification. In the latter case, the mixing-layer is often identified at the depth where the density gradient sharply increases; this is frequently far below the depth identified using a fine-density difference. In spite of these occasional discrepancies, the MIMOC mixed-layer climatology, when evaluated in the same manner as the NODC climatology, agrees well with the observed mixing-layer depth (figure 3.13).

3.6.2 $\Delta\rho$ values

In many cases the effective differences between the mixed-layer identification criteria are negligible. This is particularly true when comparing the mixed-layers identified using the 0.005 and 0.01 kg m^{-3} criteria. Visual inspection shows that, in some cases, there is evidence

that 0.01 kg m^{-3} is too coarse. The results presented here make the case that a criterion between the instrument's resolution of 0.002 kg m^{-3} and the previous finest criterion of 0.01 kg m^{-3} is a better identification of the mixing-layer than the criteria in current use. The comparisons with PWP and Langmuir cell parameterizations of mixing-layer thickness H strongly indicate that 0.005 kg m^{-3} is the most appropriate density-difference criterion. The nearly linear relationship (figure 3.10) between the depth where $\Delta\rho = 0.005$ kg m^{-3} and that derived through the wind-based parameterizations holds across density profile observations spanning three years, the breadth of the ACC, and the Atlantic and Pacific sectors of the Southern Ocean. This suggests that this $\Delta\rho$ value has general applicability, however it has not been tested outside of this region and the agreement seen here may be specific to the Antarctic Circumpolar Current.

3.7 Conclusions

By studying the detailed vertical structure of Southern Ocean near-surface stratification in an autonomous profiling float database, we have been able to justify a new fine-density criterion for determining the thickness of the actively-mixing surface boundary layer.

Estimates of near-inertial energy flux using the Pollard-Millard damped-slab near-inertial current model require parameterization of the thickness of the mixing-layer (the layer in contact with the wind), which is fundamentally different from the mixed-layer (the weakly-stratified remnant of a past mixing event). This work suggests the actively mixing-layer can be estimated using a high-resolution density profile and the $\Delta\rho = 0.005$ kg m^{-3} density-difference criterion.

This criterion is justified by the fact that the identified depth agrees well with simulated mixing-layer thickness from vertical shear and Langmuir cell mixing schemes. In addition, in most cases the mixing-layer does not appear to be the result of surface buoyancy forcing. These results suggest that wind forcing is responsible for both the rapid expansion of the mixing-layer and maintenance of mixing-layer turbulence in the Southern Ocean.

As an aside, we demonstrate a simple but effective parameterization of wind work using observations of the mixing-layer thickness H, determined using the $\Delta\rho = 0.005$ kg m^{-3} density-difference, and a scalar value of wind-stress determined from gridded global datasets.

From the seasonal and spatial distribution of mixing layer thickness, it is apparent that previous estimates of near-inertial wind power estimates (Alford, 2003) should be scaled by a factor of 1.5 to 3.5, in the Southern Ocean, to account for overestimated mixed-layer depth used in these calculations.

These results emphasize the importance of quantifying the actively-mixing layer in any high-latitude mode water formation region, not just the Southern Ocean. Although our conclusions about density criteria are supported by previous microstructure observations, there is a need for additional microstructure sampling in the weakly stratified surface layers considered here. Microstructure surveys from research vessels are both difficult and expensive due to distance and typical sea-state in the Southern Ocean. A more effective survey of upper ocean microstructure may require the use of autonomous vehicles.

3.8 Acknowledgments

This research was funded through NSF grants OCE0623177 and OCE1129564. We would like to particularly thank John Dunlap and Avery Snyder for keeping the instruments operating and producing quality data in the face of many challenges. The quality of this manuscript has been improved by the patient listening and thoughtful comments of Eric Kunze, Thomas Sanford, Eric D'Asaro, Leah Johnson, Haley Dosser, Ramsey Harcourt, and Brain Chinn.

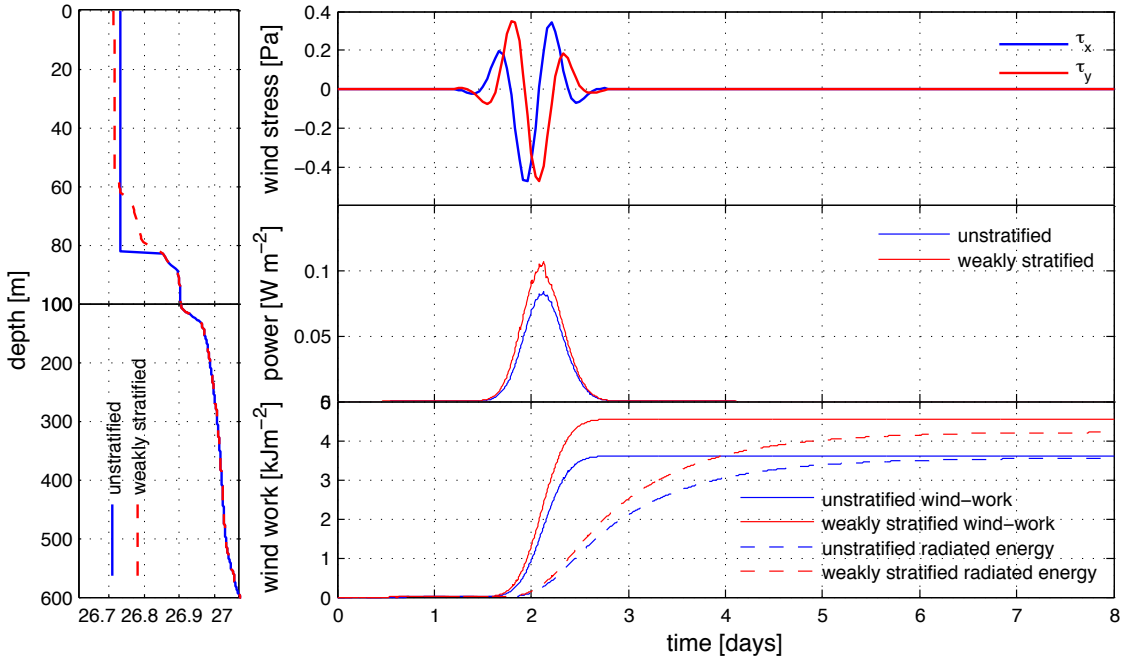

Figure 3.1: Left; Observed vertical profile of potential density (red dashed) and the same profile mixed to the depth of the 0.125 kg m^{-3} density-difference (blue). The mixed profile mimics the dynamics of the damped-slab mixed-layer model. Top right; Wind-stress vector components showing an inertial-frequency wind pulse. Center right) The wind power transferred to near-inertial surface currents. The weakly-stratified profile (red) receives greater power than the mixed profile (blue) due to the initially thinner mixing-layer. Bottom right; The time integrated wind work (solid lines) and energy lost to internal waves (dashed lines, defined as the time integral of the power lost to the linear drag coefficient). The weakly-stratified profile results in an 18% increase in radiated internal wave energy.

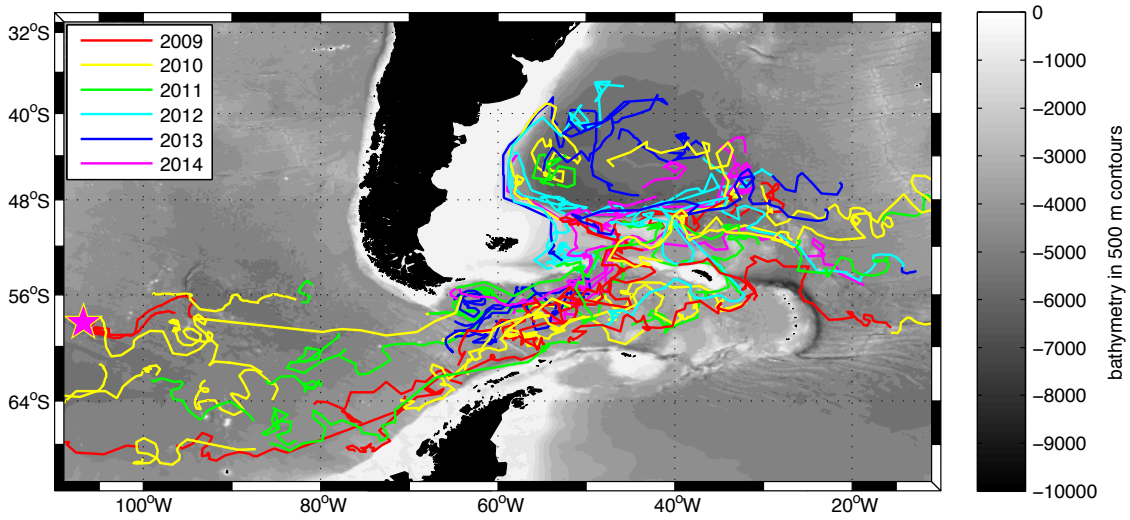

Figure 3.2: Trajectories of each of the floats used in this study. The float tracks are colored by the year in which the observations were made. The shading shows 500 m depth contours and land is shown with solid black shading.

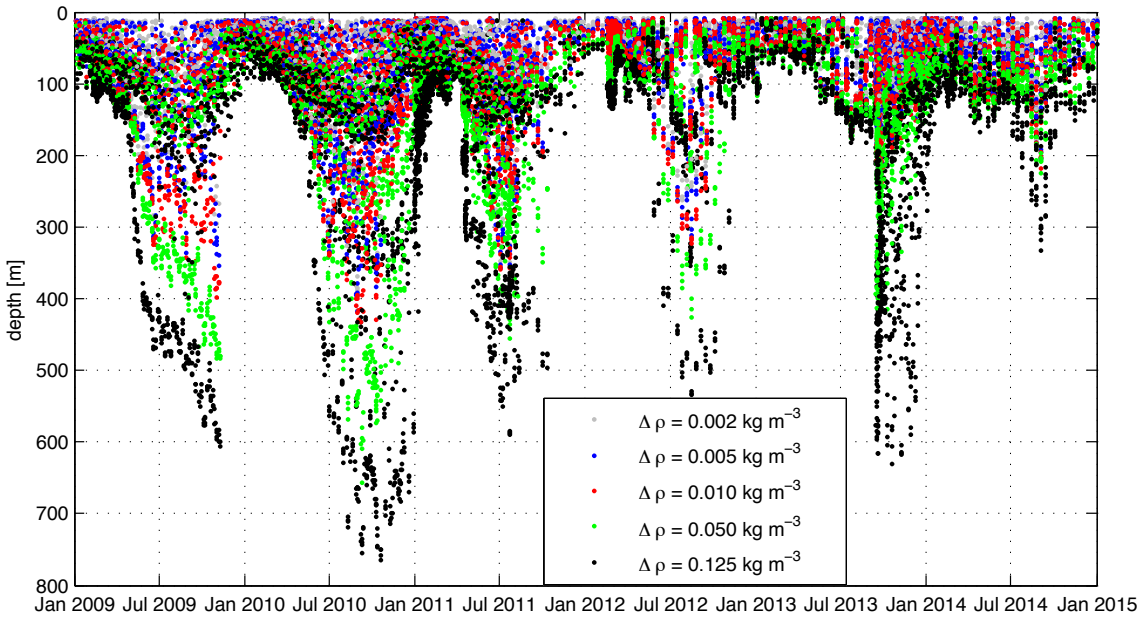

Figure 3.3: Mixing-layer thickness H from all density profiles, as determined from the five density-difference criteria.

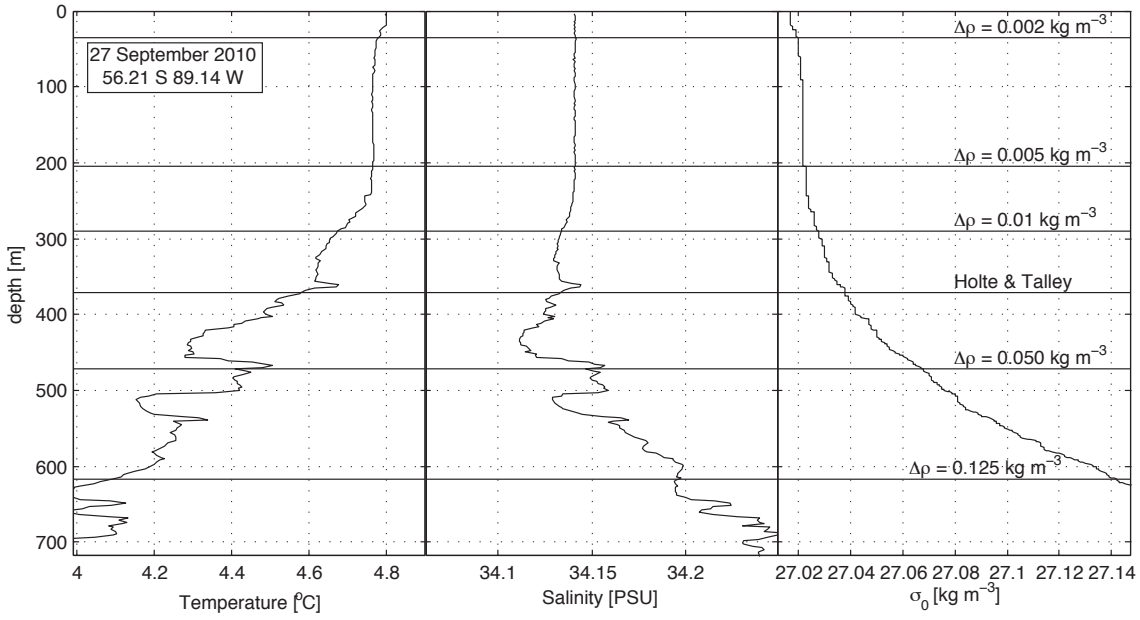

Figure 3.4: Observed in-situ temperature(Left) salinity(Center) and potential density anomaly (Right) during austral spring in the eastern Pacific sector of the Southern Ocean. Horizontal lines show the mixed-layer thickness as identified by five increasing density-difference criteria and by the mixed-layer algorithm developed by Holte and Talley (2009). These data come from EM-APEX # 4815 on the 180th (ascending) profile.

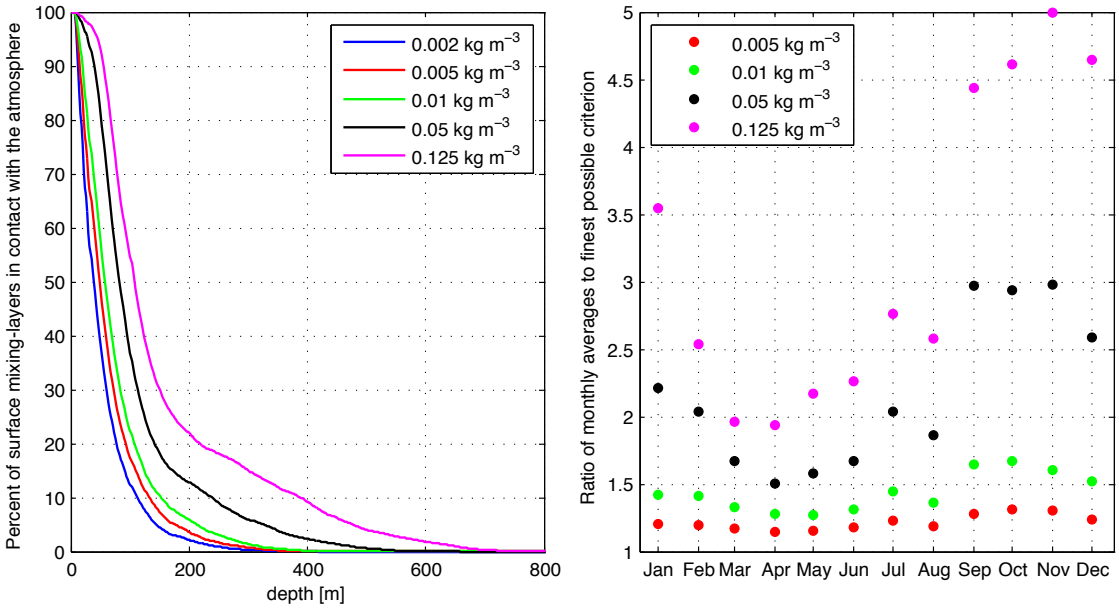

Figure 3.5: Left; The percent of mixed-layer thickness H observations which are inferred to be in contact with the atmosphere according to five density-difference criteria. The three finest criteria, which have similar distributions, indicate that direct contact with the atmosphere is rare below 400 m. Right; Ratio of monthly average mixing-layer thickness to the absolute finest (0.002 kg m^{-3}) criterion. The large ratios seen September through January are due to the two most-coarse criteria failing to capture stratification associated with the austral spring.

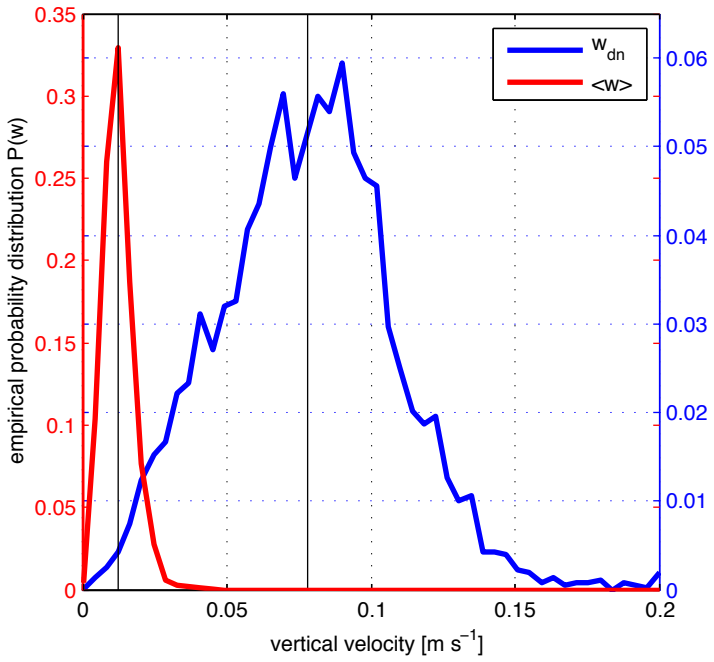

Figure 3.6: Empirical probability distribution functions of vertical velocity associated with downwelling jets as determined from the Langmuir cell parameterization $w_{dn} = 0.008U_{10}$ (where U_{10} is the wind speed at 10 m above the ocean surface) (Li and Garrett, 1997) (blue) and the root-mean-square of observed vertical velocities which are characterized by $\langle w \rangle = u_*$ (D'Asaro et al., 2014) (red). The vertical black lines show the mean of each distribution, the mean speed of downwelling jets w_{dn} is 6.2 times the long term mean of $\langle w \rangle$.

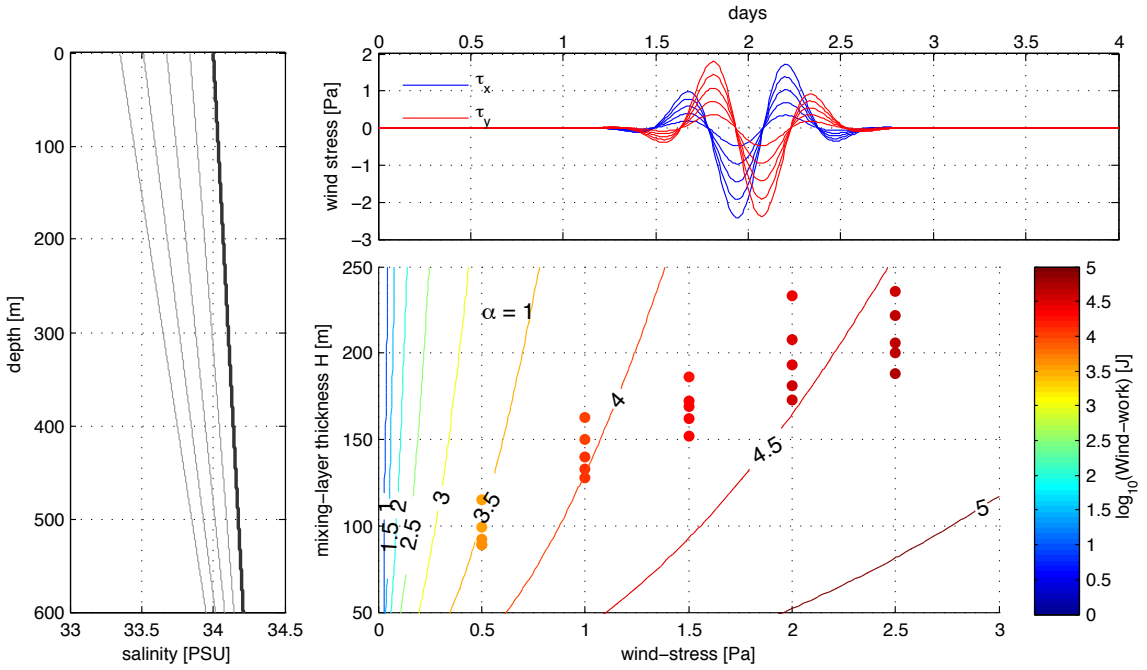

Figure 3.7: Left; Salinity profiles used to initialize the idealized PWP model simulations. Top right; Inertial band wind-stress pulses varying in peak magnitude from 0.5 to 2.5 Pa. Bottom right; Colored dots show the log_{10} of the wind work for the simulations. Colored lines are contours of the wind work approximation (equation 3.6) for $\alpha = 1$.

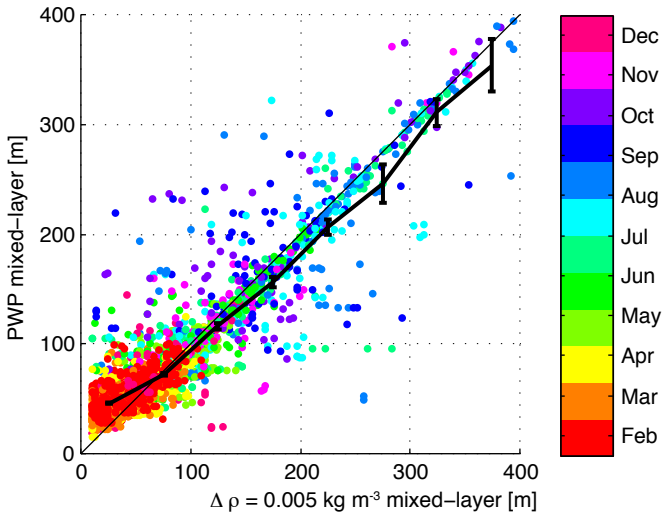

Figure 3.8: Mixing-layer thickness determined using the $\Delta\rho = 0.005$ kg m^{-3} compared to PWP simulated H. Each dot represents one simulation, similar to those illustrated in figure 3.7. The marker coloring indicates the month in which the float observations were made.

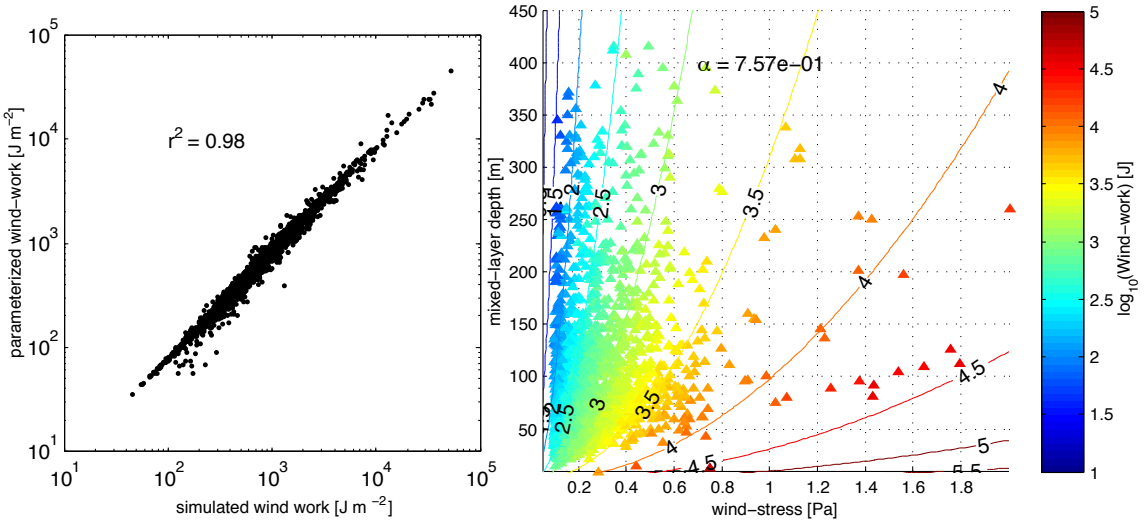

Figure 3.9: Comparison of wind work simulated using PWP to the parameterized wind work. Colored dots show integrated PWP wind work initialized with observed profiles and forced with an inertial wind pulse (as in figure 3.7). Contours show wind work derived from the parameterization $P = \frac{\alpha}{rf\rho}\frac{|\tau|^2}{H}$ (equation 3.6).

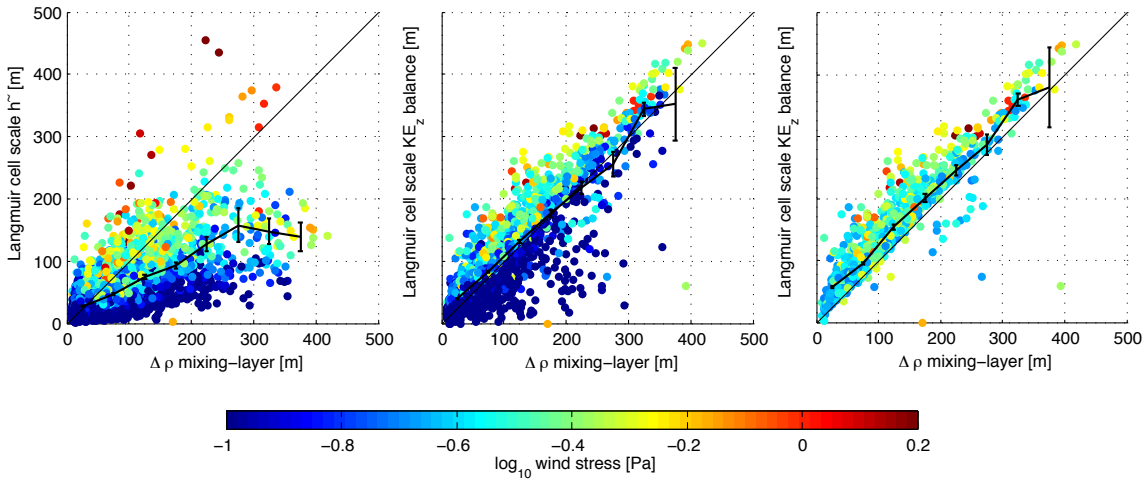

Figure 3.10: Comparison of parameterized Langmuir cell depth to observed mixing-layers determined using the $\Delta\sigma = 0.005$ kg m^{-3} criterion. Left panel; Langmuir cell depth from the $\tilde{h} = \frac{cu_*}{N}$ parameterization. Center panel; Langmuir cell depth estimated by balancing downwelling kinetic energy (from the scaling of Li and Garrett (1997)) to buoyant potential energy gain (from observed density profiles). Right panel; Same as in center panel limiting source data to profiles with corresponding wind-stress greater than 0.2 Pa.

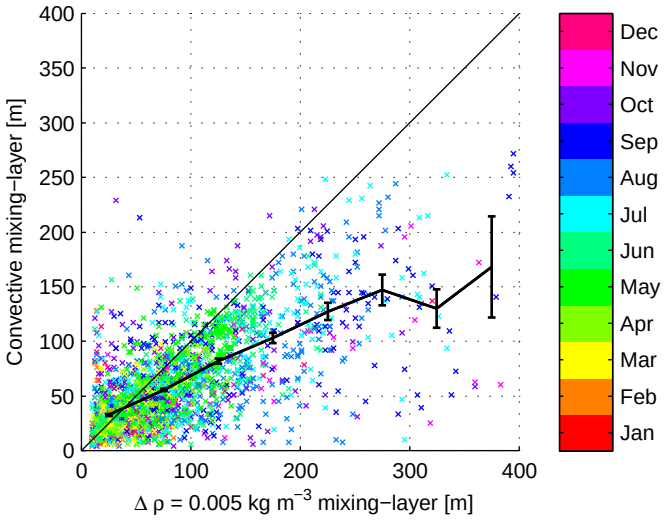

Figure 3.11: Comparison of mixing-layers forced by surface heat fluxes with the depth determined using the $\Delta\rho = 0.005$ kg m^{-3} criterion. Each dot represents the convection simulation for one density profile and the color represents the month of the year.

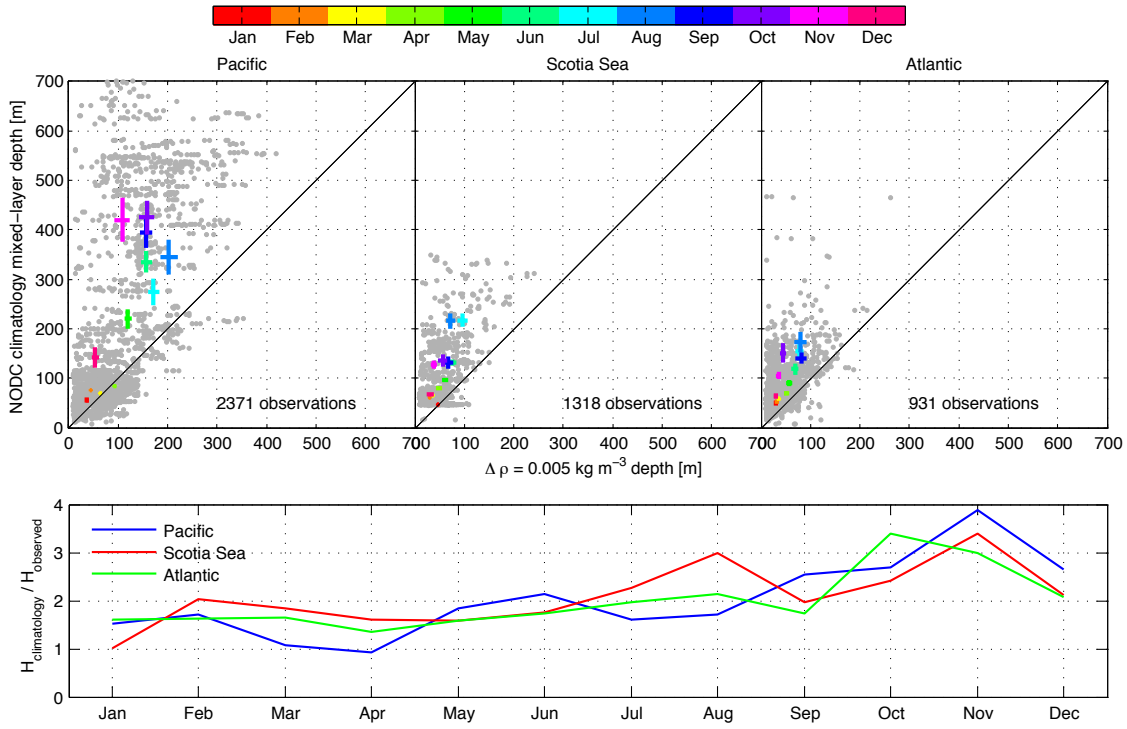

Figure 3.12: Comparison of observed depth of the $\Delta\rho = 0.005$ kg m^{-3} density difference with NODC climatological mixed-layer depths. Top panels; Results from the Pacific region of the Southern Ocean. Gray dots show each observation and the corresponding climatological mixed-layer depth. Monthly averages with 95% confidence limits are shown using colored lines. Bottom panel; Ratio of monthly average climatological mixed-layer depths to observations.

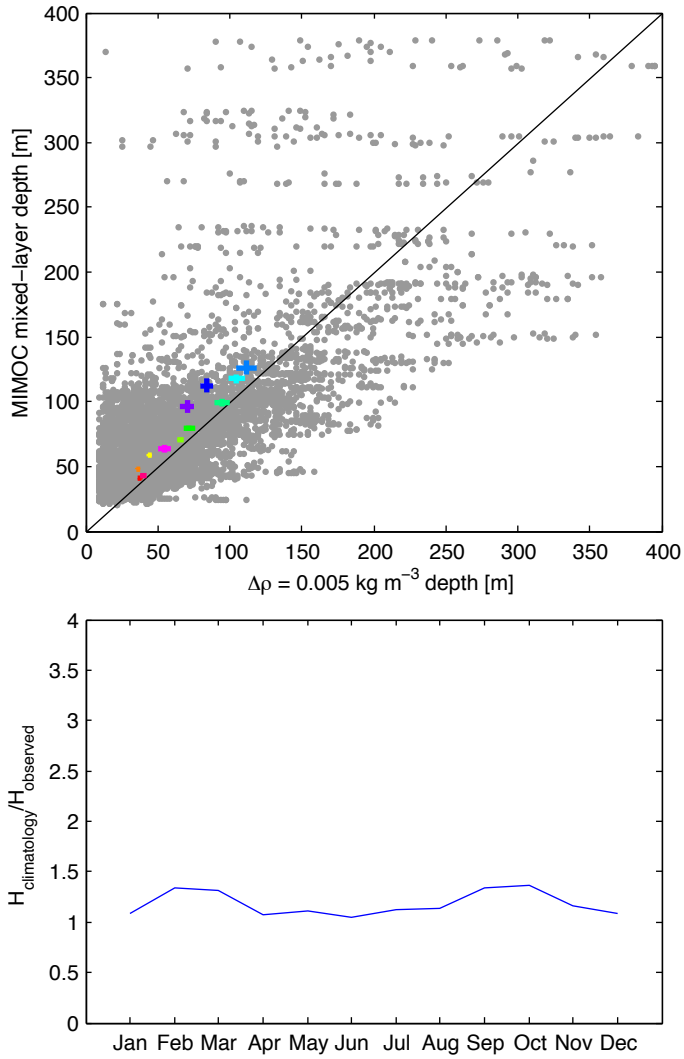

Figure 3.13: Comparison of observed depth (as in figure 3.12) of the $\Delta\rho = 0.005$ kg m^{-3} density difference with MIMOC climatological mixed-layer depths. Top; Gray dots show each observation and the corresponding climatological mixed-layer depth. Monthly averages with 95% confidence limits are shown using colored lines. Bottom; Ratio of monthly average MIMOC mixed-layer depths to observations.

Chapter 4

OBSERVATIONS OF NEAR-INERTIAL ENERGY IN THE ANTARCTIC CIRCUMPOLAR CURRENT

4.1 Introduction

Internal gravity waves near the local Coriolis frequency (also called the inertial frequency) contribute to energy dissipation in the ocean interior (Munk and Wunsch, 1998). Internal waves near the inertial frequency are generated at the ocean surface by wind (Webster, 1968; Pollard and Millard, 1970; Gill, 1984; D'Asaro, 1985), in the interior by baroclinic frontogenesis (D'Asaro et al., 2011), and at the sea floor when currents are forced over rough topography (Bell, 1975; Fu, 1981; Gill, 1982). Wind generated waves are most commonly observed, likely due to the combined effect of scientist's relatively better access to the upper ocean compared with the abyss and the difficulty of observing the upper ocean with sufficient resolution to observe frontal instability. In the data described here, observations of upward propagating features are far more common in the Scotia Sea, a region of rough and shallow topography, compared with the Pacific and Atlantic sectors.

This research was undertaken as part of the Diapycnal and Isopycnal Mixing Experiment in the Southern Ocean (DIMES). The core of the experiment was the release of 76 kg of CF_3SF_5 tracer in the eastern Pacific near 107° W and 58° S, between the Subantarctic (SAF) and the Polar Fronts (PF) of the Antarctic Circumpolar Current (ACC). Observations of the diapycnal diffusion of tracer were used to estimate diapycnal diffusivity throughout the Antarctic Circumpolar Current (Ledwell et al., 2011; Watson et al., 2013). Vertical profiles of horizontal velocity from profiling floats, which sampled along the approximate tracer path, were also used to estimate the upper ocean interior diapycnal diffusivity from vertical shear. In both the Pacific and Scotia Sea sectors of the Southern Ocean, estimates of diapycnal diffusivity from float data agree with those estimated from the vertical spread of the tracer. This suggests that internal waves, most of which are near f, supply sufficient

energy to maintain interior stratification in the Southern Ocean.

This study examines the the atmospheric and oceanic features which influence internal wave variability near the inertial frequency. The near-inertial component of the velocity record was isolated (Sanford, 1975) then decomposed into counterclockwise and clockwise rotary components (Gonella, 1972). Consistent counterclockwise rotation with depth is an indicator of downward propagation (Leaman and Sanford, 1975). The counterclockwise components of the velocity data were compared with with wind, satellite altimetry, and mixed-layer thickness. Clockwise signals, signifying upward propagation, were compared to topographic roughness and, where appropriate, to specific topographic features. Inertial-band shear and strain spectra were used to estimate diapycnal diffusivity following the method established in Gregg et al. (2003).

4.2 Data

The following analysis utilized float observations, gridded global winds, gridded global sea-surface-height, and high-resolution bathymetry.

4.2.1 Observed horizontal velocity, temperature, pressure, and salinity

Horizontal velocity and conductivity, temperature, and depth profiles were obtained from nineteen electro-magnetic autonomous profiler explorers (EM-APEX) (Sanford et al., 2005). These data include 7039 individual vertical profiles. These profiles span the breadth of the ACC, determined using closed sea surface height contours, from 110°W in the eastern Pacific to 20°W in the western Atlantic. Temporal coverage begins February 2009 and ends in September 2014 with the geometric center of the float's positions progressing approximately along with the tracer patch. These data were used to analyze 1229 profile 'bursts' (figure 4.1), each providing one estimate of inertial-band horizontal variability.

4.2.2 Global wind

Ocean surface wind from the Cross-Calibrated Multi-Platform level three gridded analysis (Atlas et al., 2011) is available with six-hour temporal resolution and 0.25° ($\sim$ 30 by 15 km

area) spatial resolution. These data from the ten-year period from 2002 through 2011 were used to derive float-following wind records and seasonally averaged inertial-band variance.

4.2.3 Satellite altimetry

Sea-surface height data from the French Research Institute for Exploitation of the Sea (IFREMER) Archiving, Validating, and Interpretation of Satellite Oceanographic data (AVISO) active dynamic topography product were used in this study. This product includes observed sea level anomalies and an estimate of the geoid (the geopotential surface underlying the anomalies). The data were available on a 0.33° grid ($\sim$ 20 by 40 km) with weekly temporal coverage from 1993 to 2014. Sea surface height data were used to compare with observations of inertial-band kinetic energy and to derive the long-term average sea-surface height field. A discussion of the validity of comparing these coarsely resolved data with *in-situ* observations is found in section 4.6.1.

4.2.4 Bathymetry

High resolution bathymetry was extracted from the SRTM30 Plus, 30 arc second (500 m spatial resolution), dataset (Smith and Sandwell, 1997). These data were used to compute topographic roughness, defined as the variance within 1° (56 by 112 km) bins, and to extract a float-following bathymetry record.

4.3 Quantifying near-inertial variance from EM-APEX velocity profiles

The EM-APEX floats were programmed to vertically profile in 'bursts'. The instruments drift along a prescribed neutral buoyancy level for up to ten days in a low-power state. The instruments then power up, and complete a set of vertical profiles such that the ascending profiles (see figure 4.1) are separated in time by one-half the local inertial period ($1/(2f)$, where $f = 2\Omega sin(latitude)$ is the Coriolis frequency and Ω is the angular velocity of the Earth). A full data profile is not typically collected on the final descent to conserve power. When available, the second descending profile can be used to estimate the fraction of 'near-inertial' variance observed in the ascending profiles.

The velocity data was linearly interpolated onto a uniform depth grid. Poor quality data were identified using both the float provided error value for each data point and by visual inspection. The instrument samples electric potential difference at 20 Hz, this is averaged into 1 Hz 'raw data', horizontal velocities are determined from a set of 50 1 s averages[1] using a least squares fit to a sine, cosine, linear trend, and a mean (Sanford et al., 2005). The residual after this fit is interpreted as the error level of the measurement. Errors are caused by real high-frequency (faster than the 50 s fit window) or high-wavenumber (less than 2.5 m) variance, or electromagnetic interference (Sanford, 1975). In addition to automated residual error, the instruments were observed to fail in novel and interesting ways which required human identification. Sunlight on the electrodes causes large horizontal current errors (John Dunlap 2013, personal communication). As battery voltage levels fall, the EM current sensing system performs decreasingly well; the result is many 'spikes' and weak signals. These errors were visually identified and manually removed from the dataset.

To account for minor variability in the actual time difference of the samples, each data point was rotated in time such that the time difference was exactly $\frac{1}{2f}$. This correction is applied to the full measured current and as a result may artificially introduce non-inertial variance into the differencing operation (ie when background currents are $\geq$ the wave amplitude). The correction introduces at most an error of 5% of the measured current into the half-inertial period differencing operation. When the background flow speed is less than that of the wave, this initial small amplitude back-rotation improves the quality of the half-inertial difference. Inertial-band currents ,(u_I, v_I), were diagnosed as the difference between the two interpolated, time-corrected ascending (and descending when possible) profiles (u_1, u_3, v_1, v_3)

$$u_I(z) = \frac{u_3(z) - u_1(z)}{2} \text{ and } v_I(z) = \frac{v_3(z) - v_1(z)}{2} \tag{4.1}$$

where z is the vertical coordinate (profile numbering in figure 4.1).

[1]the number of 1 s raw data to include in the fit is programmable, inclusion of more dat improves the estimate at the expense of vertical resolution

4.3.1 Evaluation of half-inertial differences

Half-inertial differencing isolates all variance within a frequency band from $0.9f$ to $1.1f$. Unfortunately, this band often includes semidiurnal tides since the local Coriolis frequency f at the observed locations varies from 64 to 94 % of the M_2 tidal frequency.

The half-inertial differencing operation is also vulnerable to signals outside of its bandwidth, such as aliased high frequency signals, and float motion through quasi-stationary vertical and horizontal variability. When depth-averaged horizontal current is strong, the assumption that two successive profiles sample the same location and wave signal is less accurate. This type of error impacts only a small subset of the data presented here when the barotropic velocity is unusually strong.

In the half-inertial difference variance at odd multiples of f (i.e. $3, 5, 7 \times f$) is indistinguishable from f. The buoyancy frequency N is approximately $7f$ in much of the sampled region. This is not an issue for velocity observations as internal waves near N have negligible horizontal velocity. However, this may contribute to the high levels of 'inertial-band' strain, which is used here in the parameterization of diapycnal diffusivity. Horizontal currents with frequency 3 and 5 f were assumed to be negligible as well based on the spectral levels of the Garrett and Munk internal wave frequency spectrum (Garrett and Munk, 1972; Cairns and Williams, 1976), although we have no observations to confirm this.

A technique was developed to better quantify the degree to which the half-inertial differenced velocity data contain real inertial-band variance (Sanford, 1975; Silverthorne and Toole, 2009). In most cases, portions of the descending profiles are separated sufficiently close to $\frac{1}{2f}$ to provide a second estimate of the inertial-band current (figure 4.1). The descending half-inertial differenced profiles often only apply to a limited subset of the ascending depth range. The time separation of the two inertial-band current profiles, from ascending and descending pairs, varies from about one hour at the surface to about seven hours at 1500 m. The descending profile was back-rotated at each depth at the local inertial frequency, f, to the time of the ascending profile. The lag-zero correlation coefficient was computed between the ascending and back-rotated descending inertial-band current profiles. The square of this correlation coefficient is the fraction of variance in the ascending profile

explained by pure inertial rotation with respect to time. The percent of observed variance attributable to inertial-band rotary current was defined as

$$R = \frac{c_u^2 + c_v^2}{2} \ , \tag{4.2}$$

where c_u and c_v are the lag-zero correlation coefficients of u_I and v_I respectively and R is the percent of variance explained by circular motion at the inertial frequency. This technique adds a measure of the quality of the assumptions (circular rotary motion at f, both profiles sample the same feature) inherent to the inertial-differencing operation.

4.3.2 Distribution of inertial-band kinetic energy

The spatial distribution of the observed inertial-band kinetic energy, defined as

$$E_I = \frac{\rho}{2}(u_I^2 + v_I^2) \ , \tag{4.3}$$

vertically integrated over the profile depth, is shown in figures 4.3 and 4.4. Observations which are both energetic and near-inertial appear to occur near the northern boundary of the study region. This is likely due to the presence at lower latitude of both a shallower pycnocline (Schmidtko et al., 2013) and enhanced inertial-band wind-forcing in these regions (Atlas et al., 2011). Overall, despite the sources of error described in section 4.3.1, the half-inertial differencing operation performs well. In the majority of profiles 50% or more of the variance is explained by motion at f (figure 4.5). In the following analysis, the observed inertial-band kinetic energy is multiplied by the corresponding percent of variance, R, attributable to near-inertial motion; this guards against false connections between non-inertial energetic events and the reference (wind, topography, etc) data.

4.3.3 Separation of inertial-band currents into rotary components

Inertial-band internal waves propagate both down from the surface and up from the sea floor. Downward propagating near-inertial internal waves in the Southern Hemisphere have a counterclockwise rotary polarization with respect to depth (Leaman and Sanford, 1975) while upward propagating waves have a clockwise polarization with respect to depth. The

observed (differenced) inertial-band current profiles were separated into counterclockwise (CCW) and clockwise (CW) components through the use of the Fourier transform

$$Z_I(k_z) = \int_{-\infty}^{\infty} (u_I(z) + iv_I(z))e^{i2\pi k_z z} dz \ . \tag{4.4}$$

The mean of $u_I(z) + iv_I(z)$ was removed and a Tukey window (Harris, 1978) with $\alpha = 0.2$ was applied to each current profile to eliminate ringing in the the transformed records. Rotary separation was achieved by partitioning the transformed velocity by the sign of vertical wavenumber k_z,

$$Z_{I+}(k_z) = Z_I(k_z > 0) \text{ and } Z_{I-}(k_z) = Z_I(k_z < 0) \ . \tag{4.5}$$

The time domain signals (u_+, v_+) and (u_-, v_-) were recovered using a the inverse Fourier transforms,

$$(u_+ + iv_+) = \int_0^{\infty} Z_{I+} e^{i2\pi k_z z} dk_z \text{ and } (u_- + iv_-) = \int_{-\infty}^{0} Z_{I-} e^{i2\pi k_z z} dk_z \ . \tag{4.6}$$

In the following analysis, the counterclockwise component (u_+, v_+) was used to calculate the kinetic energy in downward propagating near-inertial motions, which are assumed to be generated by wind. Similarly, the clockwise component (u_-, v_-) was used to calculate the kinetic energy in upward propagating near-inertial motions. The utility of this decomposition is clearly seen in figure 4.2; the total inertial-band current shows an apparent upward propagating beam on February 6th (figure 4.2). The separation into rotary components clearly identifies the apparent upward beam as clockwise polarized, coherent near-inertial motion.

4.4 Winds

Several previous studies have shown that inertial frequency oscillations in the surface mixed-layer, and waves in the stratified interior, are generated by the surface wind stress (Webster, 1968; Pollard and Millard, 1970; Thomson and Huggett, 1981; D'Asaro, 1985; D'Asaro et al., 1995; Alford, 2001; Klein et al., 2004; Jiang et al., 2005; Plueddemann and Farrar, 2006) . The author expected an approximate linear relationship between wind-stress and observed

inertial-band kinetic energy. No such relationship presents itself. Probable causes for the results shown here include: inaccuracies in the CCMP wind product, insufficient sampling of the internal wave field, observed near-inertial motions were not wind generated, and reduced wind power input due to deep mixing-layers.

4.4.1 Quality and availability of wind data

High frequency wind does generate near-inertial currents in the ocean. However we know that gridded-reanalysis winds do not capture the high-frequency changes in wind speed and direction that drive the inertial-band ocean response (Nyquist, 1928; Alford, 2001; Rimac et al., 2013; Kilbourne and Girton, 2015a). Spatial and temporal improvements in available wind forcing have increased the estimate of globally integrated wind-power input into near-inertial currents from 0.47 (Alford, 2003) to 1.1 (Rimac et al., 2013) TW. A comparison of six-hour resolution winds with those from *in-situ* observations of the same storm found vastly different estimates of the resulting wind-work, and that six-hour, 25° gridded winds cannot generally reproduce the impulsive nature of the wind-stress associated with a strong storm (Kilbourne and Girton, 2015a). The results of a comparison of wind-stress, determined using a speed-dependent drag coefficient (Large and Pond, 1981) (a reasonable approximation for winds below 25 m s^{-1} (Powell et al., 2003)), to the depth averaged counterclockwise inertial-band kinetic energy shows little relationship between these two quantities (figure 4.8).

The western Atlantic sector appears, based on the polarization and magnitude of the inertial-band currents observed, to have been the most likely sector in which to find a relationship between wind-stress and counterclockwise kinetic energy. Unfortunately, CCMP winds were only available through 2011 and the EM-APEX data in the Atlantic region spans 2011 through 2014. As a result few point comparisons of wind-stress to counterclockwise energy were possible.

Inertial-band wind forcing in the Atlantic, north of the Falkland Escarpment (figure 4.6), is stronger relative to the Pacific sector at the same latitude. Counterclockwise inertial-band kinetic energy observations in the Atlantic exhibit a strong seasonal cycle. This implies that, when reanalysis winds are available for comparison, a statistically significant relationship

should exist between inertial-band kinetic energy and wind-stress in the western Atlantic sector of the ACC.

4.4.2 Other factors

The generation of near-inertial oscillations is controlled by both the wind stress and the mixing-layer thickness, represented by $\vec{\tau}$ and H respectively in the damped-slab surface current response (Pollard and Millard, 1970) equation ($\vec{Z}$ is the complex horizontal current $u + iv$)

$$\frac{d\vec{Z}}{dt} + \omega\vec{Z} = \frac{\vec{\tau}}{\rho H} \ . \tag{4.7}$$

Although this equation has skill in reproducing observed surface currents (Pollard and Millard, 1970; D'Asaro, 1985; Plueddemann and Farrar, 2006), a comparison of inertial-band kinetic energy to the total forcing $\vec{\tau}/H$ does not indicate a clear connection between these quantities (figure 4.7). In the Pacific sector of the Southern Ocean $\vec{\tau}$ is comparatively reduced (figure 4.6) and the mixed-layers, H, are unusually deep. As a result, the typical relationship between wind-stress and counterclockwise kinetic energy (ie. wind stress and near-inertial ocean currents increase together) fails to appear (figure 4.8). Section 4.5 explores this topic in greater detail.

In the Scotia Sea the wind-stress, τ, is comparatively small, and internal wave signals from topography and tides are comparatively large. It is likely that the small amplitude of the downward propagating near-inertial signal is lost among the many other internal wave signals present in the region. It appears that much of the near-inertial variance in the Scotia Sea is connected to the presence of rough topography in this region, the effect of topography on wave generation in the Scotia Sea is investigated in section 4.7.

4.4.3 Insufficient sampling of the internal wave field

In this analysis the three geographic regions have been treated as if they were uniformly sampled in both space and time. This is far from the reality. Near-inertial motions are common (Elipot and Lumpkin, 2008a), they exist in measurable amplitude in nearly all of

the data presented here. In spite of this, finding a relatively large amplitude propagating wave with an unguided instrument is not unlike looking for the proverbial, "needle in a haystack". It is possible that because near-inertial internal waves are relatively small (the observed k_z of $\approx 1/200$ m^{-1} and $\omega = 1.05f$ suggests a horizontal wavelength of ≈ 30 km) and infrequent (there are five well resolved waves in more than seven thousand vertical profiles), the floats simply did not observe the wind generated propagating waves that were present in nature.

4.5 Mixed-layers

In all regions, the wind is stronger during the austral winter (figure 4.6). Its impact on the generation of inertial-band currents is moderated by the thickness of the actively-mixing layer H (equation 4.7). Mixing-layer thickness, H, was identified as the depth at which the sorted potential density profile exceeds 0.005 kg m^{-3} difference from the surface density (Kilbourne and Girton, 2015b). The results presented here (and in figure 4.9) show that mixed-layers are deeper during the austral winter in each region. In the Pacific sector both deep mixed-layers and the low levels of counterclockwise inertial-band kinetic energy were found during the austral winter.

The results in the Atlantic sector hint at the opposite trend. Although the uncertainty is large (figure 4.9), counterclockwise inertial-band energy in the Atlantic sector appears to increase with mixing-layer thickness. Since thicker mixing-layers tend to diminish the inertial current response, this suggests a compensating increase in the wind forcing.

In the Scotia Sea, counterclockwise kinetic energy is largest in the austral summer, when wind stress is weakest. Downward propagating wave energy appears to follow the seasonal cycle of mixed-layer thickness in the Scotia Sea. This result highlights the importance of the mixed-layer in modulating the near-inertial wind power input.

4.6 Geostrophic vorticity

Many previous studies (Kunze, 1985; Mied et al., 1987; Lee and Niiler, 1998; Zhai et al., 2005, 2007) have investigated the effect of mesoscale vorticity on near-inertial motions. These studies explore the behavior of internal waves in the presence of mesoscale vorticity features.

EM-APEX observations of inertial-band kinetic energy offered an opportunity to test these ideas through comparison to satellite estimates of geostrophic vorticity. Near-inertial wave ray-paths are strongly controlled by horizontal and vertical gradients in the mean current and buoyancy field (Kunze, 1985). Effective vorticity $f_{eff} = f + \zeta/2$ replaces planetary vorticity in the internal wave dispersion relation, ζ (equation 4.9) is the vertical component of vorticity calculated from the satellite altimetry field. Positive vorticity anomalies, or anticyclones, tend to bend near-inertial wave ray paths towards their centers and trap or significantly alter wave properties.

In some regions the position of the ACC appears to be strongly controlled by sea floor topography. In these regions, which include the Kerguelen Plateau, Macquarie Ridge, Udintsiv and Eltanin fracture zones, and the Scotia Sea, the position of the mean flow is quasi-stationary in time. The original hypothesis driving the comparison of the observations with the vorticity field was that, the frequent storms in the region (visual inspection of CCMP winds shows storms about once a week, the power-spectrum of wind speed (not shown) has a peak at 0.1 cpd) provide a statistically steady supply of near-inertial waves, which stationary positive vorticity anomalies would attract and possibly trap. Several of the strongest stationary vorticity features in the ACC are found in the Scotia Sea. Observations of inertial-band kinetic energy was compared to long-term mean and weekly vorticity fields to test this hypothesis.

4.6.1 Satellite altimetry

Twenty two years of weekly, 0.33° gridded estimates of absolute dynamic topography (courtesy of IFREMER/AVISO) were used to estimate the long-term average geostrophic current in the ACC. The mean sea surface height field $\bar{h}$ (figure 4.10) was used to estimate the width of the ACC using the northernmost and southern most closed contours around Antarctica. The northernmost closed contour was found at 20 cm, the southernmost closed contour (partially incomplete due to ice coverage and satellite limitations) was found at -110 cm. The mean positions of the Subantarctic Front, Polar Front, and Southern ACC Front were identified as the 0, -30, and -70 cm sea surface height contours respectively. The position

of these contours appears to be strongly controlled by sea floor topography (figure 4.10 top panel).

The horizontal gradients of sea surface height h were found using centered-differences. Geostrophic currents,

$$U_g = \frac{-g}{f}\frac{dh}{dy} \text{ and } V_g = \frac{g}{f}\frac{dh}{dx}, \tag{4.8}$$

were used to determine the mesoscale vorticity

$$\zeta = \left(\frac{dV_g}{dx} - \frac{dU_g}{dy}\right)\hat{k} \tag{4.9}$$

($\hat{k}$ is the vertical unit vector, the horizontal elements of ζ have been omitted). Each iteration of the centered differencing operation increases the 'footprint' of the data by 40 km, resulting in approximately 120 km spatial resolution of the vorticity estimate.

4.6.2 Comparison to observations

In the Southern Hemisphere the ratio f_{eff}/f is less than one when the mesoscale vorticity is positive. The inertial band kinetic energy was compared to both the mean and weekly vorticity estimates (figures 4.11 and 4.12 respectively). Higher inertial-band kinetic energy levels were expected in positive vorticity regions. However, the comparison does not clearly indicate a pattern.

In the Scotia Sea, which is the region in which vorticity anomalies were both strong ($f_{eff} \geq 1.1f$) and stationary in time, the comparison shows far more energy associated with negative vorticity features. A possible explanation for this curious result is that the observed inertial-band energy is due to topographic lee waves. In the limited case where the background flow generating these waves is constant, the waves are fixed in space near their generation sites. Where topographic waves have frequency near f and occur in a region of negative vorticity, comparison of energy to satellite derived vorticity in not useful. This may explain the results in the Scotia Sea, where near-inertial lee waves were observed (figure 4.14) the mesoscale vorticity is negative (figure 4.10).

The Scotia Sea region contains very sharp, very large gradients in the geostrophic flow field. Float trajectories in the lee of Drake Passage show that the geostrophic flow speed

drops from greater than 1 to 0.01 m s^{-1} over just a few kilometers. Given the very poor spatial resolution of the satellite derived vorticity field, it is unlikely that the vorticity field used here accurately reflects the *in-situ* conditions sampled by the floats.

The results from the Pacific and Atlantic sectors show a slight trend toward greater energy in positive vorticity regions (figures 4.11 and 4.12 upper and lower right side panels) as would be expected from the broadening of the internal wave frequency band. The energy levels were found to be significantly elevated (with 95% confidence) in the Pacific sector comparison of inertial-band kinetic energy to weekly vorticity fields. These statistically significant results in the Pacific were surprising for two reasons: 1) The poor spatial resolution of the vorticity estimate reduces the likelihood that the weekly vorticity estimates accurately reproduce the transient eddy field found in the Pacific, because eddies are moving features and generally smaller than the 120 km resolution of the vorticity estimate. 2) Pacific sector vorticity is comparatively weak and ray-tracing simulations indicate that much stronger vorticity is required meaningfully alter the wavevector.

Taken together these comparison provide some hint that positive vorticity anomalies attract near-inertial wave energy. However, the results also highlight the difficulty in such comparisons. As both observations and models improve the resolution of mesoscale features (0.1° degree data may be sufficient) the ability of mesoscale vorticity to shape the spatial distribution of inertial energy may become more clear.

4.7 Topographic roughness and upward propagating waves

The DIMES tracer was released in a relatively quiescent area in the eastern Pacific sector of the Southern Ocean. Initial results in this region showed weak mean flow, background levels of diapycnal diffusivity, and predominantly downward propagating internal waves (Ledwell et al., 2011; Kilbourne and Girton, 2015a). As the tracer moved downstream into the Drake Passage and Scotia Sea, dramatic changes were observed. The diapycnal diffusivity diagnosed from the vertical distribution of the tracer increased by more than an order of magnitude (Watson et al., 2013; Sheen et al., 2013) between measurements upstream and downstream of the Drake Passage. Data from EM-APEX instruments were similarly changed. Two floats launched into the Subantarctic Front just upstream of the Tierra del

Fuego Spur (figure 4.13) passed through vertical velocities w in excess of 0.12 m s^{-1}, likely the effect of topographic lee waves. These data provided early indication that the Scotia Sea was a much more energetic background environment than the quiescent conditions observed in the Pacific.

4.7.1 Topographic control of mean currents

The locations of the geostrophic currents that comprise the ACC are controlled by the shallow and varying topography in the Scotia Sea (figure 4.10 top and center panels). The Subantarctic Front (SAF) is forced southward upstream of Drake Passage then immediately veers northward following the South American continental slope. The long-term position of the 0 m sea surface height (SSH) contour, used as a proxy for the SAF, exits the Scotia Sea east of the Burdwood Bank and continues following the continental slope (see figure 4.13 for placenames). The Polar Front (PF) enters the Scotia Sea near 58°S at a deep passage through the Shackleton Fracture Zone and follows the West Scotia Ridge to the Shag Rocks Passage. The Southern ACC Front enters the Scotia Sea near the southern edge of the West Scotia Ridge, and exits through the Georgia Passage east of South Georgia island.

4.7.2 Large vertical velocities / Lee waves

Very strong vertical velocities were observed in the Scotia Sea. Vertical velocities sufficient to carry the float to the opposite direction of its profiling direction were observed in the lee of the Tierra del Fuego Spur. The approximate Lagrangian frequency of this wave was determined from the timing of anomalous peaks in measured $\frac{dP}{dt}$, which were separated in time by 1 hour. This is consistent with expectations for a topographic lee wave with a Lagrangian frequency near N (Gill, 1982). Similarly large vertical velocities were also seen near the Shag Rocks Passage. In the latter case insufficient data were collected to estimate the Lagrangian frequency, but the observations were consistent with variation at N. The profiles of horizontal velocity during these periods show very large background speed (> 1 m s^{-1}) and a highly energetic internal wave field (seen in wavenumber spectra), but in both cases little of the observed variability falls within the inertial-band. These

observations are currently being investigated by J.Cusack (at the National Oceanography Centre Southhampton).

4.7.3 Inertial-band variability

The Scotia Sea is unique in this study in that, on average, as much internal wave energy is propagating upward as is downward. In order for these signals to appear coherent in the clockwise/counterclockwise rotary decomposition, the current must vary at or near f and have rotary structure with respect to depth. A particularly interesting wave was observed by float 4976 in February 2011 (figure 4.14). Inspection of the individual differenced profiles shows clockwise rotary structure with respect to depth, indicative of upward energy propagation. The Lagrangian frequency, ω, (if the mean flow is approximately barotropic the Lagrangian frequency is observed by these floats) of topographic lee waves is determined by

$$k_T = \frac{\omega}{|U|} \tag{4.10}$$

where k_T is the topographic wavenumber and U is the background flow speed. The waves investigated here have frequency indistinguishable from f = -1.22 $\times$ 10^{-4} rad s^{-1} and flow speed U = 0.4 m s^{-1} was inferred from GPS positions, our best estimate of the the barotropic flow. The topographic wavelength, λ_H, needed to generate inertial-band lee waves was found by substitution of these values into 4.10

$$\lambda_H = k_T^{-1} = \frac{U}{|f|(2\pi)^{-1}} \approx 21.04\,\mathrm{km}\,. \tag{4.11}$$

This gives the width of the seamount needed for near-inertial lee wave generation under the observed flow speeds. The uncertainty in this estimate is due to temporal and spatial variability in the background geostrophic flow. These observations do not directly measure this, but float trajectories suggest that the position of the ACC fronts varies significantly. The width of the seamount in figure 4.14, along the float trajectory, was approximately 31.8 km. Given the uncertainty in the mean flow and the exact angle of the trajectory across the seamount (which are large and difficult to quantify), it is plausible that the observed upward propagating beam is a near-inertial topographic lee wave generated by the seamount.

These well resolved observations of topographic lee waves with frequency near f and N provide evidence of the prevalence of these waves in the Scotia Sea. To quantify the impact of upward propagating waves on internal wave energy levels, clockwise-polarized kinetic energy was compared with topographic roughness (defined as the variance within 1° bins). The results of this comparison show that upward propagating inertial-band kinetic energy increases with topographic roughness (figure 4.15). A separate, similar comparison (figure 4.16) indicates that upward propagating kinetic energy is inversely correlated to bottom depth. These results suggest that upward propagating waves contribute significantly to upper ocean internal wave variance when topography is both rough and relatively shallow.

4.8 Contribution of observed internal waves to diapycnal diffusivity

4.8.1 Inertial-band shear and strain spectra

Internal waves transport energy horizontally and vertically away from generation sites. The focus of this study is primarily the vertical transport of wind energy into the ocean interior, but the lateral flux of wave energy out of the Southern Ocean may also be significant. These diffusivity estimates assume the observed wave energy is dissipated within the region (ie Pacific, Scotia Sea, Atlantic) in which it is observed. These analyses also assume that the observed energy is dissipated in the upper 1500 m. This last assumption is qualitatively supported by our observations of internal wave energy (none of the well sampled beams appear to reach the 1500 m limit of our measurements), but is impossible to verify.

Internal waves lose energy through vertical shear instability, which is enhanced when the vertical wavenumber becomes large. One scenario where this is known to happen is when a subinertial ($f_{eff} < \omega < f$) wave packet reaches its critical depth in a positive vorticity anomaly (Kunze et al., 1995). The inverse of this scenario may occur when upward propagating waves encounter this critical depth from below. Several efforts have been made to generalize the contribution of internal waves to energy dissipation in the ocean interior (Polzin et al., 1995; Gregg et al., 2003). In the following analysis, inertial-band current profiles (determined using half-inertial period differencing) were used to calculate the rotary vertical wavenumber spectrum of inertial velocity

$$\phi_V(k_z) = \widehat{Z_I(k_z)} \cdot \overline{\widehat{Z_I(k_z)}} \cdot \frac{dz}{L} \tag{4.12}$$

and inertial shear

$$\phi_S = (i2\pi k_z) \cdot \overline{(i2\pi k_z)}\ \phi_V\ , \tag{4.13}$$

where ϕ_V is the variance conserving spectrum of the inertial-band current. ϕ_S is the vertical wavenumber spectrum of vertical shear, dz is the depth spacing of the measurements, overbars represent the complex conjugate, and L is the number of data in the record (1024 in the spectra presented here, figure 4.17). The shear spectrum ϕ_S (figure 4.17) was separated into counterclockwise and clockwise components by the sign of wavenumber k_z,

$$\phi_{S+}(k_z) = \phi_S(k_z > 0) \text{ and } \phi_{S-}(k_z) = \phi_S(k_z < 0)\ . \tag{4.14}$$

These shear spectra were used to compute the ratio of counterclockwise to clockwise shear $\frac{\phi_{S+}}{\phi_{S-}}$, a proxy for the local importance of downward propagating (wind generated) versus upward propagating (bottom generated) inertial internal waves (Leaman and Sanford, 1975). The resulting ratios are shown in figure 4.20 displayed by geographic sector and by month of the year. The ratios indicate that in the western Atlantic and eastern Pacific sectors of the Southern Ocean, downward propagating waves dominate the inertial-band of the internal wave field. The ratios follow seasonal cycles in the wind and mixed-layer thickness in both regions. The partition of energy in the Scotia Sea appears to be roughly equivalent, with equal contributions to shear from both upward and downward propagating waves.

Inertial band variability in temperature and salinity was derived using the half-inertial difference operation on full temperature and salinity profiles. The temperature anomaly and mean,

$$T_a = T_3 - T_1 \text{ and } T_m = \frac{T_3 + T_1}{2} \tag{4.15}$$

respectively, were calculated from each pair of profiles (1 and 3 on figure 4.1). A similar procedure was used to find the salinity anomaly and mean S_a and S_m. These inertial-band

temperature and salinity profiles were used to compute the anomalous potential density profile $\rho_a(S_m + S_a, T_m + T_a)$ and the mean potential density profile $\rho_m(S_m, T_m)$. The buoyancy frequency of the anomalous and mean potential density profiles, N_a and N_m, were used to calculate the inertial-band vertical strain

$$\eta_z = \frac{N_a^2}{N_m^2} - 1 \ . \tag{4.16}$$

The vertical wavenumber spectrum of inertial-band strain

$$\xi_z(k_z) = \widehat{\eta_z(k_z)} \cdot \overline{\widehat{\eta_z(k_z)}} \cdot \frac{dz}{L} \tag{4.17}$$

was computed for each half-inertial difference. These inertial-band strain estimates are much more likely to be contaminated by variance at $3f$, $5f$, and $7f$ because the aspect ratio of the wavevector becomes more horizontal (ie greater vertical displacement) as ω approaches $N \approx 7f$. Despite this, these strain spectra are useful in that finescale strain data is rare in general and even more so in the Southern Ocean. These inertial-band shear and strain provide important context for future work in understanding the internal wave field in the ACC.

4.8.2 Estimates of diapycnal diffusivity

Shear spectra computed from the original velocity profiles (figure 4.22) were used to parameterize diapycnal diffusivity following the method established in Gregg et al. (2003) and Kunze et al. (2006). Strain spectra computed from half-inertial differences are inappropriate for comparison to the full shear spectrum, and computation of the full strain spectrum requires an (unknown) reference buoyancy profile. In place of locally computed strain, the shear to strain ratio $R_\omega = 7$ was used (Kunze et al., 2006). The resulting diapycnal diffusivities, computed over the depth 200 to 1500 m depth range,

$$\kappa = \kappa_0 \frac{\langle \phi_S \rangle^2}{\langle GM \phi_S \rangle^2} h_1(R_\omega) j(f/N) \, , \tag{4.18}$$

(Kunze et al., 2006) are shown in figures 4.23 and 4.24. EM-APEX estimates of diapycnal diffusivity in the eastern Pacific sector of the ACC are $1.96 \pm 0.36 \times 10^{-5}$ m^2 s^{-1} and in the

Scotia Sea that estimate jumps to $1.08\pm0.08\times10^{-4}$ m^2 s^{-1} compared to $1.3\pm0.2\times10^{-5}$ m^2 s^{-1} and $0.7\pm0.2\times10^{-4}$ m^2 s^{-1} from tracer observations. A central goal of DIMES was to directly measure the interior diapycnal diffusivity in the Southern Ocean. These results suggest that EM-APEX measurements of vertical finestructure are capable of providing credible estimates of diapycnal diffusivity in the ocean interior.

4.9 Conclusions

4.9.1 Inertial-band wind forcing

The results presented here show little to no relationship between contemporary values or monthly averages of wind-stress and counterclockwise polarized inertial-band kinetic energy. The time scale for the majority of the energy in surface oscillations to radiate into the stratified interior is not more than a few inertial periods (D'Asaro et al., 1995) (less than one week at this latitude), and this suggests that a correlation should exist between monthly averages of wind and inertial-band wave energy (similar to results in Alford et al. (2012)). The lack of this relationship in the data presented here suggests that the *in-situ* near-inertial energy is a more complex function of vorticity, mixed-layer thickness, wind stress, and horizontal advection than previously assumed. As a result, it is difficult predict upper ocean near-inertial energy from wind stress alone (Plueddemann and Farrar, 2006).

4.9.2 Mixed-layer thickness

In the Pacific sector, inertial-band kinetic energy is lowest during the austral winter, when the wind forcing is greatest (figures 4.6 and 4.8). During this time, mixing-layers are deepest (figure 4.9). Upper-ocean stratification generally enhances the wind power input and subsequent transfer into the ocean interior. Seasonal erosion of the pycnocline in the Pacific sector allows the formation of very deep mixing-layers (Kilbourne and Girton, 2015b); these dilute momentum and reduce the dot product of $\vec{\tau}$ and $\vec{Z}$ (the wind power input (D'Asaro, 1985)). The inertial-band kinetic energy in the western Atlantic and Scotia Sea sectors is not impacted in the same way due to the presence of a permanent pycnocline in these regions.

4.9.3 Effective vorticity

Positive mesoscale vorticity features refract near-inertial wave rays towards their centers and also trap locally generated waves with frequency between f_{eff} and planetary f (Kunze, 1985). Because of this, increased near-inertial energy was expected to be found in regions of positive vorticity. Comparison of all observed inertial-band kinetic energy to weekly and long-term average geostrophic vorticity shows a weak, statistically insignificant, trend towards regions of negative vorticity (figures 4.11 and 4.12). This result contradicts expectations and is likely due to the poor resolution in the satellite-derived vorticity field. Additionally topographic lee waves are spatially constrained near their generation sites, which may be coincident with negative vorticity regions, as is the case in the wave shown in figure 4.14. In the Pacific sector, where the geostrophic vorticity is both weak and unsteady, observations of greater energy in positive vorticity regions weakly indicates that internal wave energy is impacted by the mesoscale vorticity field.

4.9.4 Variations across the Pacific, Atlantic, and Scotia Sea

There are large differences in the both the observed inertial-band energy and background conditions across the eastern Pacific, Scotia Sea, and western Atlantic sectors of the Southern Ocean studied here. Observations in the eastern Pacific are mostly over the abyss, with little direct forcing from topography to shape the flow field. Unusually deep mixing-layers appear to dominate the temporal distribution of near-inertial energy. The circumpolar band of peak near-inertial winds (figure 4.6) intersects with the ACC, and the float trajectories, in the western Atlantic sector of the Southern Ocean. In this region, observations of near-inertial kinetic energy follow the seasonal cycle of inertial-band wind stress.

1. The seasonal cycle of inertial-band variance in the Pacific is primarily controlled by mixed-layer thickness. Deep mixed-layers reduce the power transferred from the wind into near-inertial motions thereby inhibiting the formation of propagating inertial-internal waves. As a result the seasonal cycle of inertial-band kinetic energy is out of phase with the seasonal cycle of the winds.

2. The inertial-band kinetic energy in the Scotia Sea is primarily generated by interactions between the geostrophic currents and the region's rough sea-floor topography. The results presented here show the greater fraction of inertial-band energy to be clockwise polarized, or upward propagating, indicating that wind-driven near-inertial waves have a reduced role in the observed inertial-band internal wave variance in the Scotia Sea. Estimates of diapycnal diffusivity determined from vertical finestructure are greatly enhanced in this region, likely due to rough and shallow topography, consistent with other results from the region (Brearley et al., 2013; Sheen et al., 2013).

3. In the Atlantic sector of the Southern Ocean the seasonal cycle of inertial-band variability is driven by seasonal variation in surface wind stress. The presence of a permanent pycnocline near 100 m depth, combined with relatively strong winds, allows for the transfer of more energy into near-inertial internal waves relative to the Pacific.

4. Diapycnal diffusivity, estimated from vertical finestructure, is similar to estimates of the same quantity from observations of the vertical spreading of tracer in the Diapycnal and Isopycnal Mixing Experiment in the Southern Ocean (Ledwell et al., 2011; Sheen et al., 2013; Watson et al., 2013).

4.10 Acknowledgments

This research was funded through NSF grants OCE0623177 and OCE1129564 and later through the generosity of the Applied Physics Laboratory and Department of Oceanography. This work could not have been accomplished without the insight of the following people: Eric Kunze, Thomas Sanford, John Dunlap, Avery Snyder, Brian Chinn, Haley Dosser, and so many others.

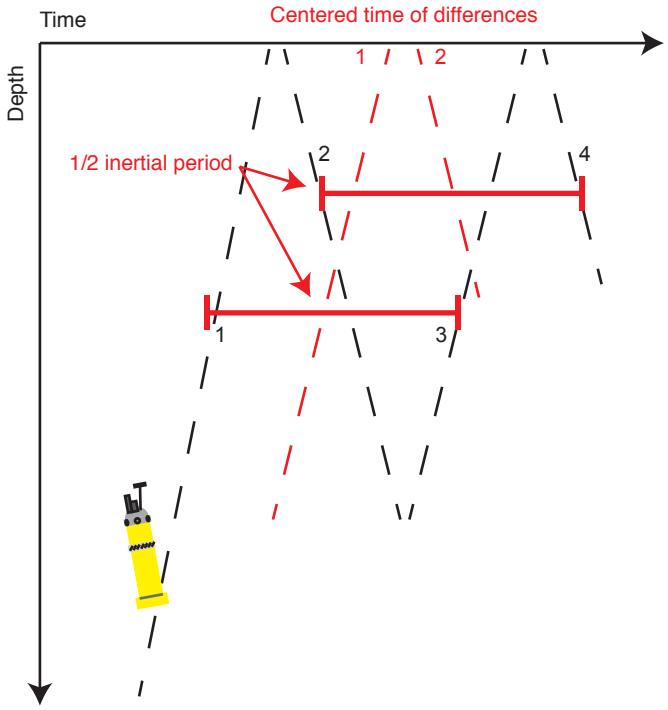

Figure 4.1: A schematic showing the burst pattern for sampling variance near the inertial frequency. After a preset drift period (typically several days) the float ascends (float trajectory shown as the black-dashed line), descends, and ascends again such that the two ascending profiles are separated in time by approximately one-half the local inertial period.

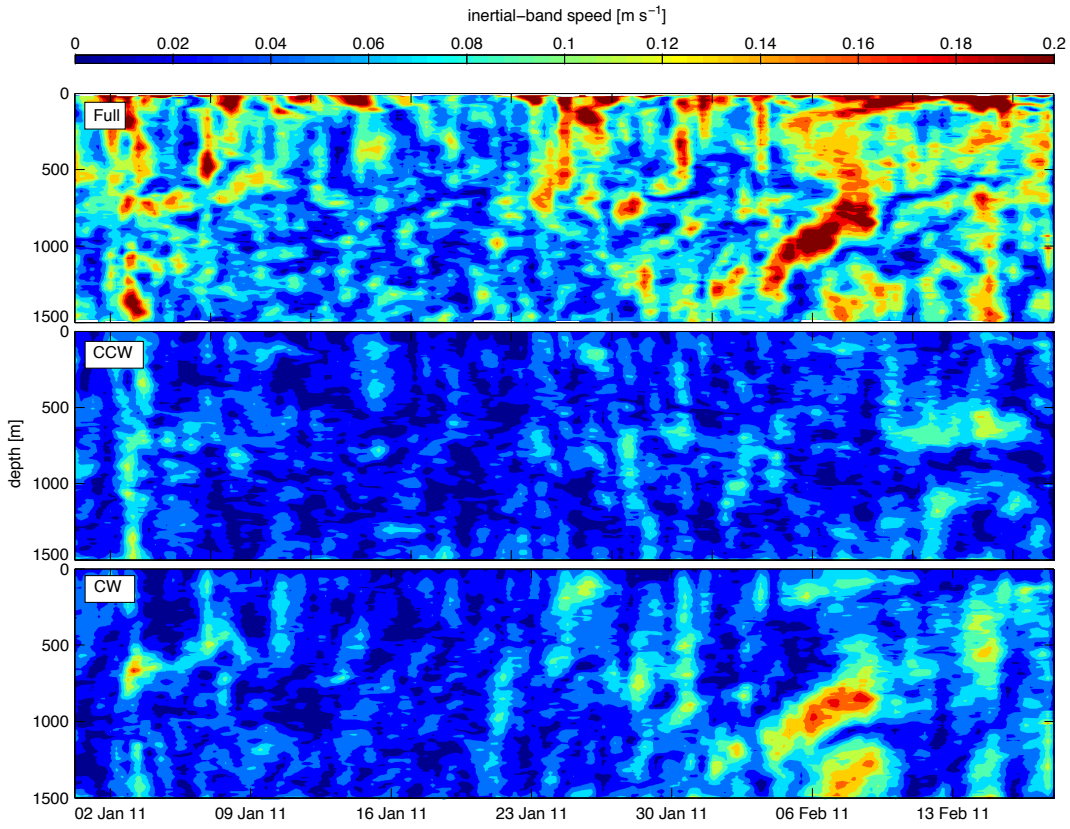

Figure 4.2: The decomposition of the full, inertial-band, velocity profile into clockwise and counterclockwise components. In this example, which is derived from float 4976, the large and apparently upward propagating feature (February 6th) is clearly identified in the clockwise portion of the data, consistent with expectations for an upward propagating wave.

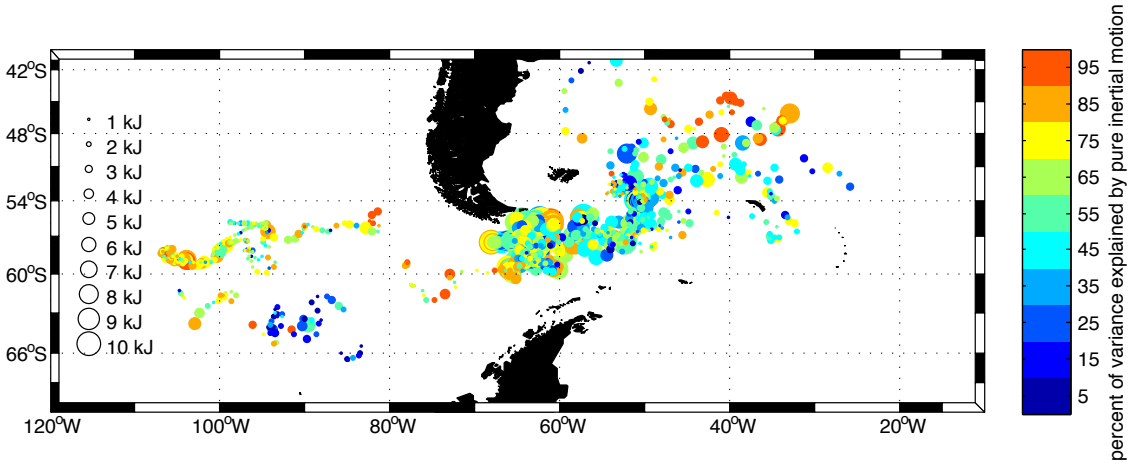

Figure 4.3: Depth-integrated near-inertial band kinetic energy from half-inertial period differences. The size of each circle represents the energy (scale at left) and the color shows the percent of inertial-band variance attributable to each observation. By example, circles which are both large and red-orange represent events which are both energetic and nearly inertial.

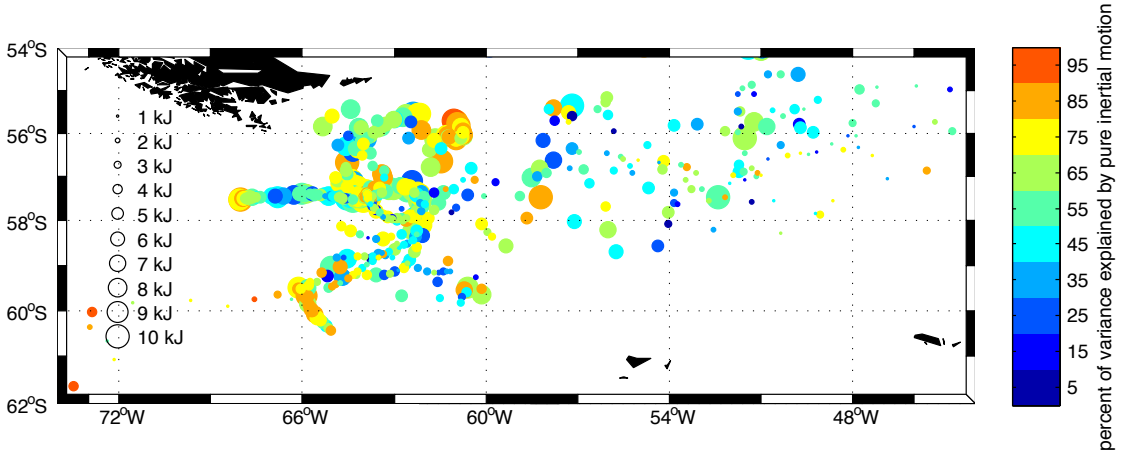

Figure 4.4: As in figure 4.3, showing a close-up of the Scotia Sea region.

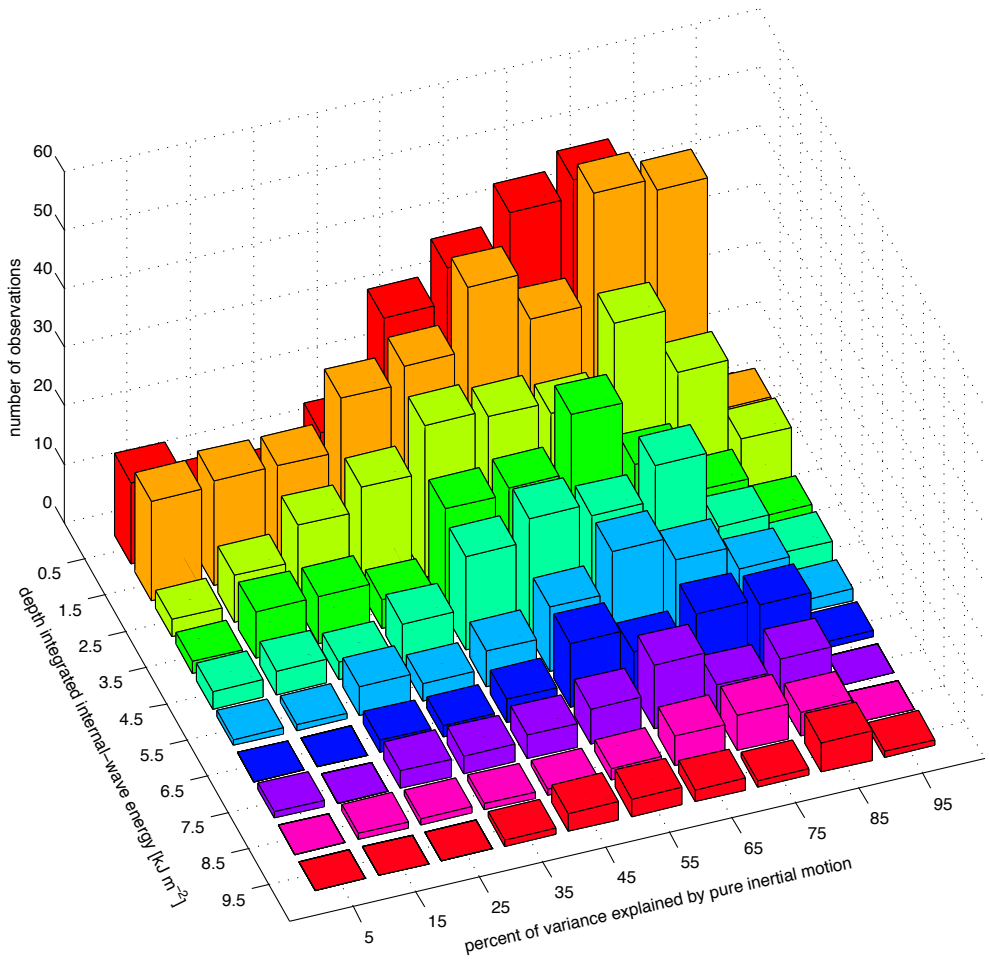

Figure 4.5: The distribution of half-inertial difference observations with respect to the percent of observed variance explained by purely inertial motion and the depth integrated inertial-band kinetic energy.

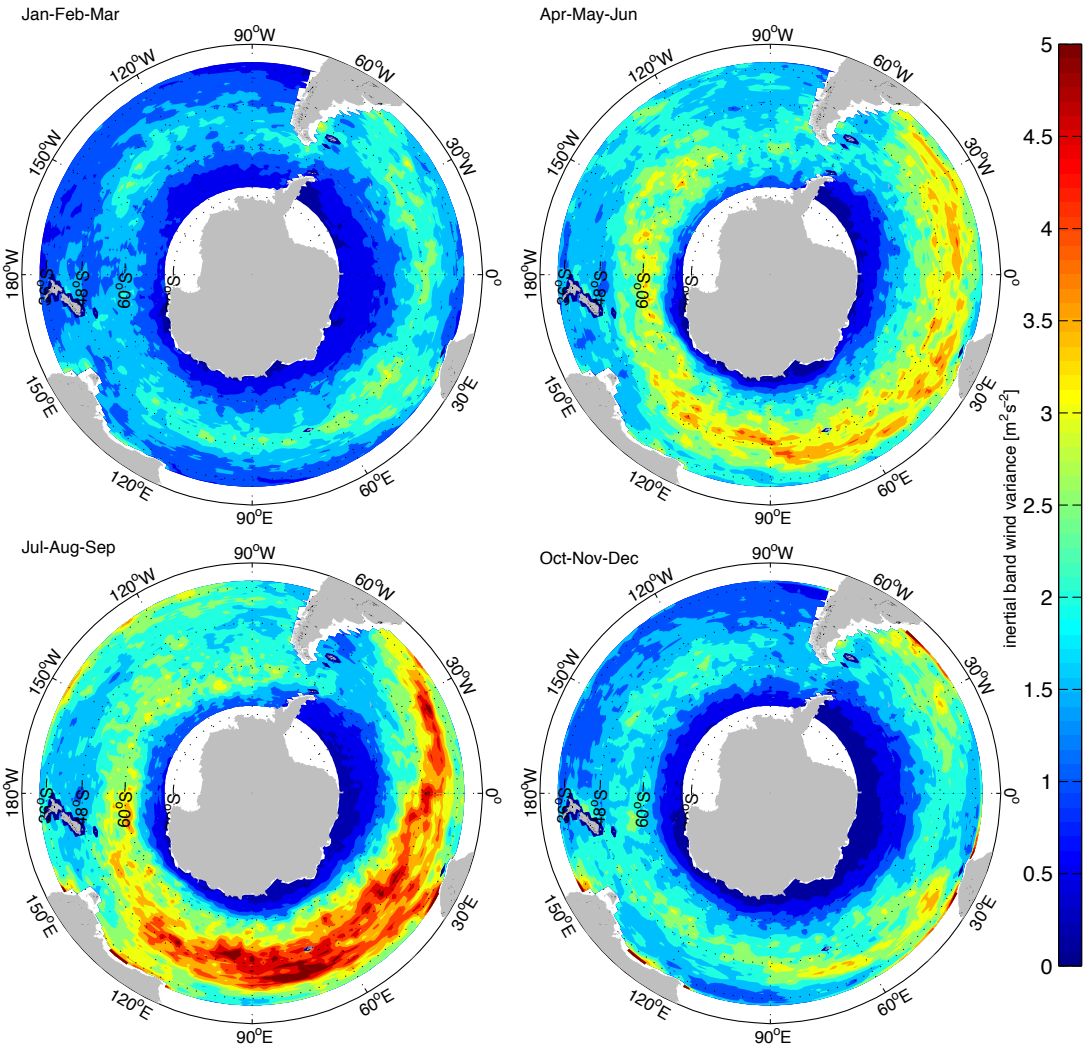

Figure 4.6: Seasonally averaged near-inertial wind variance. Near-inertial variance is determined by integrating the $0.9f$ to $1.1f$ portion of the frequency spectrum of CCMP winds in each season from the years 2001 through 2011.

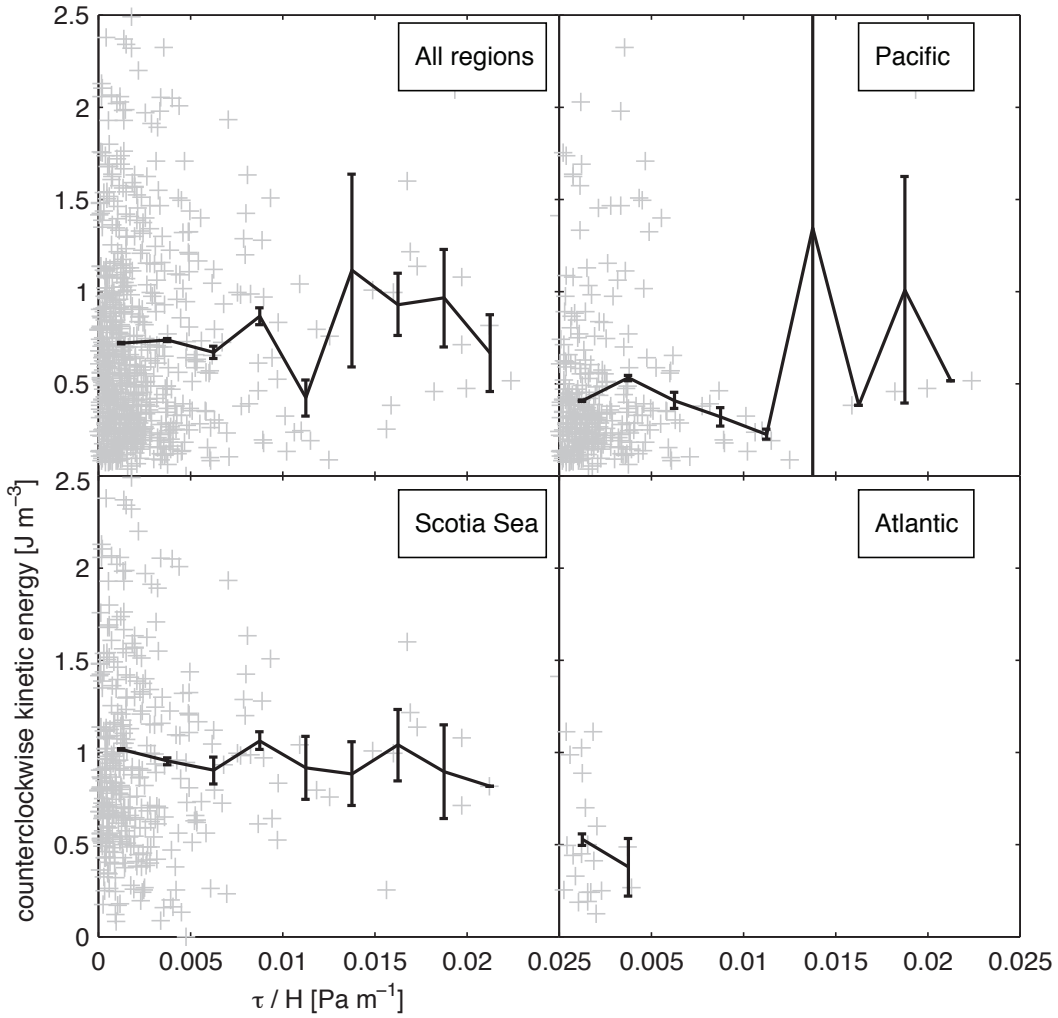

Figure 4.7: Comparison of estimated total forcing $|\tau|/H$ to the depth-averaged counterclockwise near-inertial kinetic energy across all regions (upper left) and in the Pacific, Scotia Sea, and Atlantic sectors of the Southern Ocean. τ was determined using CCMP wind vectors interpolated onto the observation locations and mixed-layer thickness was determined using a 0.005 kg m^{-3} density difference criterion. Each gray cross shows $|\tau|/H$ and CCW kinetic energy at one observation, the colored lines show the 95% confidence limits (along both axes) of the monthly averages.

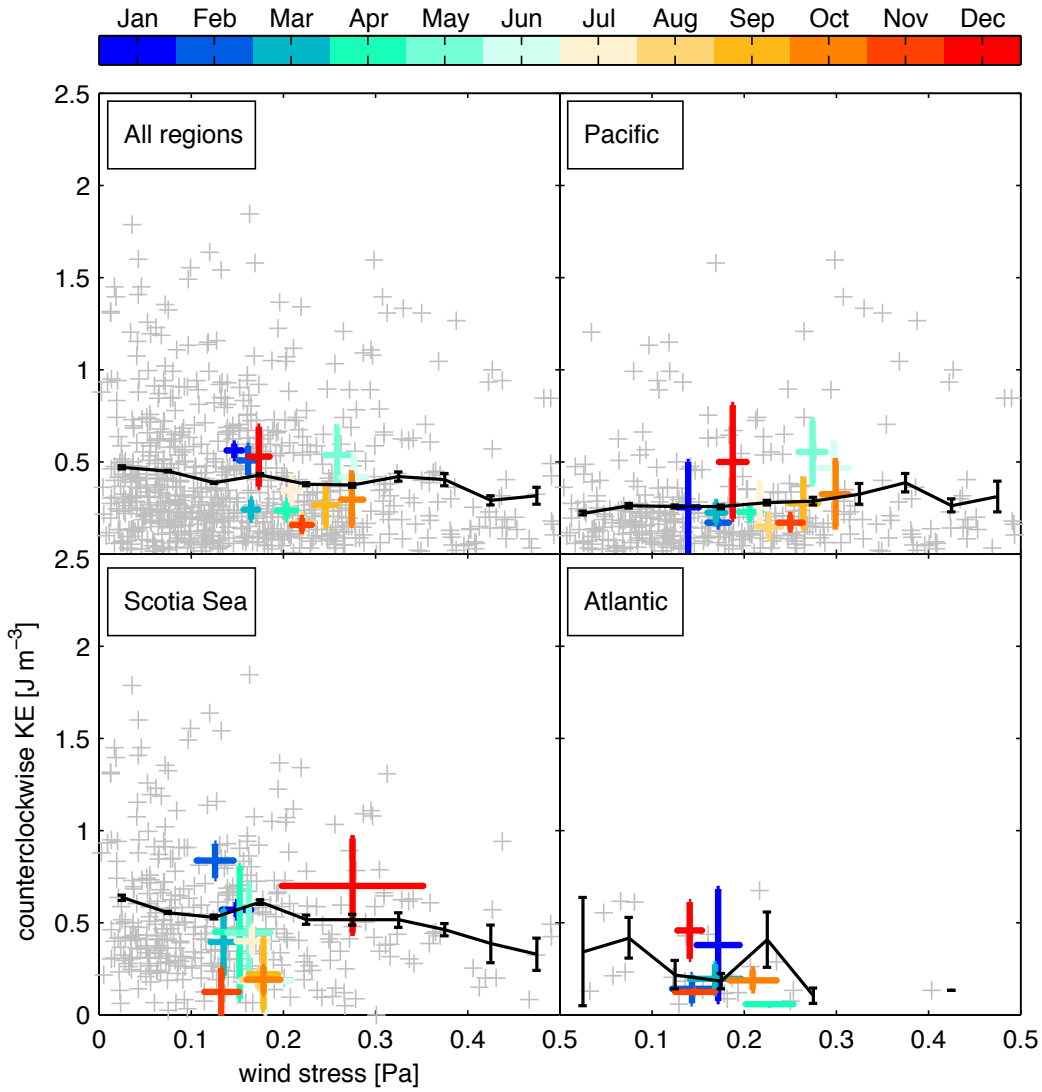

Figure 4.8: Comparison of wind-stress to the depth-averaged counterclockwise near-inertial kinetic energy across all regions (upper left) and in the Pacific, Scotia Sea, and Atlantic sectors of the Southern Ocean. Wind-stress was determined using a float-following CCMP wind time series. Each gray cross shows the wind and kinetic energy at one observation, the colored lines show the 95% confidence limits (along both axes) of the monthly averages.

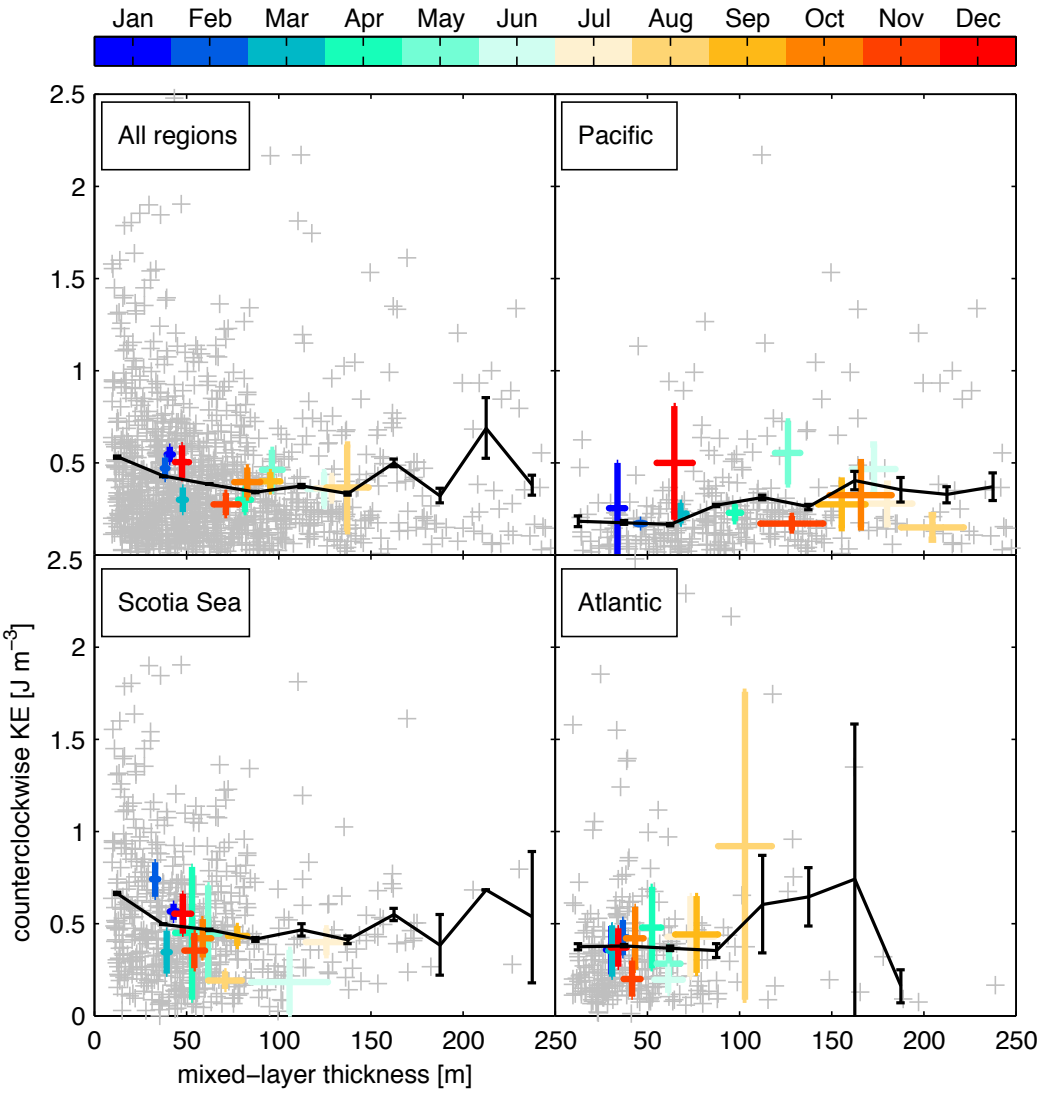

Figure 4.9: Comparison of observed mixed-layer thickness to the depth-averaged counterclockwise near-inertial kinetic energy across all regions (upper left) and in the Pacific, Scotia Sea, and Atlantic sectors of the Southern Ocean. Mixed-layer thickness was determined using a 0.005 kg m^{-3} density difference criterion. Each gray cross shows the mixed-layer thickness and kinetic energy at one observation, the colored lines show the 95% confidence limits (along both axes) of the monthly averages.

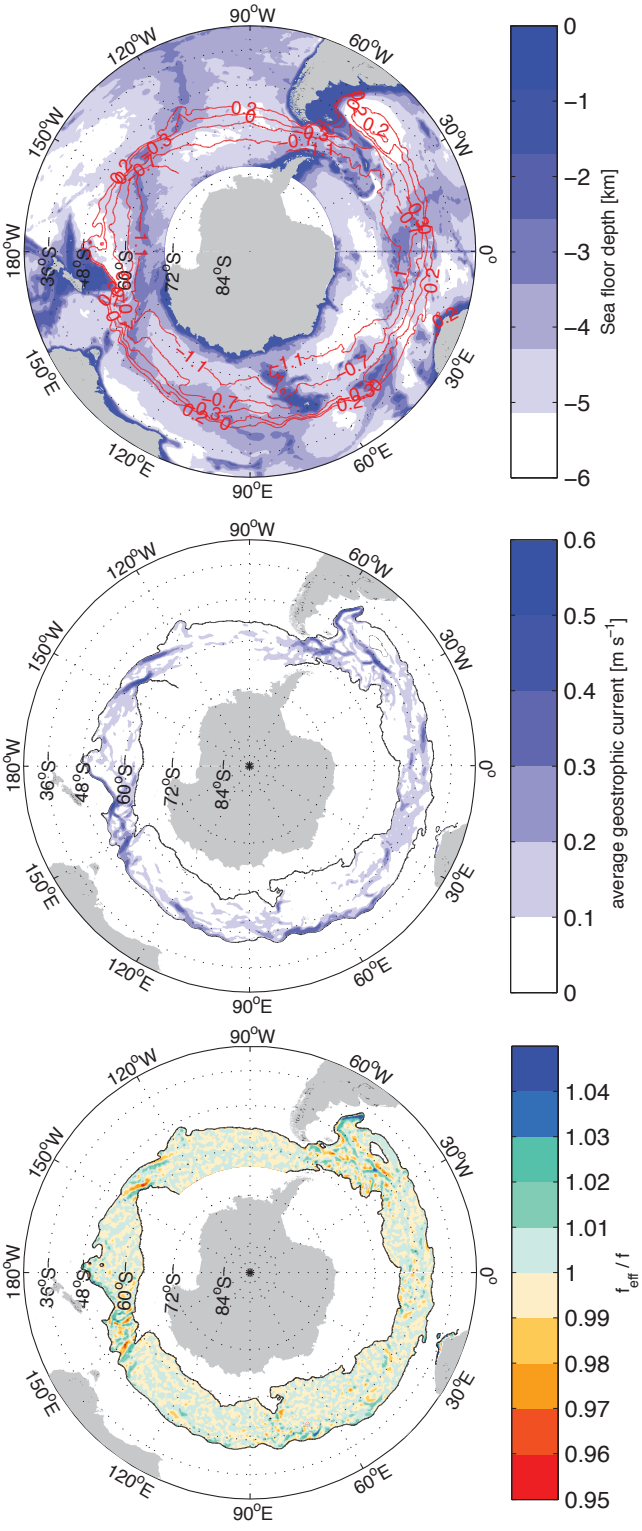
90°W
120°W
60°W
150°W
30°W
180°W
0°
150°E
30°E
120°E
60°E
90°E
36°S
48°S
60°S
72°S
84°S
Sea floor depth [km]
0
−1
−2
−3
−4
−5
−6
average geostrophic current [m s−1]
0.6
0.5
0.4
0.3
0.2
0.1
0
f_eff / f
1.04
1.03
1.02
1.01
1
0.99
0.98
0.97
0.96
0.95

Figure 4.10: Long-term average satellite (from AVISO weekly gridded absolute dynamic topography from 1993 through 2014). Top panel: The filled colored show 1° smoothed bathymetry (Smith and Sandwell one-minute version 18.1) overlaid with long-term average sea surface height contours. The selected contours show the breadth of the space which exists within closed sea surface height contours around Antarctica. Center panel: The colored contours show the magnitude of the geostrophic velocity determined from the long-term averaged sea surface height field. Regions with large amplitude mean speed show areas where the Antarctic Circumpolar Current is both strong and stationary with respect to time. These stationary features create standing vorticity features which are shown in the bottom panel. Bottom panel: The colored contours show the ratio of effective vorticity $(f + \zeta/2)$ to planetary vorticity f. Regions where this ratio is less than one tend to bend inertial-internal wave ray paths towards their centers.

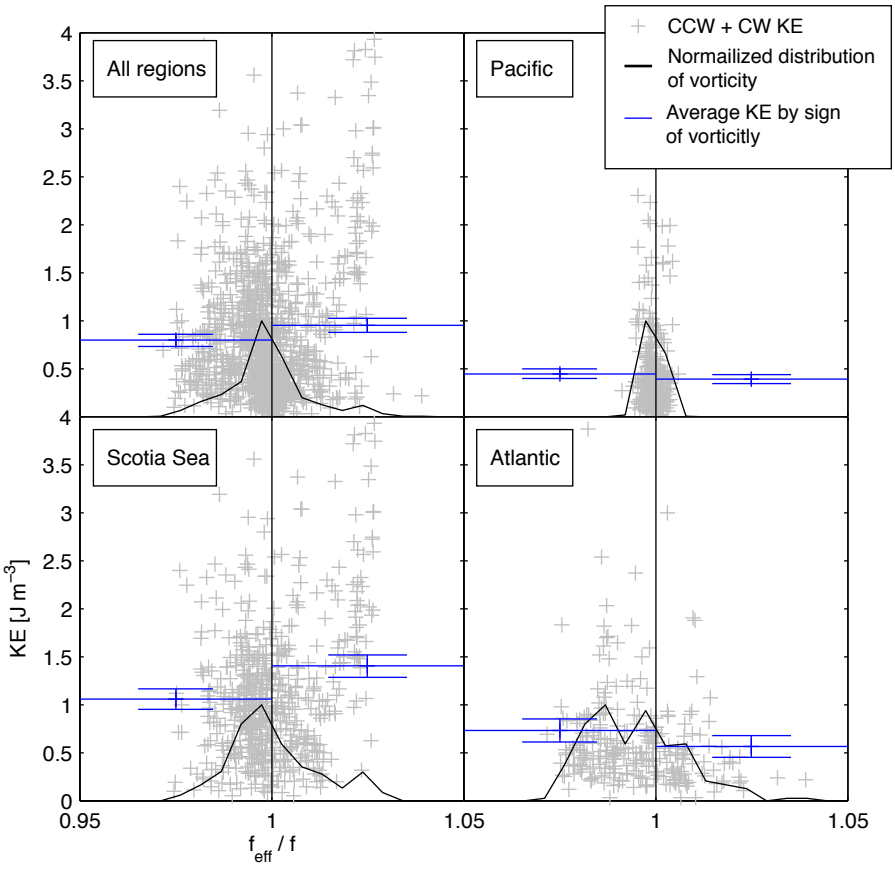

Figure 4.11: Comparison of the depth-averaged inertial-band kinetic energy with long-term average geostrophic vorticity across all regions and in the Pacific, Scotia Sea, and Atlantic sectors of the Southern Ocean. Each gray cross shows the effective vorticity and kinetic energy at one observation. The solid black line shows the normalized probability distribution of the effective vorticity ratio. Average inertial-band kinetic energy binned by sign of vorticity are shown by blue lines with 95% confidence limits.

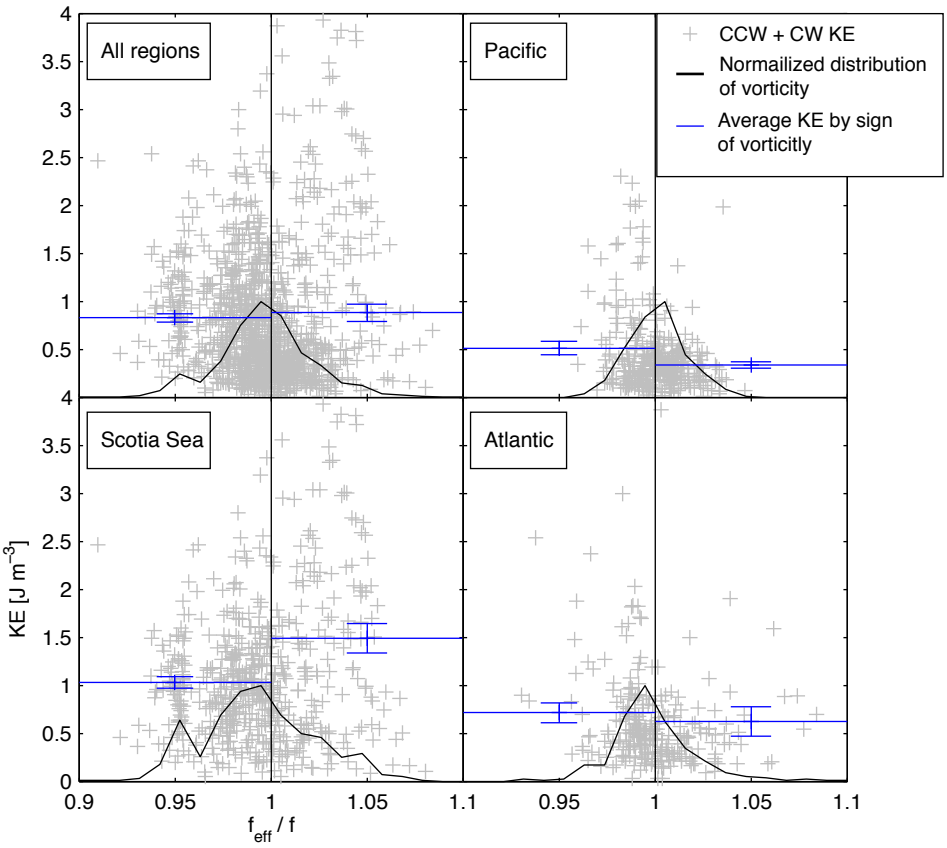

Figure 4.12: Comparison of the depth-averaged inertial-band kinetic energy with geostrophic vorticity, determined from weekly 0.33° gridded satellite altimetry, across all regions and in the Pacific, Scotia Sea, and Atlantic sectors of the Southern Ocean. Each gray cross shows a point comparison of effective vorticity to kinetic energy. The solid black line shows the normalized probability distribution of the effective vorticity ratio. Average inertial-band kinetic energy binned by sign of vorticity are shown by blue lines with 95% confidence limits.

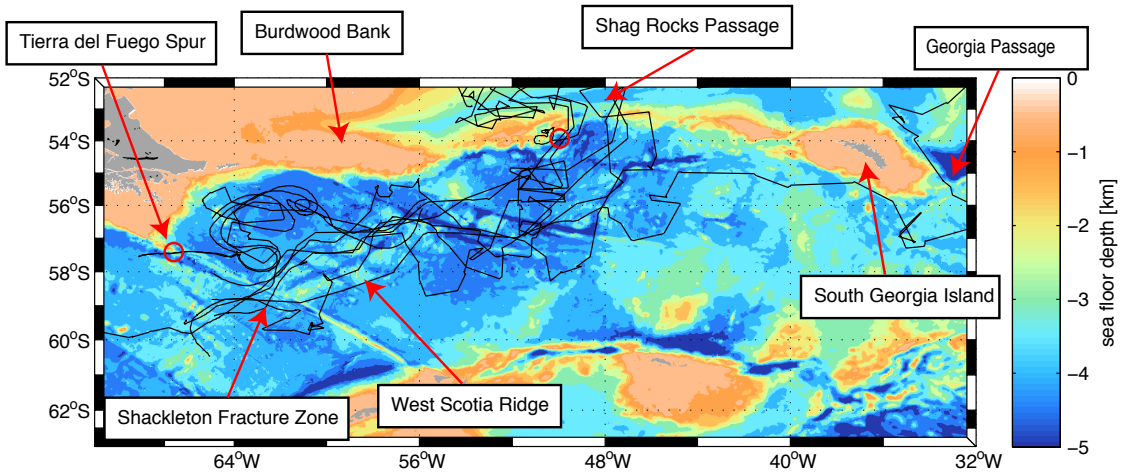

Figure 4.13: The complex bottom topography of the Scotia Sea region overlaid with EM-APEX float trajectories (shown in black). Two bathymetric features of interest are the Tierra del Fuego Spur and the Shag Rocks Passage. Large vertical velocities (in excess of 12 cm s^{-1}) were observed near each of these features. Despite each float's complex route through the Scotia Sea, most paths follow topographic features and exit the Scotia Sea through the Shag Rocks Passage.

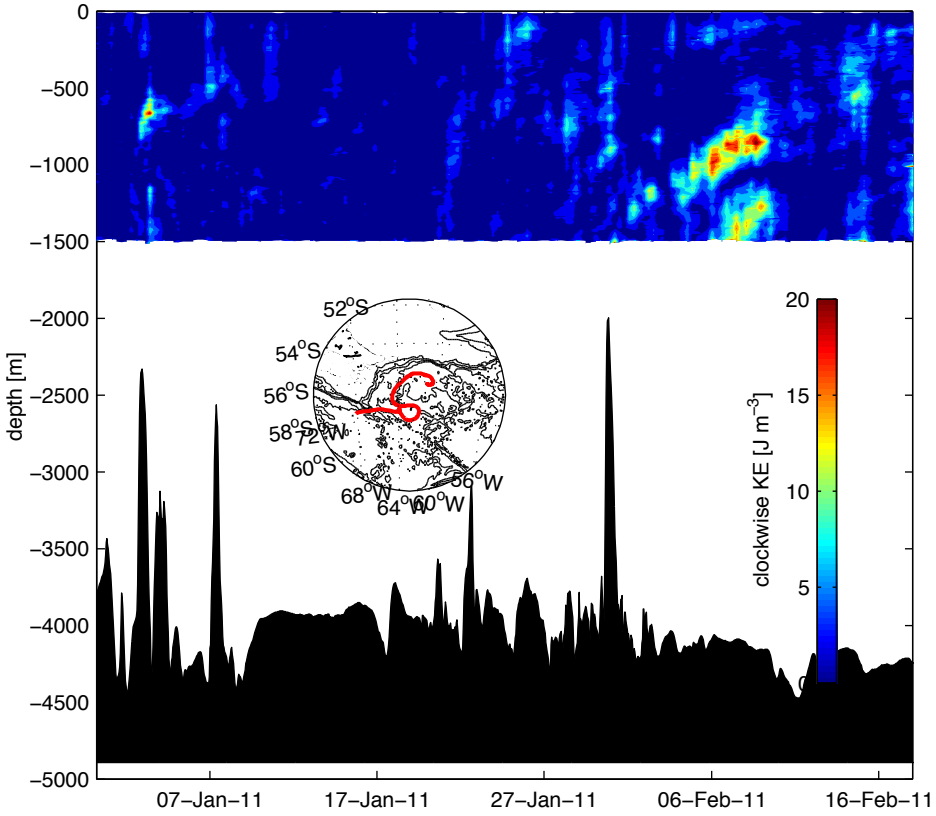

Figure 4.14: The clockwise component of inertial-band kinetic energy from float 4976 along with the along-track bottom depth. The large topographic features are the Tierra del Fuego Spur (January 5th) and an unnamed seamount (January 31st). The center panel shows the float trajectory (red) over 1000 m topographic contours (black).

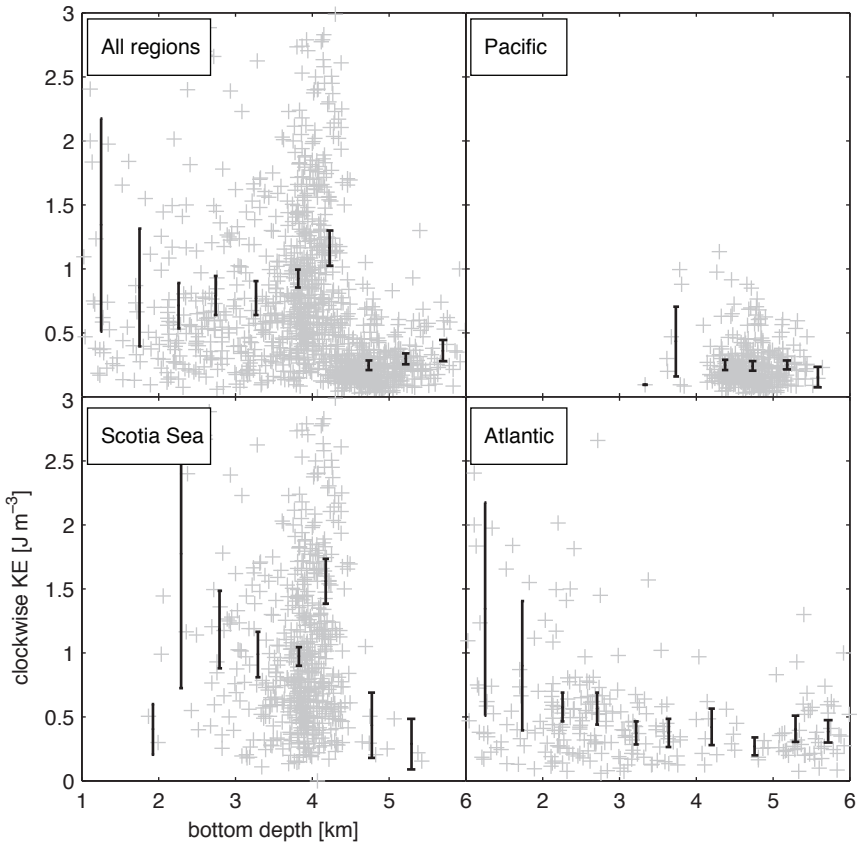

Figure 4.15: Comparison of bottom depth with the depth-averaged clockwise component of inertial-band kinetic energy, across all regions (upper left) and in the Pacific, Scotia Sea, and Atlantic sectors of the Southern Ocean. Each grey cross shows the bottom depth and inertial-band clockwise kinetic energy at each observation. The black bars show the average kinetic energy in 500 m bottom depth regions with 95% confidence limits.

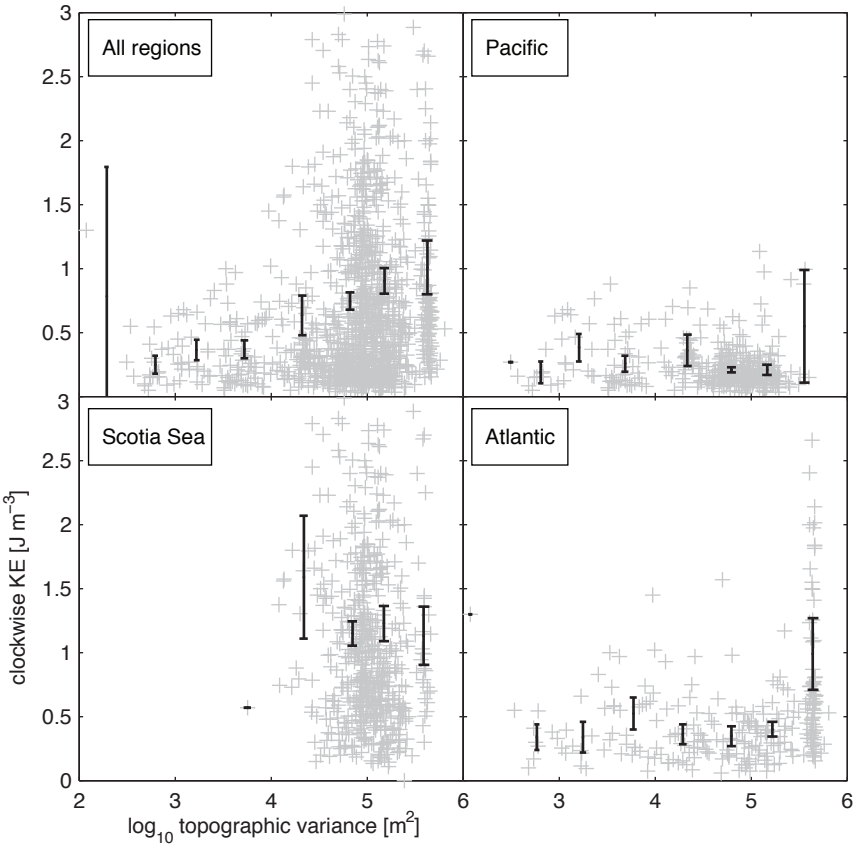

Figure 4.16: Comparison of topographic roughness (topographic variance in 1° bins) with the depth-averaged clockwise component of inertial-band kinetic energy, across all regions and in the Pacific, Scotia Sea, and Atlantic sectors of the Southern Ocean. Each grey cross shows a point comparison of topographic roughness with each observation of inertial-band clockwise kinetic energy. The black bars show bin averaged kinetic energy with 95% confidence limits.

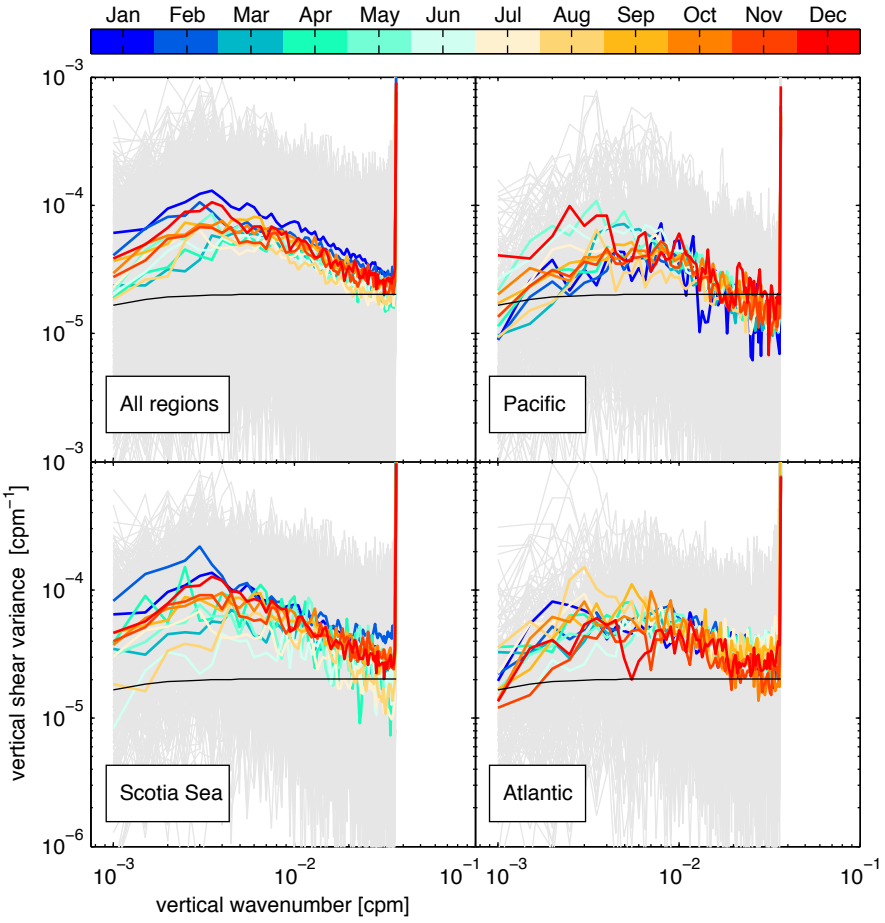

Figure 4.17: Spectra of inertial-band vertical shear, across all regions and in the Pacific, Scotia Sea, and Atlantic sectors of the Southern Ocean. Gray lines show each individual shear spectrum and colored lines show monthly averaged spectra.

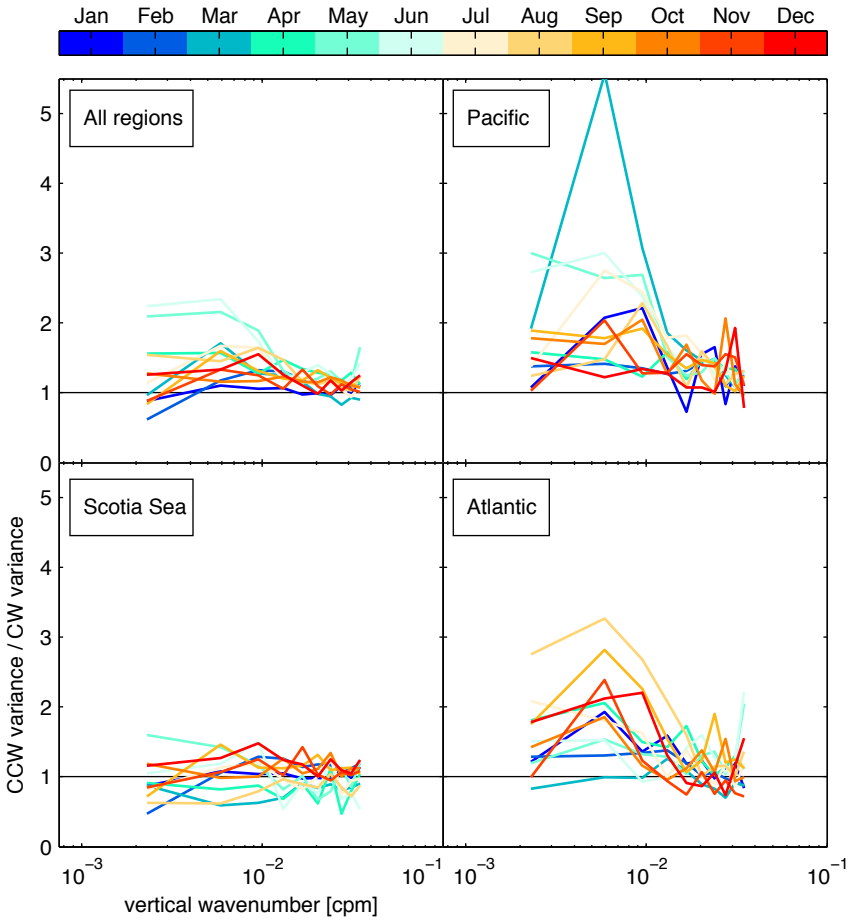

Figure 4.18: Ratio of the counterclockwise ($k_z > 0$) inertial-band vertical shear spectra to the clockwise ($k_z < 0$) inertial-band vertical shear spectra, across all regions and in the Pacific, Scotia Sea, and Atlantic sectors of the Southern Ocean. Colors indicate the ratio of monthly averaged spectra.

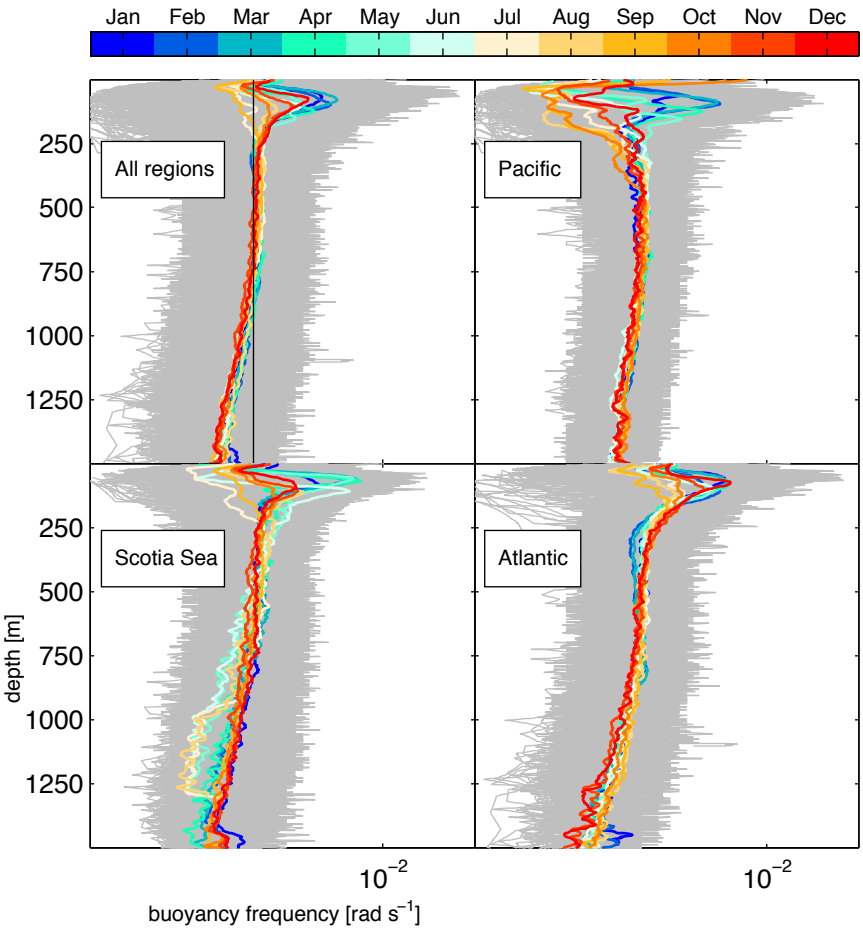

Figure 4.19: Vertical profiles of buoyancy frequency for each half-inertial difference (shown in gray), and monthly averages, shown by colored lines, for the full area and Pacific, Atlantic, and Scotia Sea sectors. The solid black line in the upper left panel shows the mean of all observations.

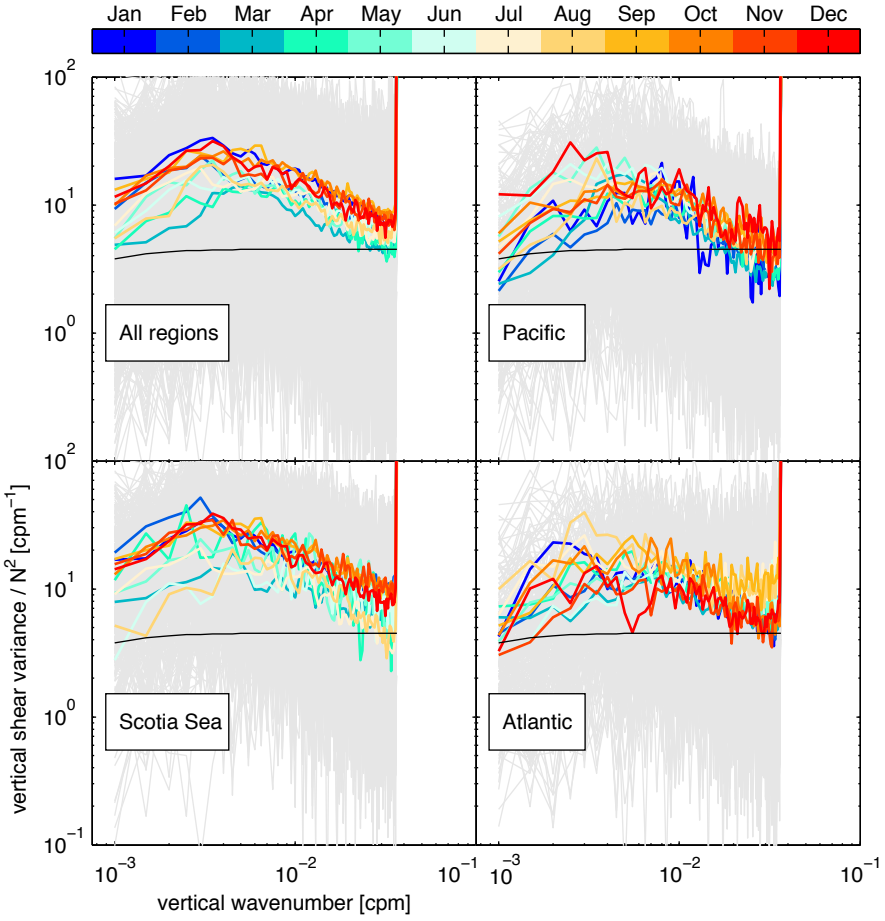

Figure 4.20: Near-inertial vertical shear spectra as in figure 4.17 normalized by N^2 to aid comparison to strain spectra.

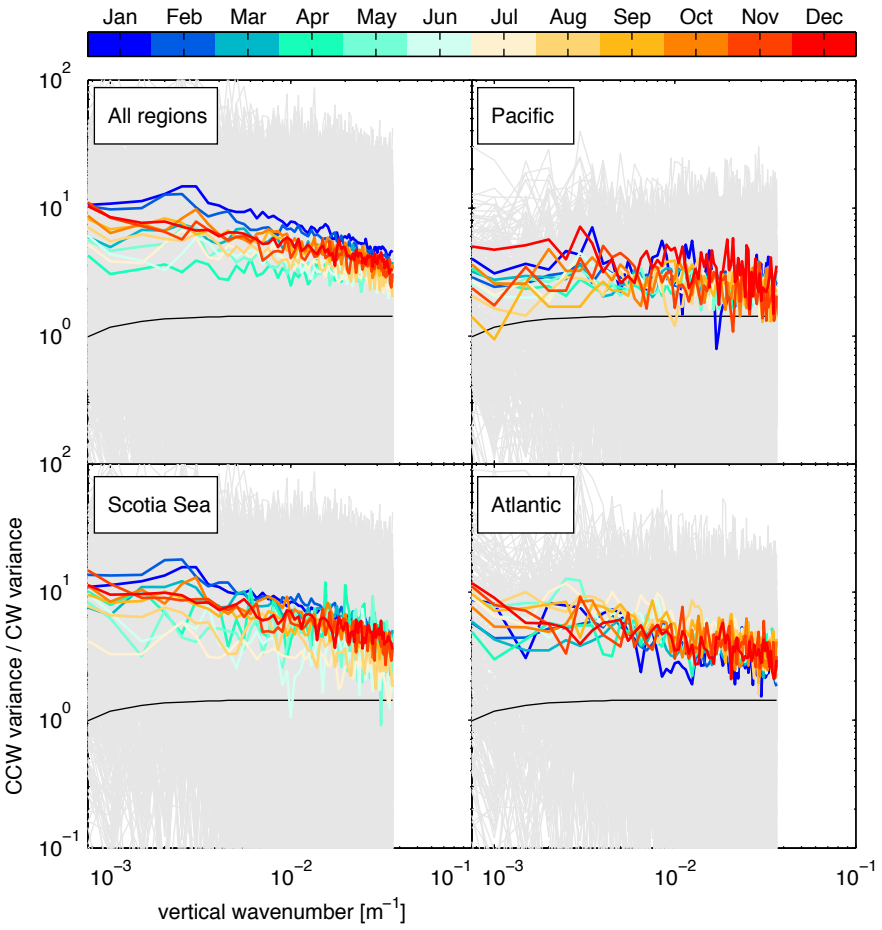

Figure 4.21: Spectra of inertial-band vertical strain, across all regions and in the Pacific, Scotia Sea, and Atlantic sectors of the Southern Ocean. The gray lines show each individual strain spectrum and the colored lines show the monthly averaged spectra. Monthly averaged spectra have been both block averaged (across individual spectra) and band averaged (by wavenumber bins).

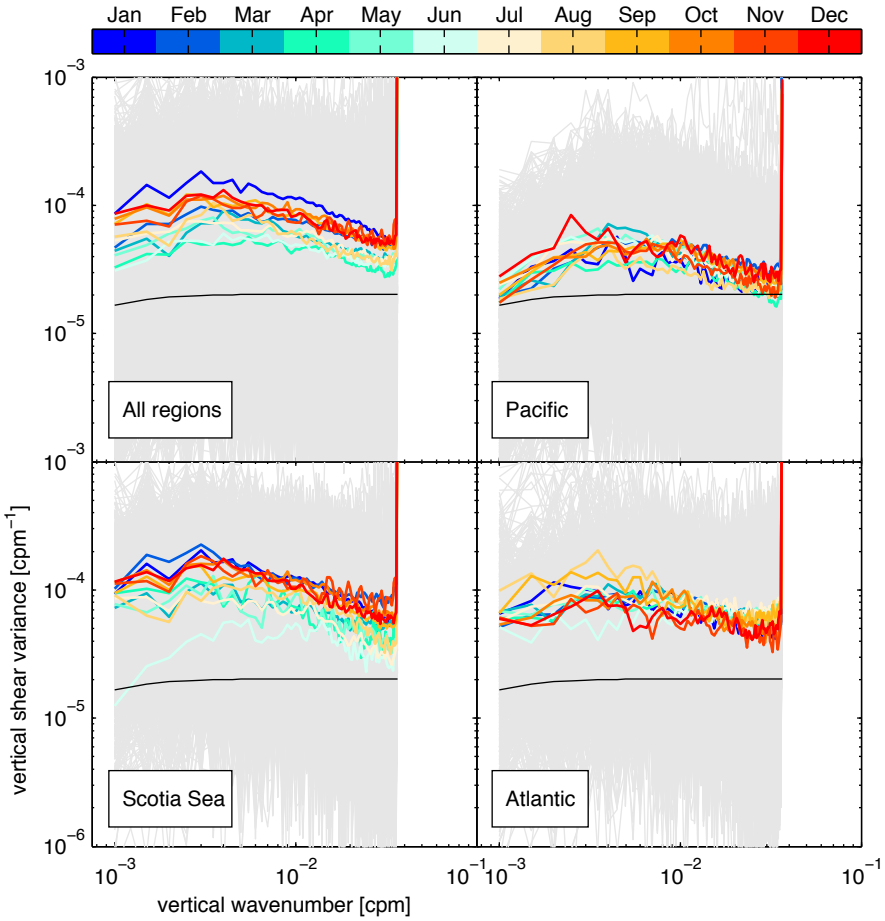

Figure 4.22: Vertical wavenumber spectra of vertical shear, displayed for all regions and in the Pacific, Scotia Sea, and Atlantic sectors of the Southern Ocean. The gray lines show each individual shear spectrum and the colored lines show the monthly averaged spectra.

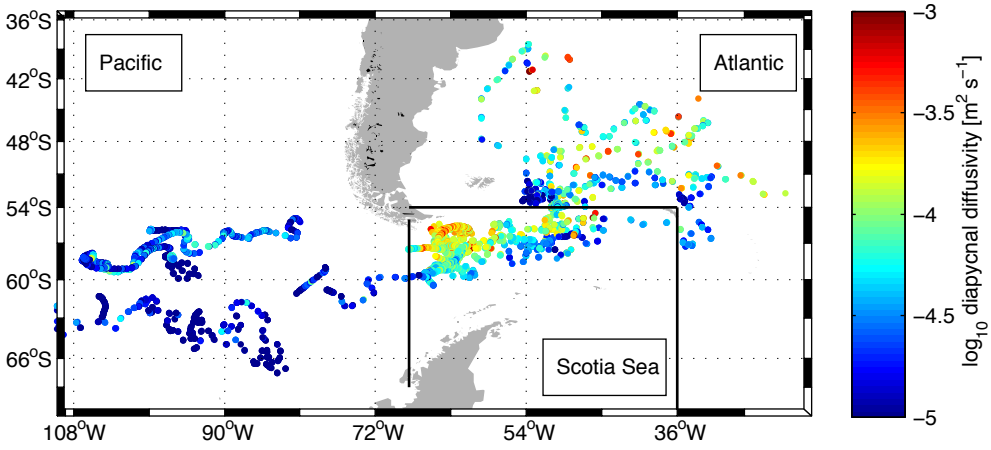

Figure 4.23: Spatial distribution of the parameterized diapycnal diffusivity. Color corresponds to the log_{10} of each estimate. The solid black lines show how the data was divided between the Pacific, Scotia Sea, and Atlantic sectors.

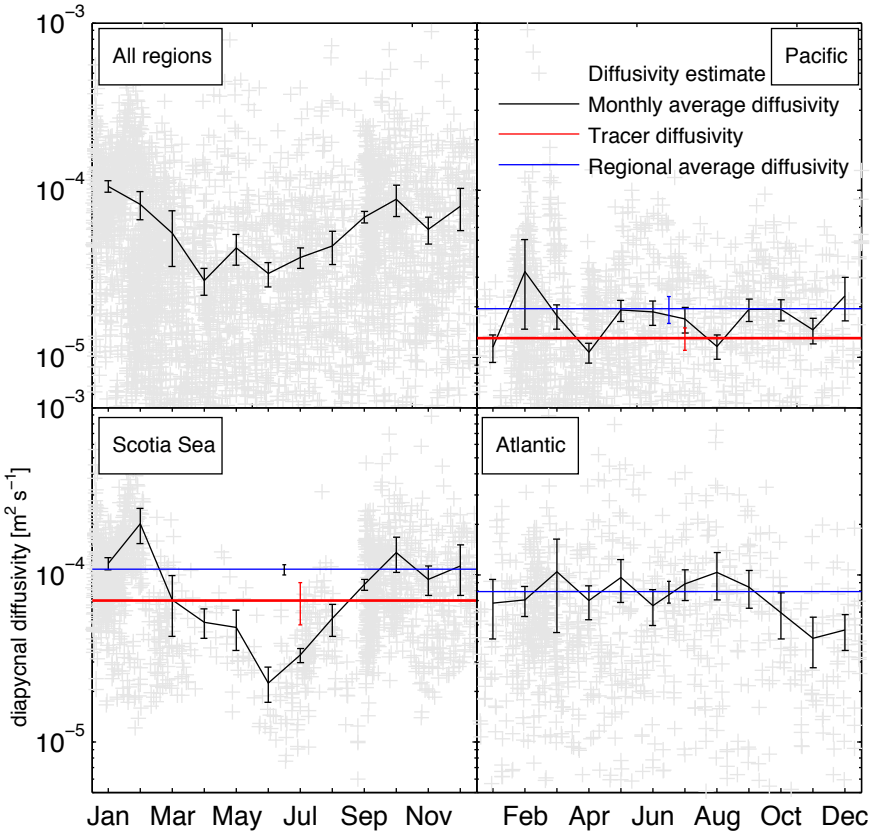

Figure 4.24: The above panels show the parameterized diapycnal diffusivity, determined from shear spectra (shown in 4.22), across all regions and in the Pacific, Scotia Sea, and Atlantic sectors of the Southern Ocean. The solid black lines show monthly average diffusivity with 95% confidence limits; the solid red line shows the dissipation rate observed from the DIMES tracer patch in the Pacific and Scotia Sea regions.

Chapter 5

CONTRIBUTIONS OF THIS RESEARCH AND SUGGESTED FUTURE WORK

5.1 Overview of research topics

The key contribution of this research is the diagnosis of both the rate of, and physical processes driving, diapycnal diffusivity in the eastern Pacific, Scotia Sea, and western Atlantic sectors of the Antarctic Circumpolar Current. These estimates address the goals of DIMES by highlighting the importance of wind driven and topographically generated internal-wave energy to interior mixing pathways. Along the path to these results this research addressed several ancillary science questions including:

- Impact of gridded wind resolution on the estimation of inertial-band wind power input
- Importance of accurately estimating the mixing-layer thickness H to wind power input
- Basin-scale spatial variability of inertial-band kinetic energy in the Southern Ocean
- Spectral shape and seasonal cycle of internal-wave vertical shear in the Antarctic Circumpolar Current

The significance of these results and ideas for future improvements are briefly described in the following sections.

5.2 Impact of gridded wind resolution

Observations of near-inertial wind forcing and downward energy propagation in the Southern Ocean illustrate several features of the upper-ocean forcing of internal waves that have long been suspected but have been difficult to observe. These include the quantitative connection between episodic near-inertial wind work and the increase of kinetic energy in the mixed

layer, (as reported in D'Asaro et al. (1995); Plueddemann and Farrar (2006); Alford et al. (2012)). These results highlight the sensitivity of wind work calculations to the details of the wind time series, particularly the spectral level at the inertial frequency, to the maximum wind stress in an event. EM-APEX velocity observations also show the radiation of the bulk of mixed-layer inertial energy in the form of downward-propagating near-inertial internal waves (Gill, 1984; D'Asaro, 1985; D'Asaro et al., 1995; Plueddemann and Farrar, 2006), and the decay of the downward propagating energy well above the sea-floor. Over a nine month EM-APEX observation period, long term average wind power input, simulated using the damped-slab model, is approximately 3 mW m^{-2}; similar to the observed downward energy flux at the base of the mixed-layer. This flux estimate relies on the assumption of a constant vertical group velocity (determined by fitting lines to apparent energy propagation in a time-depth sense) and can only be regarded as a ballpark figure. Nevertheless, the agreement suggests that most of the near-inertial wind power input radiates from the mixed-layer as propagating near-inertial internal waves.

The total range of wind work inferred from simulations forced by different wind products highlights the sensitivity of these models to both wind-stress peaks and temporal resolution. The damped-slab model forced with smoothed winds produced just 21% of the wind-work found by the same model forced with fully resolved winds. Gridded wind products may not accurately reproduce the shape, location, and speed for any given storm, particularly in regions with little *in-situ* data such as the Southern Ocean. Even when gridded winds are accurate, the lack of high-frequency variance generally diminishes the wind power input (Kilbourne and Girton, 2015a).

5.2.1 Future improvements of wind data

This research shows that highly-resolved winds dramatically alter estimates of wind power input, a conclusion which is shared by Rimac et al. (2013). New wind products with better temporal resolution have recently become available. However, this does not address the large spatial gaps in wind observations, which complicate the calibration of reanalysis products. Long-term high-resolution *in-situ* wind observations are needed, particularly in

the Southern Ocean. These data would allow a better understanding of the distribution and intermittence of high-frequency winds and their impact on ocean surface currents.

5.3 Importance and estimation of H

Estimates of near-inertial energy flux using the damped-slab near-inertial current model (Pollard and Millard, 1970) require parameterization of the thickness of the mixing-layer, defined here as the layer in direct contact with the wind-stress. This is a fundamentally different quantity from the mixed-layer, which is the weakly-stratified remnant of a past mixing event (Brainerd and Gregg, 1995). By studying the detailed vertical structure of Southern Ocean near-surface stratification we have been able to justify the use of a new fine-density criterion for determining the thickness of the actively-mixing surface boundary layer. Two independent methods of determining the wind driven mixing-layer thickness suggest that this is better-defined by depth of the $\Delta\rho = 0.005$ kg m^{-3} surface referenced density-difference. Simulations of buoyant convection indicate that buoyancy forcing alone is insufficient to drive the turbulence inferred from these observations.

Several previous studies have attempted better identification of the mixed-layer base in the ACC (Dong et al., 2008; Holte and Talley, 2009). These previous efforts identified many of the issues with existing criteria that are discussed here. However, the methods these studies recommend proved insufficient in determining the actively mixing-layer thickness. From the seasonal and spatial distribution of mixing-layer thickness, it is apparent that previous estimates of near-inertial wind power estimates (Alford, 2003) underestimate the power by a factor of 1.5 to 3.5 in the Southern Ocean and should be corrected to account for overestimated mixed-layer depths used in these calculations. This research indicates that, while the distributions of H are quite different between the three regions, a similar correction factor is appropriate for each sector. This implies that these corrections are appropriate throughout the ACC. These results emphasize the importance of quantifying the actively-mixing layer in any region where climatology indicates deep mixed-layers, not just the Southern Ocean.

5.3.1 Future improvements to mixing-layer identification

While the conclusions presented here are supported by previous microstructure observations, there is an immediate need for additional microstructure sampling in the weakly stratified surface layers considered here. Microstructure surveys from research vessels are both difficult and expensive due to distance and typical sea-state in the Southern Ocean. This presents a need for new microstructure observation platforms which are both less delicate and less expensive than those currently in use. In particular, observations of upper-ocean microstructure during the onset of a storm, while the turbulent mixing-layer is expanding, would be incredibly useful in determining the fraction of wind power input which is ultimately available for near-inertial wave radiation.

5.4 Contribution of inertial-internal waves to diapycnal diffusion in the Southern Ocean

The results presented here show weak correlation between contemporary values and monthly averages of wind-stress and downward propagating inertial-band kinetic energy. In the Pacific, depth-averaged inertial-band kinetic energy is lowest during the austral winter when the wind forcing is greatest but mixing-layers are deepest. Seasonal erosion of the pycnocline allows the formation of very deep mixing-layers, inhibiting wind power input (which is scales as H^{-1}). In the Atlantic a permanent pycnocline persists through the winter and inertial-band energy levels appear to covary with the annual cycle of wind-stress, although point comparisons were not available. Comparison of near-inertial kinetic energy in the Pacific to weekly estimates of mesoscale vorticity indicates higher energy levels are found in positive vorticity anomalies. A similar trend appears in data from the western Atlantic, but is not statistically significant. These results suggests that *in-situ* near-inertial energy is a function of local vorticity, mixed-layer thickness, and wind stress and as result accurate prediction of near-inertial energy is difficult using wind stress alone.

Diapycnal diffusivity estimated from observed vertical finestructure agrees well with direct observations of the vertical diffusion of tracer. This implies internal waves contribute sufficient energy to drive upper-ocean interior mixing in the eastern Pacific and Scotia Sea. Due to decreasing concentrations of the DIMES tracer and to the complex flow out of the

Scotia Sea, there are no direct observations of diapycnal diffusivity in the Atlantic. These diapycnal diffusivity estimates from EM-APEX in the Atlantic contribute significantly to goals of the experiment and to our understanding of the vertical structure of this region.

Inertial-band kinetic energy in the Scotia Sea appears to be generated by interactions between the strong currents and rough sea-floor topography characteristic of the region. Analysis of inertial-band energy shows that upward propagating waves dominate the energy balance in the region, an unusual result in the upper ocean. Topographic lee waves appear to drive diapycnal diffusivity in the Scotia Sea, which is approximately twenty times greater (Watson et al., 2013) than diapycnal diffusivity in the eastern Pacific.

5.4.1 Improvements to these analyses

This work highlights some of the revolutionary observations which were made possible by profiling current meters, however they are not without limitations. Analysis of single profile velocity data shows that it is difficult to resolve signals at vertical wavenumbers near and greater than 0.1 cpm, despite the instruments nominal Nyquist (Nyquist, 1928) sampling rate of 0.2 cpm. Improved processing techniques, which are not discussed in this work but have been investigated, may improve the quality of velocity spectra near the Nyquist frequency. Better resolution of the high-wavenumber end of the spectra would allow a more useful separation of the diapycnal diffusivity estimate into depth bins, potentially illuminating important details about where interior dissipation is greatest. In addition, better estimates of vertical water velocities could provide a critical resource in diagnosing wave frequency and vertical amplitude, which was generally not possible in the preceding work.

BIBLIOGRAPHY

Alford, M. H., 2001: Internal swell generation: The spatial distribution of energy flux from the wind to mixed-layer near-inertial motions. *J. Phys. Oceanogr.*, **31 (8)**, 2359–2368.

Alford, M. H., 2003: Improved global maps and 54-year history of wind-work on ocean inertial motions. *Geophys. Res. Lett.*, **30 (8)**, 1424–1427.

Alford, M. H., M. F. Cronin, and J. M. Klymak, 2012: Annual Cycle and Depth Penetration of Wind-Generated Near-Inertial Internal Waves at Ocean Station Papa in the Northeast Pacific. *J. Phys. Oceanogr.*, **42 (6)**, 889–909.

Atlas, R., R. N. Hoffman, J. Ardizzone, S. M. Leidner, J. C. Jusem, D. K. Smith, and D. Gombos, 2011: A cross-calibrated, multiplatform ocean surface wind velocity product for meteorological and oceanographic applications. *Bulletin of the American Meteorological Society*, **92 (2)**, 157–174.

Bell, T. H., Jr., 1975: Topographically generated internal waves in the open ocean. *J. Geophys. Res.*, **80**, 320–327.

Bender, C. M. and S. A. Orszag, 1978: *Asymptotic Methods and Perturbation Theory*, Advanced Mathmatical Methods for Scientists and Engineers, Vol. I. Springer Science+Business Media LLC.

Brainerd, K. E. and M. C. Gregg, 1995: Surface mixed and mixing layer depths. *Deep-Sea Res I*, **42**, 1521–1543.

Brearley, J. A., K. L. Sheen, A. C. Naveira Garabato, D. A. Smeed, and S. Waterman, 2013: Eddy-induced modulation of turbulent dissipation over rough topography in the southern ocean. *Journal of Physical Oceanography*, **43 (11)**.

Cairns, J. L. and G. O. Williams, 1976: Internal wave observations from a midwater float, 2. *J. Geophys. Res.*, **81**, 1943–1950.

D'Asaro, E., 1985: The energy flux from the wind to near-inertial motions in the mixed layer. *J. Phys. Oceanogr.*, **15**, 943–959.

D'Asaro, E., C. Lee, L. Rainville, R. Harcourt, and L. Thomas, 2011: Enhanced turbulence and energy dissipation at ocean fronts. *Science*, **332 (6027)**, 318–322.

D'Asaro, E., J. Thomson, A. Shcherbina, R. Harcourt, M. Cronin, M. Hemer, and B. Fox-Kemper, 2014: Quantifying upper ocean turbulence driven by surface waves. *Geophysical Research Letters*, **41 (1)**, 102–107.

D'Asaro, E. A., 2001: Turbulent vertical kinetic energy in the ocean mixed layer. *J. Phys. Oceanogr.*, **31**, 3530–3537.

D'Asaro, E. A., C. E. Eriksen, M. D. Levine, P. Niiler, C. A. Paulson, and P. V. Meurs, 1995: Upper-ocean inertial currents forced by a strong storm, part I, Data and comparisons with linear theory. *J. Phys. Oceanogr.*, **25**, 2909–2936.

de Boyer Montégut, C., G. Madec, A. S. Fischer, A. Lazar, and D. Iudicone, 2004: Mixed layer depth over the global ocean: An examination of profile data and a profile-based climatology. *Journal of Geophysical Research: Oceans*, **109 (C12)**, n/a–n/a, doi: 10.1029/2004JC002378, URL `http://dx.doi.org/10.1029/2004JC002378`.

Dong, S., J. Sprintall, S. T. Gille, and L. Talley, 2008: Southern ocean mixed-layer depth from argo float profiles. *Journal of Geophysical Research: Oceans (1978–2012)*, **113 (C6)**.

Elipot, S. and R. Lumpkin, 2008a: Spectral description of oceanic near-surface variability. *Geophysical Research Letters*, **35 (L05606)**.

Elipot, S. and R. Lumpkin, 2008b: Spectral description of oceanic near-surface variability. *Geophys. Res. Lett.*, **35 (5)**, L05 606.

Fu, L.-L., 1981: Observations and models of inertial waves in the deep ocean. *Rev. Geophys. Space Phys.*, **19 (1)**, 141–170.

Garrett, C., 1999: What is the "near-inertial" band and why is it different? *'Aha Huliko'a Proceedings.*

Garrett, C. and W. Munk, 1972: Space-time scales of internal waves. *Geophys. Fluid Dyn.*, **3**, 225–264.

Garrett, C. J. R. and W. H. Munk, 1975: Space-time scales of internal waves: A progress report. *J. Geophys. Res.*, **80 (3)**, 291–297.

Gill, A. E., 1982: *Atmosphere-Ocean Dynamics*. Academic, 662 pp.

Gill, A. E., 1984: On the behavior of internal waves in the wake of a storm. *J. Phys. Oceanogr.*, **14**, 1129–1151.

Gonella, J., 1972: A rotary-component method for analysing meteorological and oceanographic vector time series. *Deep-Sea Res.*, **19**, 833–846.

Gregg, M. C., 1976: Finestructure and microstructure observations during the passage of a mild storm. *J. Phys. Oceanogr.*, **6**, 528–555.

Gregg, M. C., T. B. Sanford, and D. P. Winkel, 2003: Reduced mixing from the breaking of internal waves in equatorial waters. *Nature*, **422**, 513–515.

Harris, F. J., 1978: On the use of windows for harmonic analysis with the discrete fourier transform. *Proceedings of the IEEE*, **66 (1)**, 51–83.

Holte, J. and L. Talley, 2009: A new algorithm for finding mixed layer depths with applications to argo data and subantarctic mode water formation. *Journal of Atmospheric & Oceanic Technology*, **26 (9)**.

Hosegood, P. J., M. C. Gregg, and M. H. Alford, 2008: Restratification of the surface mixed layer with submesoscale lateral density gradients: Diagnosing the importance of the horizontal dimension. *J. Phys. Oceanogr.*, **38**, 2438–2460.

Jiang, J., Y. Lu, and W. Perrie, 2005: Estimating the energy flux from the wind to ocean inertial motions: The sensitivity to surface wind fields. *Geophys. Res. Lett.*, **32 (L15610)**, doi:10.1029/2005GL023 289.

Kalnay, E. M., et al., 1996: The NCEP/NCAR 40-year reanalysis project. *Bulletin of the American Meteorological Society*, **77**, 437–471.

Kilbourne, B. F. and J. B. Girton, 2015a: Quantifying high-frequency wind energy flux into near-inertial motions in the southeast pacific. *Journal of Physical Oceanography*, **45 (2)**, 369–386.

Kilbourne, B. F. and J. B. Girton, 2015b: Surface boundary layer evolution and near-inertial wind power input, submitted to the Journal of Geophysical Research - Oceans on 9 August 2015.

Klein, P., G. Lapeyre, and W. G. Large, 2004: Wind ringing of the ocean in presence of mesoscale eddies. *Geophys. Res. Lett.*, **31 (L15306)**, doi:10.1029/2004GL020 274.

Kundu, P. K., 1990: *Fluid Mechanics*. Academic Press.

Kunze, E., 1985: Near-inertial wave propagation in geostrophic shear. *J. Phys. Oceanogr.*, **15**, 544–565.

Kunze, E., E. Firing, J. Hummon, T. K. Chereskin, and A. Thurnherr, 2006: Global abyssal mixing inferred from lowered ADCP shear and CTD strain profiles. *J. Phys. Oceanogr.*, **36**, 1553–1576.

Kunze, E., R. W. Schmitt, and J. M. Toole, 1995: The energy balance in a warm-core ring's near-inertial critical layer. *J. Phys. Oceanogr.*, **25 (5)**, 942–957.

Langmuir, I. et al., 1938: Surface motion of water induced by wind. *Science*, **87 (2250)**, 119–123.

Large, W. G. and S. Pond, 1981: Open ocean momentum flux measurements in moderate to strong winds. *J. Phys. Oceanogr.*, **11**, 324–336.

Leaman, K. D. and T. B. Sanford, 1975: Vertical energy propagation of inertial waves: A vector spectral analysis of velocity profiles. *J. Geophys. Res.*, **80 (15)**, 1975–1978.

Ledwell, J. R., L. C. St. Laurent, J. B. Girton, and J. M. Toole, 2011: Diapycnal Mixing in the Antarctic Circumpolar Current. *J. Phys. Oceanogr.*, **41 (1)**, 241–246, doi:10.1175/2010JPO4557.1, URL `http://journals.ametsoc.org/doi/abs/10.1175/2010JPO4557.1`.

Lee, D. and P. Niiler, 1998: The inertial chimney: The near-inertial energy drainage from the ocean surface to the deep layer. *Journal of Geophysical Research*, **103**, 7579–7591.

Li, M. and C. Garrett, 1993: Cell merging and the jet/downwelling ratio in langmuir circulation. *Journal of marine research*, **51 (4)**, 737–769.

Li, M. and C. Garrett, 1997: Mixed layer deepening due to langmuir circulation. *Journal of physical oceanography*, **27 (1)**, 121–132.

Lorbacher, K., D. Dommenget, P. Niiler, and A. Köhl, 2006: Ocean mixed layer depth: A subsurface proxy of ocean-atmosphere variability. *Journal of Geophysical Research: Oceans (1978–2012)*, **111 (C7)**.

Marshall, J. and F. Schott, 1999: Open-ocean convection: Observations, theory, and models. *Reviews of Geophysics*, **37 (1)**, 1–64.

McComas, C. H. and P. Müller, 1981: The dynamic balance of internal waves. *J. Phys. Oceanogr.*, **11**, 970–986.

Mied, R. P., G. J. Lindemann, and C. L. Trump, 1987: Inertial Wave Dynamics in the North Atlantic Subtropical Zone. *Journal of Geophysical Research*, **92 (C12)**, 13 063–13 074, doi:10.1029/JC092iC12p13063, URL `http://www.agu.org/pubs/crossref/1987/JC092iC12p13063.shtml`.

Monterey, G. I. and S. Levitus, 1997: *Seasonal variability of mixed layer depth for the world ocean.*

Munk, W. and C. Wunsch, 1998: Abyssal recipes II: energetics of tidal and wind mixing. *Deep-Sea Res. Part I*, **45**, 1977–2010.

Nyquist, H., 1928: Certain topics in telegraph transmission theory. *American Institute of Electrical Engineers, Transactions of the*, **47 (2)**, 617–644.

Plueddemann, A. J. and J. T. Farrar, 2006: Observations and models of the energy flux from the wind to mixed layer inertial currents. *Deep-Sea Research*, **53**, 5–30.

Pollard, R. T. and R. C. Millard, 1970: Comparison between observed and simulated wind-generated inertial oscillations. *Deep-Sea Res.*, **17**, 153–175.

Polzin, K. L., J. M. Toole, and R. W. Schmitt, 1995: Finescale parameterizations of turbulent dissipation. *J. Phys. Oceanogr.*, **25**, 306–328.

Powell, M. D., P. J. Vickery, and T. A. Reinhold, 2003: Reduced drag coefficient for high wind speeds in tropical cyclones. *Nature*, **422 (6929)**, 279–283.

Price, J. F., R. A. Weller, and R. Pinkel, 1986: Diurnal cycling: Observations and models of the upper ocean response to diurnal heating, cooling, and wind mixing. *J. Geophys. Res.*, **91**, 8411–8427.

Rimac, A., J.-S. von Storch, C. Eden, and H. Haak, 2013: The influence of high-resolution wind stress field on the power input to near-inertial motions in the ocean. *Geophysical Research Letters*, **40 (18)**, 4882–4886, doi:10.1002/grl.50929, URL `http://dx.doi.org/10.1002/grl.50929`.

Rossby, H. T. and T. B. Sanford, 1976: A study of velocity profiles through the main thermocline. *J. Phys. Oceanogr.*, **6 (5)**, 766–774.

Sanford, T., J. Dunlap, J. Carlson, D. Webb, and J. Girton, 2005: Autonomous velocity and density profiler: EM-APEX. *Proceedings of the IEEE/OES Eighth Working Conference on Current Measurement Technology, 2005.*, IEEE, 152–156, doi:10.1109/CCM.2005.1506361, URL `http://ieeexplore.ieee.org/lpdocs/epic03/wrapper.htm?arnumber=1506361`.

Sanford, T. B., 1975: Observations of the vertical structure of internal waves. *J. Geophys. Res.*, **80 (27)**, 3861–3871.

Schmidtko, S., G. C. Johnson, and J. M. Lyman, 2013: Mimoc: A global monthly isopycnal upper-ocean climatology with mixed layers. *Journal of Geophysical Research: Oceans*, **118 (4)**, 1658–1672.

Sheen, K. L., et al., 2013: Rates and mechanisms of turbulent dissipation and mixing in the Southern Ocean: Results from the Diapycnal and Isopycnal Mixing Experiment in the Southern Ocean (DIMES). *J. Geophys. Res.*, **118**, 1–19, doi:http://10.1002/jgrc.20217.

Silverthorne, K. E. and J. M. Toole, 2009: Seasonal kinetic energy variability of near-inertial motions. *J. Phys. Oceanogr.*, **39 (4)**, 1035–1049.

Smith, W. H. F. and D. T. Sandwell, 1997: Global sea floor topography from satellite altimetry and ship depth soundings. *Science*, **277**, 1957–1962.

Thomson, R. and W. Huggett, 1981: Wind-driven inertial oscillations of large spatial coherence. *Atmos.-Ocean.*, **19**, 281–306.

Thomson, R. E. and I. V. Fine, 2003: Estimating mixed layer depth from oceanic profile data. *Journal of Atmospheric and Oceanic Technology*, **20 (2)**, 319–329.

Thorpe, S. A., 2004: Langmuir circulation. *Annu. Rev. Fluid Mech.*, **36**, 55–79.

Watanabe, M. and T. Hibiya, 2002: Global estimates of the wind-induced energy flux to inertial motions in the surface mixed layer. *Geophys. Res. Lett.*, **29 (8)**, 10.1029/2001GL014 422.

Watson, A. J., J. R. Ledwell, M.-J. Messias, B. A. King, N. Mackay, M. P. Meredith, B. Mills, and A. C. N. Garabato, 2013: Rapid cross-density ocean mixing at mid-depths in the drake passage measured by tracer release. *Nature*, **501 (7467)**, 408–411.

Webster, F., 1968: Observations of Inertial-Period Motions in the Deep Sea. *Reviews of Geophysics*, **6 (4)**, 473–490, URL `http://www.agu.org/pubs/crossref/1968/RG006i004p00473.shtml`.

Welch, P. D., 1967: The use of fast fourier transform for the estimation of power spectra: A method based on time averaging over short, modified periodograms. *IEEE Trans. Audio Electroacoustics*, **AU-15**, 70–73.

Weller, R. A. and J. F. Price, 1988: Langmuir circulation within the oceanic mixed layer. *Deep Sea Research Part A. Oceanographic Research Papers*, **35 (5)**, 711–747.

Zhai, X., R. J. Greatbatch, and C. Eden, 2007: Spreading of near-inertial energy in a $1/12^o$ model of the North Atlantic Ocean. *Geophys. Res. Lett.*, **34 (L10609)**, doi:10.1029/2007GL029 895.

Zhai, X., R. J. Greatbatch, and J. Zhao, 2005: Enhanced vertical propagation of storm-induced near-inertial energy in an eddying ocean channel. *Geophys. Res. Lett.*, **32,doi:10.1029/2005GL023643**, 1–4.

Zhang, H.-M., J. J. Bates, and R. W. Reynolds, 2006: Assessment of composite global sampling: Sea surface wind speed. *Geophysical Research Letters*, **33 (17)**.